

**A STUDY OF AN ISORETICULAR METAL-ORGANIC
FRAMEWORK (IRMOF-8) FOR GAS STORAGE: SYNTHESIS,
FUNCTIONALIZATION AND NANOCONFINEMENT**

by

SAMUEL ABIDEMI OREFUWA

A DISSERTATION

Submitted in partial fulfillment for the requirements
for the degree of Doctor of Philosophy in the
Applied Chemistry Graduate Program of
Delaware State University
DOVER, DELAWARE

2013

Dedication

This doctorate research work is dedicated to God, My wife Mary and my sons (Joshua and John).

Acknowledgments

First I would like to thank my supervisor, Dr. Andrew J. Goudy for giving me the scientific freedom during the work on my thesis. Also, for his great support and constructive criticism.

I will also like to thank all the members of the hydrogen storage group for a great time with them and friendly working atmosphere: Dr. Hongwei Yang, Dr. Saidi Temitope Sabitu, Tolulope Durojaiye, Dr. Adeola Ahmed Ibikunle, Jalaal Hayes, Esosa Iriowen and Mrs. Sanchez.

I am also grateful to the entire staff and faculty of the Department of Chemistry for making the learning environment friendly. To my committee members, I say thank you.

I must say a big thank you to my parents Presiding Elder and Deaconess Amos Orefuwa and my siblings, Daniel, Esther, Dupe, Tope and Elizabeth for their prayers, and encouragement.

Special appreciation goes to the US Department of Transportation the Department of Energy and the Thurgood Marshall College Fund for Graduate Research for the funding.

To my wife, without a flinch of a doubt, you and the boys are highly appreciated. You gave me all the time, support and prayers that I needed and sacrificed a lot for me. Thank you my wife, Mary, and the boys, John and Joshua.

To Him from whom I get my knowledge, wisdom, understanding and inspiration; God Almighty, I say thank you.

ABSTRACT

The synthesis, functionalization and scaffolding potentials of MOFs for improving H₂, CH₄ and CO₂ storage are hereby reported. A rapid and inexpensive solvothermal method for producing high quality IRMOF-8 (isorecticular metal–organic framework) crystals in 2–4 hours has been developed. This is 10-12 times faster than the traditional solvothermal convective oven synthesis method. The effect of temperature on the pore volume, pore size, specific surface area(SSA) and hydrogen storage capacity of convective oven synthesized IRMOF-8 (C-IRMOF-8) and the rapid solvothermal synthesized IRMOF-8 (RS-IRMOF-8) were also investigated. The optimum synthesis temperatures were 120 °C and 155 °C for C-IRMOF-8 and RS-IRMOF-8, respectively. BET analysis showed that the SSA and pore volume of RS-IRMOF-8 (1801 m²/g, 0.693 cm³/g) were greater than that of C-IRMOF-8(1694 m²/g, 0.603 cm³/g) at the optimum temperatures.

In a further study, a novel IRMOF-8-NO₂ was synthesized. BET and gas sorption analysis showed that a large decrease in surface area and pore volume of the IRMOF-8-NO₂ did not result in a proportionate decrease in gas sorption capability. The amounts of hydrogen, methane and carbon dioxide adsorbed by the IRMOF-8-NO₂ were disproportionately high. A new concept known as sticking factor was determined for the adsorption of each gas on the two MOFs at various temperatures. In all cases, the sticking factors for gases adsorbed on the IRMOF-8-NO₂ were greater than those for gas adsorbed on the IRMOF-8. It was found that, in all cases, the enthalpies for gas adsorption on IRMOF-8-NO₂ were greater than those for IRMOF-8. Thus it appears that

nitro-functionalization strengthens the bonding of the gases to the surface thereby resulting in greater sticking efficiency and larger than expected gas adsorption.

Finally, attempts have been made to decrease the hydrogen desorption temperature of NaAlH_4 (sodium alanate) which is approximately 186 °C. Nanoconfined NaAlH_4 was prepared by the wet infiltration of bulk NaAlH_4 into IRMOF-8 and mesoporous carbon (MC). The BET pore volume of NaAlH_4 @IRMOF-8 and NaAlH_4 @MC showed a 40% and 23% infiltrated NaAlH_4 respectively. The residual gas analysis (RGA) and temperature program desorption (TPD) of the composite showed a 90-60 °C decrease in dehydrogenation temperature of NaAlH_4 by nanoconfinement.

TABLE OF CONTENTS

Title page.....	i
Dedication page.....	ii
Acknowledgment.....	iii
Abstract.....	iv
Table of contents.....	vi
Lists of tables.....	x
Lists of figures.....	xi
1 Introduction and Motivation.....	1
1.1 Properties of Hydrogen.....	3
1.2 Hydrogen Storage Methods and Goals of Department of Energy.....	3
1.2.1 Compressed Hydrogen Tanks.....	4
1.2.2 Cryogenic Hydrogen Tanks.....	5
1.2.3 Solid State Hydrogen Storage.....	6
1.2.3.1 Chemisorption of Hydrogen Atoms in Metals.....	7
1.2.3.2 Compounds with Ionic Character (Complex Hydrides)....	8
1.2.3.3 Physisorption of Hydrogen in Porous Materials.....	10
1.3 Properties of Methane and Methods of Storage.....	11
1.3.1 Compressed Natural Gas (CNG) Tanks.....	11
1.3.2 Liquefied Natural (LNG) Tanks.....	11
1.3.3 Adsorbed Natural Gas (ANG); Solid State Storage and Goal of the Department of Energy.....	12
1.4 Properties and Methods of Carbon Dioxide Capture and Sequestration...12	
1.4.1 Carbon Dioxide Capture and Sequestration.....	13

1.5	Metal-Organic Frameworks.....	15
1.5.1	IUPAC Classification of Porous Materials and Types of Adsorption Isotherms.....	22
1.5.2	Principles or Fundamentals of Physisorption.....	24
1.5.3	Why Isorecticular metal-organic framework (IRMOF-8).....	28
1.6	Goals and Objectives of this Research.....	30
2	Experimental Details.....	32
2.1	Materials and Methods.....	32
2.1.1	Convectional and Rapid Solvothermal Synthesis of Isorecticular Metal-Organic Framework-8 (C-IRMOF-8 and RS-IRMOF-8)....	33
2.1.2	Synthesis of IRMOF-8-NO ₂	34
2.1.3	Nanoconfinement of NaAlH ₄ @IRMOF-8.....	35
2.2	Sample Handling, Characterization and Measurements.....	35
2.2.1	Argon glove box.....	35
2.2.2	X-Ray Diffractometer (XRD).....	36
2.2.3	Thermogravimetric Analyzer (TGA).....	38
2.2.4	Fourier Transformed Infrared Spectroscopy (FTIR).....	39
2.2.5	Nuclear Magnetic Resonance (NMR).....	40
2.2.6	Laser Diffraction Particle Size Analyzer (LDPSA).....	41
2.2.7	Surface Area and Porosity Analyzer.....	42
2.2.8	High Pressure Volumetric Analyzer (HPVA).....	45
2.2.9	Pressure Composition Isotherm (PCI) Instrument for Temperature Program Desorption (TPD).....	47
2.2.10	Residual Gas Analyzer (RGA, a mass spectrometer).....	48

3	Rapid Solvothermal Synthesis of IRMOF-8.....	50
3.1	X-Ray Diffraction of C-IRMOF-8 and RS-IRMOF-8.....	51
3.2	Infrared Spectroscopy of C-IRMOF-8 and RS-IRMOF-8.....	54
3.3	Thermogravimetric Analysis of C-IRMOF-8 and RS-IRMOF-8.....	55
3.4	Laser Diffraction Particle Size Analysis of C-IRMOF-8 and RS-IRMOF-8	57
3.5	Specific Surface Area and Porosity Analysis of C-IRMOF-8 and RS- IRMOF-8.....	58
3.6	Hydrogen Adsorption Isotherms of C-IRMOF-8 and RS-IRMOF-8.....	63
3.7	Conclusion.....	64
4	Effects of Nitro-functionalization on the Gas Adsorption Properties of Isorecticular Metal-Organic Framework-Eight (IRMOF-8).....	66
4.1	X-Ray Diffraction Analysis of IRMOF-8 and IRMOF-8-NO ₂	66
4.2	Fourier Transformed Infrared Spectroscopy of IRMOF-8 and IRMOF-8-NO ₂	68
4.3	Proton NMR of the Ligands (2,6-Naphthalenedicarboxylic acid and 4,8-dinitro-2,6-Naphthalenedicarboxylic acid.....	69
4.4	Thermogravimetric Analysis RS-IRMOF-8 and RS-IRMOF-8-NO ₂	72
4.5	Residual Gas Analysis of IRMOF-8 and IRMOF-8-NO ₂	73
4.6	Laser Diffraction Particle Size Analysis of RS-IRMOF-8 and RS-IRMOF-8-NO ₂	74
4.7	Surface Area and Porosity Analysis of IRMOF-8 and IRMOF-8-NO ₂	75

4.8	Hydrogen, Methane and Carbon Dioxide Adsorption Isotherms of IRMOF-8 and IRMOF-8-NO ₂	78
4.9	Analysis of Sticking Efficiencies of IRMOF-8 and IRMOF-8-NO ₂	83
4.10	Heat of Adsorption of IRMOF-8 and IRMOF-8-NO ₂	86
4.10	Conclusion.....	89
5	Nanoconfinement of NaAlH ₄ in IRMOF-8 (NaAlH ₄ @IRMOF-8).....	91
5.1	X-Ray Diffraction of NaAlH ₄ @IRMOF-8 and NaAlH ₄ @MC.....	92
5.2	Thermogravimetric Analysis of Bulk and Composite Materials.....	93
5.3	Surface Area and Porosity Analysis of Composites.....	95
5.4	Temperature Program Desorption (TPD) of Composite Materials.....	97
5.5	Residual Gas Analyzer (TPD-RGA analysis) of NaAlH ₄ @IRMOF-8.....	98
5.6	Conclusion.....	99
6	Summary of the Research.....	100
7	References.....	104
8	Appendix.....	115
	Presentations (Oral and Poster).....	115
	List of Publications.....	116
	Curriculum Vitae.....	117

LIST OF TABLES

Table 1.1 Desorption of NaAlH_4 under Argon Atmosphere.....	8
Table 3.1 XRD reflections and d-spacings of RS-IRMOF-8 and C-IRMOF-8.....	53
Table 3.2 Summary Synthesis Parameters and Results of C-IRMOF-8.....	62
Table 3.3 Summary Synthesis Parameters and Results of RS-IRMOF-8.....	62
Table 4.1 Physisorption Properties of IRMOF-8- NO_2 , and IRMOF-8.....	77
Table 4.2 Methane Adsorption and Sticking Factor of IRMOF-8- NO_2 , and IRMOF-8.....	82
Table 4.3 Carbon Dioxide Adsorption and Sticking Factor of IRMOF-8- NO_2 , and IRMOF-8.....	83
Table 5.1 Physisorption and Thermodynamic Properties of Bulk and Nanoconfined Materials.....	96

LIST OF FIGURES

Figure 1.1: Hydrogen Density and Accessibility in Different Storage System.....	4
Figure 1.2: Illustration of MOF Synthesis and Chemical Composition.....	16
Figure 1.3: A Large Series of Isorecticular Metal–Organic Frameworks (IRMOFs).....	16
Figure 1.4: IUPAC Classifications of Adsorption Isotherms.....	23
Figure 1.5: Potential Energy Curve for Chemisorbed and Physisorbed Hydrogen.....	25
Figure 2.1: Glove box.....	36
Figure 2.2: X’pert Pro PANalytical X-ray Diffractometer.....	37
Figure 2.3: Thermogravimetric Analyzer.....	39
Figure 2.4: IRPrestige-21 Spectrometer.....	40
Figure 2.5: Oxford JEOL ECX 400 MHz Delta 2-NMR Spectrophotometer.....	41
Figure 2.6: Laser Diffraction Particle Size Analyzer.....	42
Figure 2.7: ASAP 2020 Surface Area and Porosity Analyzer.....	44
Figure 2.8: High Pressure Volumetric Analyzer (HPVA-100).....	46
Figure 2.9: Advanced Automated Hydriding Apparatus.....	48
Figure 2.10: Residual Gas Analyzer coupled to Advanced Materials PCI unit.....	49
Figure 3.1: XRD Patterns of Reactants (a) 2,6-H ₂ NDC, (b) Zn(NO ₃) ₂ ·6H ₂ O and products (C-IRMOF-8) Prepared by a Convectional One-spot Solvothermal Method at (c) 80 °C, (d) 100 °C, (e) 120 °C, (f) 150 °C.....	52
Figure 3.2: XRD Patterns of Reactants (a) 2,6-H ₂ NDC, (b) Zn(NO ₃) ₂ ·6H ₂ O and products (RS-IRMOF-8) Prepared by Rapid Solvothermal Method at (c) 100 °C, (d) 120 °C, (e) 150 °C, (f) 155 °C compared to (g) C-IRMOF-8 at 120 °C.....	53

Figure 3.3: FTIR Spectra of Reactants (a) 2,6-H ₂ NDC (b) Zn(NO ₃) ₂ .6H ₂ O and Products (RS-IRMOF-8) at (c) 100 °C, (d) 110 °C, (e) 130 °C, (f) 150 °C, (g) 155 °C Compared to a Convectional One-spot Solvothermal Method (h) C-IRMOF-8 at 120 °C.....	55
Figure 3.4: TGA Curves of the as-synthesized IRMOF-8 using the Rapid Conventional Solvothermal Method (RS-IRMOF-8) at Different Temperatures (b) 120 °C(c) 130 °C (d) 150°C (e) 155°C compared to (a) C-IRMOF-8 Prepared by a Convectional One-spot Solvothermal Method at 120 °C.....	56
Figure 3.5: Laser Diffraction Particle Size of RS-IRMOF-8 and C-IRMOF-8.....	57
Figure 3.6: N ₂ adsorption-desorption Isotherms of C-IRMOF-8 Synthesized by a Conventional One-spot Solvothermal Method at (a) 120 °C,(b) 110 °C,(c) 100 °C,(d) 130°C. Open symbols represent desorption and filled symbols represent adsorption.....	60
Figure 3.7: N ₂ Adsorption- desorption Isotherms for IRMOF- 8 Prepared by the Rapid Solvothermal Method (RS-IRMOF-8) (a) 155 °C (c) 150 °C, (d) 130 °C, (e) 120 °C Compared to Conventional One-spot Solvothermal Method (b) (C-IRMOF-8) at 120 °C. (Open symbols represent desorption and filled symbols represent adsorption).....	61
Figure 3.8: Correlation Between SSA and Temperature of IRMOF- 8 Prepared by the Rapid Solvothermal Method (RS-IRMOF-8(c &d)) Compared to a Conventional One-spot Solvothermal Method(C-IRMOF-8 (a & b)).....	61
Figure 3.9: Hydrogen Sorption Isotherms for C-IRMOF-8 at (a) 120 °C, (c) 110 °C and RS-IRMOF-8 at (b) 150 °C, (d) 130 °C, (e) 120 °C and (f) 155 °C at 1 atm.....	64
Figure 4.1: XRD Pattern of Reactants and Products (d) IRMOF-8-NO ₂ (e) IRMOF-8.....	67
Figure 4.2: Comparative FTIR Patterns of Organic Linkers and Products, Before and After Gas Sorption Analysis (■ represents the nitro functional group, ● is the carboxylic functional group).....	69
Figure 4.3(a): ¹ H NMR of 4,8-Dinitro-2,6-H ₂ NDC and 2,6-H ₂ NDC.....	71
Figure 4.3(b): ¹³ C NMR of 4,8-Dinitro-2,6-H ₂ NDC and 2,6-H ₂ NDC.....	71
Figure 4.4:TGA Curve of Organic Linker (b, c) and Products (a, d).....	72
Figure 4.5a: RGA Signal of Degassed IRMOF-8-NO ₂	73
Figure 4.5b: RGA Signal of Degassed IRMOF-8.....	74

Figure 4.6: Particle Size Distribution of IRMOF-8 and IRMOF-8-NO ₂	75
Figure 4.7: (a) LN ₂ Nitrogen Adsorption- desorption Isotherms of (a) Pure IRMOF-8 (b) IRMOF- 8-NO ₂ (□ is desorption ■ is adsorption isotherm). The Inset is LN ₂ Nitrogen-Adsorption- desorption Isotherms for IRMOF- 8-NO ₂	76
Figure 4.8. Low Pressure H ₂ Sorption Isotherm of (a) Pure IRMOF-8 (b) IRMOF-8-NO ₂ at -196 °C.....	79
Figure 4.9: High Pressure Hydrogen Sorption Isotherms (a) Pure IRMOF-8 (b) IRMOF-8-NO ₂ at -196 °C. The Inset Shows the High Pressure H ₂ Isotherm at Different Temperatures for IRMOF-8-NO ₂	80
Figure 4.10a: Low Pressure CH ₄ Storage Capacities of IRMOF-8-NO ₂ and pure IRMOF-8 at 0 and 25 °C.....	80
Figure 4.10b: Low Pressure CO ₂ Storage Capacities of IRMOF-8-NO ₂ and Pure IRMOF-8 at 0 and 25 °C.....	81
Figure 4.11a: High Pressure CH ₄ Storage Capacities of IRMOF-8-NO ₂ and Pure IRMOF-8 at 0 and 25 °C.....	81
Figure 4.11b: High Pressure CO ₂ Storage Capacities of IRMOF-8-NO ₂ and Pure IRMOF-8 at 0 and 25 °C.....	82
Figure 4.12: Sticking Factor versus Temperature for the Adsorption of Hydrogen on IRMOF-8-NO ₂ and Pristine IRMOF-8 at High Pressure.....	84
Figure 4.13: Sticking Factor versus Heat of Adsorption of Gases on IRMOF-8 and IRMOF-8-NO ₂	85
Figure 4.14: Sticking Factor versus Molecular Weight of Gases on IRMOF-8 and IRMOF-8-NO ₂	85
Figure 4.15: Van't Hoff Plots for Heat of Adsorption of IRMOF-8-NO ₂ at High Pressure.....	88
Figure 4.16: Isothermic Heat of Adsorption of IRMOF-8-NO ₂ and Pristine IRMOF-8 versus Hydrogen Loading at High Pressure.....	89

Figure 5.1: X-ray Diffraction of Bulk NaAlH ₄ , IRMOF-8, Mesoporous Carbon (a, b, d) and Nanoconfined NaAlH ₄ @IRMOF-8 (c) and NaAlH ₄ @MC (e).....	93
Figure 5.2: TGA-DTA of Bulk IRMOF-8, MC and Nanoconfined NaAlH ₄ in IRMOF-8 and MC.....	94
Figure 5.3: Nitrogen Isotherms of Bulk and Nanoconfined NaAlH ₄ in IRMOF-8 and MC.....	95
Figure 5.4: TPDs of Pristine and Nanoconfined NaAlH ₄ in IRMOF-8 and MC.....	97
Figure 5.5: RGA of Bulk and Nanoconfined NaAlH ₄ in IRMOF-8 and MC.....	98

CHAPTER ONE

1 INTRODUCTION AND MOTIVATION

The world depends largely on the limited supply of fossil fuels such as coal, oil and natural gas for its energy need. With the increasing standard of living and ever growing world population, it has been envisaged that the world will deplete its supply of fossil fuels [1-10]. Their combustion is responsible for increasing the greenhouse gases (CO_2 ; 56 % and CH_4 ; 18 %), although the methane level is beginning to be stabilized and it also has been used as alternative energy source for automobiles [2, 11]. The consumption of petroleum in 2005 was about 83 million barrels and this resulted in the release of several billion metric tons of carbon dioxide into the atmosphere. This is expected to increase steadily in the next 50 years [1, 2, 4-6, 9].

The dramatic increases in the price of gasoline in some countries are also a motivation for an alternative, sustainable, clean and renewable energy or energy carrier. Two-thirds of the oil used in the United States of America goes to the transportation industry. The alternative, clean and renewable energy carrier or source should be able to meet the transportation industry [1-14]. The various sources of energy are accompanied by their draw backs. Already mentioned, chemical energy (fossil fuels) leads to the production of greenhouse gases causing global warming. Another alternative is the use of nuclear energy which is a primary energy source in France (80%). The problems of long term storage of nuclear waste and the dangers of explosion like Chernobyl prevents many

countries from investing significantly in nuclear energy [15-20]. Solar and wind energy require large surface area, high cost and the energy is fluctuating. Other forms of energy are hydroelectric and geothermal. The major obstacle to all these other energy sources is that they are unevenly distributed. Pollution occurring from the transportation sector as a result of the use of chemical energies (fossil fuels) is problematic [5, 13, 15, 17, 19, 20].

It is therefore very urgent to propose solutions to avoid or limit such problems. Presently, two main technologies are considered as energy storage or carriers for mobile applications: the first is batteries for electrical vehicles and the other is hydrogen or methane for ICE (internal combustion engine) or H₂-FCV (fuel cell vehicle) and methane for Natural gas vehicle (NGV) [1-14, 16, 17]. Batteries do not require additional synthetic fuels and are therefore promising. However, low cycling stability, long recharging time, the heavy weight of the batteries and the large volume occupied by batteries are major drawbacks [2, 10, 17]. The use of hydrogen or methane as energy carriers for automobile applications is very promising. A major bottleneck is the lack of an efficient storage system for it to be used in hydrogen-fuel cell driven vehicles or natural gas vehicle [1, 3, 11, 12, 14, 16, 18].

Dual fuel ICE vehicles have been produced to run on both hydrogen and gasoline. This technology in automobile application has an efficiency of up to 25 % when compared to hydrogen which has been used to power FCV with an efficiency of 45 %. The use of hydrogen in ICE produces water as a byproduct as well as small amount of nitrogen oxide, an air pollutant [15, 17].

1.1 PROPERTIES OF HYDROGEN

As the most promising candidate for the replacement of current carbon-based energy sources; hydrogen can be a safe and convenient vector of energy. It holds promise as an efficient and clean alternative [1-8, 17, 18-25]. Hydrogen is the most abundant element on earth and is nearly an ideal fuel because it can be generated from a diverse number of renewable feedstocks (biomass, hydro, solar, geothermal and wind) as well as natural gas from fossil fuels and nuclear energy. It can be converted to a desired form of energy without releasing harmful emissions at the point source [1, 5, 6, 17-20]. Gravimetrically, hydrogen has nearly three times the energy content of gasoline (120 MJ/kg for hydrogen versus 44 MJ/kg for gasoline). On a volumetric basis, hydrogen has only a quarter of the energy content of gasoline (8.4 MJ/L for liquid hydrogen and 4.4MJ/L for 10,000 psi versus 32 MJ/L for gasoline) due to the binding of hydrogen. The current methods for hydrogen storage are in compressed tanks or in liquid form. These storage methods however have their setbacks which will be discussed in the section below [1, 4, 5, 10, 12, 13, 17].

1.2 HYDROGEN STORAGE METHODS AND DEPARTMENT OF ENERGY GOALS

Effective hydrogen storage is needed for fuel-cell vehicles. Single-walled carbon nanotubes, zeolites, activated carbon, and metal hydrides have all been evaluated as possible candidates, but none have met the U.S. Department of Energy goals (DOE) of 5.5 wt % and 40 g/L for 2010 with an ultimate goal of 7.5 wt. % and 70 g/L all at an operating temperature of -40 to 100 °C and 100 bar. Other targets set by DOE are

refueling time of 5 minutes and a material that can be recycled 1000 times. For a means of storage to be useful, two conditions are important. It must first hold enough H_2 at the appropriate temperatures and secondly, release the H_2 easily whilst not requiring more energy to get it out than was used to store the H_2 . An important challenge for the use of hydrogen as an energy carrier is its compact and safe storage [1-10]. The figure below compares the accessibility and density of hydrogen in the available storage materials. While hydrogen densities increase from compressed gas tanks to storage in various solid forms, its accessibility however decreases.

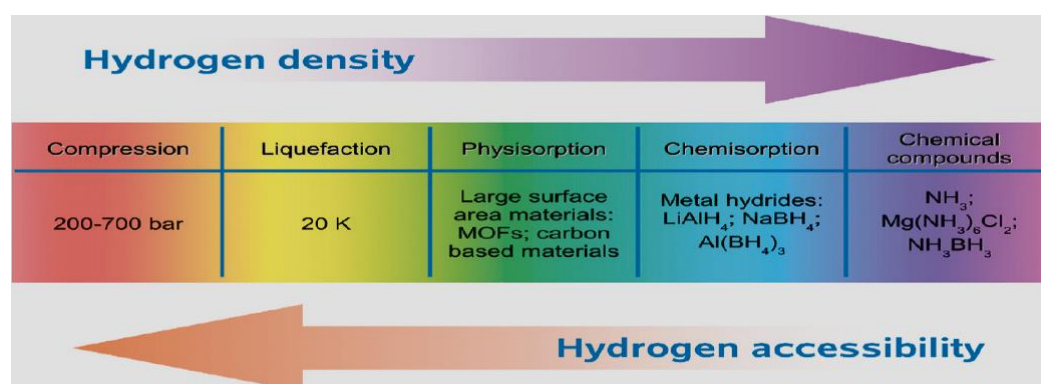


Figure 1.1 Hydrogen density and accessibility in different storage system [1]

1.2.1 COMPRESSED HYDROGEN TANKS

The conventional methods of hydrogen storage are in high-pressure gas cylinders. The gas cylinders are very massive and hold little hydrogen for their weight. Compressed hydrogen storage has become the current standard for fuel cell demonstration vehicles [1-20]. Newer carbon fiber composite tanks operating at 350 bar (5000 psi) have exceeded 6 wt% hydrogen storage density, but the tank volume is still in excess of the goals by a factor of two or more. Increasing compressed hydrogen pressures from 350 bar to 700 bar

(10,000) can reduce the tank volume by about 33%, but at higher safety risk, increased compression energy requirements and cost. The driving range of H₂-FCV with compressed tanks depends on the vehicle type, amount of stored hydrogen and design. For example, the General Motors fuel cell vehicle (Opel Zafira minivan with a weight of 1590 kg) is specified for a 270 km (168 mile) driving range with 3.1 kg of hydrogen at 10,000 psi. A longer driving range can be achieved by increasing the amount of compressed hydrogen gas beyond 3 kg, but at more cost, weight and reduced passenger and cargo space on the vehicle. Volumetric capacity, limits of high pressure and cost are thus key challenges for compressed hydrogen tanks. Dramatic cost reductions would be needed to meet the DOE goals [10, 12, 13, 16-20].

1.2.2 CRYOGENIC HYDROGEN TANKS

Hydrogen only liquefies at -251.9 °C which imposes impractical limitations on its use. Liquid hydrogen storage can meet or exceed many of the gravimetric and volumetric density targets, but costs and energy use, especially with respect to liquefaction are high. Liquid hydrogen storage requires dealing with the hazard of handling cryogenic hydrogen at 20 degrees above absolute zero [10, 17-20]. Liquid hydrogen (LH₂) tanks store more hydrogen in a given volume than compressed gas tanks, since the volumetric capacity of liquid hydrogen is 70.8 g/L (compared to 39 g/L at 700 bar). Key issues with LH₂ tanks are hydrogen boil-off, energy required for hydrogen liquefaction (requires 30% of its energy value) and cost of the tank. The driving range for vehicles using liquid hydrogen, excluding the effects of boil-off, can be longer than that for compressed hydrogen. For example, the Opel Zafira minivan is specified with a driving range of 400 km (249 mile)

with 4.6 kg liquid hydrogen, versus 270 km (168 mile) described above for the 700 bar tank [12, 13, 17, 19, 20].

To get the maximum possible driving range, hydrogen loss as a result of boil-off must be minimized or eliminated. Hydrogen boil-off is also considered an issue in terms of refueling frequency, cost, energy efficiency and safety, particularly for vehicles parked in confined spaces such as parking garages. The amount and rate of hydrogen boil-off depends on the following factors; amount of hydrogen stored, effectiveness of the thermal insulating material, ambient conditions, vessel geometry, and length of time between driving. The amount of thermal insulation affects the system-level gravimetric and volumetric capacity, so there are trade-offs to consider among all of these different factors. Hydrogen is lost when the system has been dormant (without driving) and the pressure within the liquid tank reaches the boil-off pressure. System designs that have a capacity for higher levels of gas pressure (“cryo-compressed” tanks) can greatly improve the degree of dormancy and reduce boil-off loss. However, even with minimal or no boil-off, the energy required to liquefy hydrogen, over 30% of the lower heating value of hydrogen, remains a key issue and impacts fuel cost as well as fuel cycle energy efficiency. New approaches that can lower these energy requirements and thus the cost of liquefaction are needed [4, 12, 13, 15, 17-20].

1.2.3 SOLID STATE HYDROGEN STORAGE

The most promising alternative storage option is finding a material that traps a large quantity of hydrogen at room temperature and atmospheric pressure. A promising option is reversible solid state hydrogen storage. In solid state hydrogen storage, the

binding of hydrogen atom or molecule unto the sorbate materials is much stronger in ionic, ionic-covalent or a quasi-molecular bond rather than the usual van der Waals attraction in compressed tanks. The strong or weak interactions give rise to the phenomenon of chemisorption or physisorption. This stronger bonding allows for optimizing the volumetric setback obtained with compressed tanks [1, 4-6, 17, 18].

1.2.3.1 CHEMISORPTION OF HYDROGEN ATOMS IN METALS

The hydrogen molecules split into hydrogen atoms on the solid support to form chemical bonds forming metal hydrides or chemical hydrides depending on the nature of the solid support material [3, 4]. Metal hydrides exhibit high hydrogen storage capacity at low pressures and moderate temperatures and also have high volumetric capacities. Their stored hydrogen density is near that of liquid hydrogen. Their inherent barrier is in dissociating the H-H bond to store the hydrogen and recombining the hydrogen atoms to desorb the hydrogen molecule [1, 3, 4, 13, 18]. They also have high binding energies for binding the hydrogen atoms to the metal host (60-100 kJ/mol) [1, 3, 4, 13, 17]. The absorption of hydrogen by metal hydride is an exothermic reaction. Heat removal during refueling becomes the controlling factor on refueling time. The heat therefore generated during the charging and discharging process must be managed effectively for on-board application [1, 3, 4, 13].

However, some metal hydrides have the potential for reversible on-board hydrogen storage at the low temperature and pressure required for FCVs (with a P-T window of 1-10 atm and 25-120 °C). However, they have low gravimetric capacity, too

high of a cost, and their weight are their main disadvantages. They require the least amount of energy to operate. LaNi_5H_6 is one of such metal hydride [13, 18]. Much effort is underway to find lighter materials. Generally, metal hydrides exhibit too slow hydrogen release and uptake and a too high thermodynamic stability [15, 17].

1.2.3.2 COMPOUNDS WITH IONIC CHARACTER (COMPLEX HYDRIDES)

The complex hydrides are comprised of light metal hydrides and chemical hydrides. Magnesium hydride (MgH_2), salts of $[\text{AlH}_4]^-$ (alanates), $[\text{BH}_4]^-$ (borohydrides) and, $[\text{NH}_2]^-$ (amides) such as, sodium alanate (NaAlH_4), magnesium borohydrides $\{\text{Mg}(\text{BH}_4)_2\}$ and lithium amide (LiNH_2). In these materials, the hydrogen is covalently bonded to the central atom in the complex and they contain a high density of hydrogen (5.5-18.5 wt. %). They were initially not considered as suitable candidates for hydrogen storage due to their poor kinetics, reversibility and thermodynamics. LiBH_4 and $\text{Mg}(\text{BH}_4)_2$ have high gravimetric capacity but suffer lack of reversibility. This is attributed to the existence of stable polyhedral complexes containing $[\text{B}_{12}\text{H}_{12}]^-$ Orimo et. al.[1, 5, 17, 18]. NaAlH_4 is the only complex metal hydride identified so far that combines relatively high gravimetric hydrogen content with suitable thermodynamic properties. NaAlH_4 is known to decompose in three distinct steps.

TABLE 1.1 Decomposition of NaAlH_4 under Argon Atmosphere

Equation	Decomposition Pathway	H_2 wt%	T	kJ/mol $[\text{H}_2]$
1	$3\text{NaAlH}_4(\text{s}) \leftrightarrow \text{Na}_3\text{AlH}_6(\text{s}) + 2\text{Al}(\text{s}) + 3\text{H}_2(\text{g})$	3.7	180-186 °C	37
2	$\text{Na}_3\text{AlH}_6(\text{s}) \leftrightarrow \text{NaH}(\text{s}) + \text{Al}(\text{s}) + 11/2\text{H}_2(\text{g})$	1.85	240-250 °C	47
3	$\text{NaH}(\text{s}) \leftrightarrow \text{Na}(\text{l}) + 1/2\text{H}_2(\text{g})$	1.85	>425 °C	56

Attempts have been made to decrease the hydrogen desorption temperature of NaAlH_4 which is approximately 186 °C (no hydrogen is released in undoped NaAlH_4 at 30-100 °C). The pioneering works of Bogdanovic and Schwickardi [5, 6] introduced Ti-containing compounds into NaAlH_4 to catalyze the hydrogen absorption and desorption under milder conditions. These attempts have been limited by particle agglomeration and grain growth of the NaAlH_4 upon hydrogen release and uptake cycles at elevated temperatures and also by low maximum reversible storage on multiple cycles at temperatures less than 120 °C. High pressures (>200 bar) and long release times are needed also for reloading depleted NaAlH_4 [5, 6, 19-20].

The ideal enthalpy for hydrogen release in solid state storage should be in the range of 35-45 kJ/mol $[\text{H}_2]$ for operation with PEM fuel-cell temperatures. A number of approaches have been investigated to alleviate the problem of thermodynamics and stability such as cation/anion substitution, additives of hydrides of transition metals and size effects. Reducing the size of NaAlH_4 to the nanoscale dimension is a potential route to enhance its hydrogen storage capacity. Ball milling and nanoconfinement of metal hydrides in scaffolds (mesoporous and microporous materials) are two potential techniques for size reduction. However, the positive effects (faster dehydrogenation kinetics and better reversibility than pristine sodium alanate) of ball milling diminish due to the inevitable particle agglomeration driven by high surface energy and the segregation of the Al domain after several cycles. Nanoconfinement either by wet infiltration or thermal melt infiltration on the other hand helps to maintain a stable nanostructure during cycling and maintain the nano-effects [5, 6, 13, 17, 18].

A reduction in dehydrogenation temperature of NaAlH_4 deposited on carbon nanofiber from 186 °C to 70 °C as the particle size decreases from 1-10 μm to 2-10 nm has been reported. Metal-organic frameworks (MOF) with pore sizes between 1-2 nm also reduced the dehydrogenation temperature to 70 °C [5, 6, 17]. The nanoconfinement of NaAlH_4 in isorecticular metal-organic framework-8 (here known as NaAlH_4 @IRMOF-8) is therefore studied in this dissertation.

1.2.3.3 PHYSISORPTION OF HYDROGEN IN POROUS MATERIALS

Porous materials are carbon based materials known as sorbent such as fullerenes, nanotubes, graphenes, zeolites, ordered mesoporous carbon, certain clathrates and metal-organic frameworks. They are able to reversibly bind and release hydrogen by weak attractive forces at low temperatures. They have fast kinetics and their enthalpy values are usually between 4-7 kJ/mol. Only a small amount of heat is released during on-board refueling which is an advantage over chemical hydrides [1-10, 12-14, 16-40]. Metal-organic frameworks have an advantage over other porous materials. The presence of unsaturated metal centers (UMCs) generated during activation or degassing of the materials by removal of coordinated solvent results in more interaction between hydrogen and the UMCs. This interaction is much higher than in pure carbon materials. The isosteric heat (enthalpy) thus tends to be as high as 12-13 kJ/mol. Compared to other porous materials, they also have higher surface area [12, 18].

1.3 PROPERTIES OF METHANE AND STORAGE METHODS

Natural gas is a mixture of ethane, other hydrocarbons, carbon dioxide, nitrogen and the main component being methane (95 %). The gravimetric heat of combustion of methane is comparable to gasoline (55.0 MJ/kg vs. 44.5 MJ/kg). It has no quadrupole moment. It is polarizable with a spherical conformation. Compared to petroleum oil, it can provide much more energy because of its higher hydrogen-to-carbon ratio which will also result in lower carbon emission. The barrier to the methane economy is the lack of a safe and effective storage method for mobile applications. The current methods of storage are as compressed natural gas (CNG) and liquefied natural gas (LNG) [11, 12, 14].

1.3.1 COMPRESSED NATURAL GAS (CNG) TANKS

Compressed natural gas tanks for automobile applications can hold up to 200 bar (3000 psi) of methane gas and can offer about 26 % of the volumetric density of gasoline. Safety at such high a pressure is a concern, also a car with dual CNG and gasoline as fuel requires two separate tanks which consequently adds weight to the vehicle and reduces cargo space [2, 16].

1.3.2 LIQUIFIED NATURAL GAS (LNG) TANKS

Liquefied natural gas as a method of methane storage can provide about 72 % of the volumetric energy density of gasoline. This can be achieved also at cryogenic temperatures just like hydrogen, but at 112 K (-161.15 °C). Safety and energy input are also setbacks for implementing this technology [12, 14].

1.3.3 ADSORBED NATURAL GAS (ANG) AND DOE's GOAL

Adsorbed natural gas is the storage of methane on a porous adsorbent (solid state storage). The volumetric energy storage for methane at 500 psi in a porous material has been investigated to be 80% of that of that of CNG at 3000 psi. Unlike hydrogen storage in porous materials, the heat of adsorption of methane (~ 20 kJ/mol) is already within the target goal of the department of energy (DOE). DOE has set a target of 180 v/v or 18 wt % at ambient temperature and pressure at no more than 35 bar [11, 12, 31]. Some of the carbon materials already studied have reached the goal of DOE. However, the focus is on increasing the surface area of the porous sorbent due to low packing density [11, 12, 14, 16].

1.4 PROPERTIES AND METHODS OF CARBON DIOXIDE CAPTURE AND SEQUESTRATION

The capture of CO₂ at the power plant, its transport to an injection site and subsequent sequestration in geological formations such as saline formations, depleted oil and gas field and unmineable coal seams for a very long time (thousands of years) is an approach that is promising to reduce CO₂ emission. However, the promise of this approach can only come to fruition if cost is effectively reduced. The CO₂ capture from coal-derived power generating plants can be achieved by post or pre-combustion and oxy-combustion. [5, 9, 14, 40].

The capture and the separation cost of CO₂ sequestering are a significant portion of reducing CO₂ emission. At the present, a variety of separation techniques are being pursued. They are: gas phase separation, absorption into liquid, adsorption on a solid and

hybrid processes [9]. The Department of Energy's (DOE's) goal is to have the necessary technology ready for large scale field testing, should it become necessary to impose mandatory limits on CO₂ emissions. The specific goal is to have technologies developed by 2012 that have advanced beyond the pilot scale and are ready for large scale field tests. The goal is to achieve 90% CO₂ capture at an increase in the cost of electricity of less than 20% for post-combustion and oxy-combustion and less than 10% for pre-combustion capture. Capture and separation costs are a significant portion of the cost to sequester CO₂ [9, 11].

1.4.1 CARBON DIOXIDE CAPTURE AND SEQUESTRATION

For the purpose of this thesis, processes involved in post-combustion CO₂ capture shall be discussed. This is because in spite of its technical challenge, in post-combustion, CO₂ is removed from the flue gas by combustion using air (which contains four-fifths nitrogen). The flue gas generated is at atmospheric pressure with a CO₂ concentration less than 15 % (the CO₂ partial pressure is typically less than 0.15 atm). Therefore the driving force for CO₂ capture from flue gas is low. Thus, there is a need for the development of cost effective advanced capture processes. Post-combustion capture methods have the greatest near-term potential for reducing greenhouse gas (GHG) emission because it can be fitted to existing units that generate about two-thirds of the CO₂ emissions in the power sector [9, 11]. Other CO₂ capture methods are discussed in detail elsewhere [9].

Amine-based systems (e.g. monoethanolamine MEA): this post-combustion CO₂ capture method involves the reaction of primary, secondary or tertiary amines with CO₂ to form water soluble compounds and capture CO₂ from streams with a low CO₂ partial

pressure. However, the capacity is equilibrium limited, it is very costly and the efficiency is reduced [9, 11, 14].

Carbon-based systems (e.g. Potassium carbonate/piperazine K_2CO_3/PZ): these were developed at the University of Texas at Austin. The carbonate compounds are based on the ability of a soluble carbonate to react with CO_2 to form a bicarbonate that releases CO_2 on heating, which then reverts to a carbonate. This has a significant advantage over the MEA or amine-based system in that the carbonates require significantly lower energy for regeneration. The absorption rate is 10-30 % faster than a 30 % solution of MEA. There is also a high loading capacity of 40% versus about 30% for MEA but the piperazine catalyst is more expensive than MEA [9].

Aqueous ammonia (e.g. ammonium carbonate $(NH_4)_2CO_3$): this is similar in operation to amine-based systems. In the ammonia-based wet scrubbing process of CO_2 capture, ammonia and its derivatives react with CO_2 via various mechanisms. The ammonia carbonates (AC), CO_2 , and water react to form ammonium bicarbonate. This method has the advantage of lower heat of reaction than the amine system resulting in energy saving, high CO_2 capacity, lack of degradation during absorption and regeneration, low cost and tolerance to oxygen in flue gas. However, the major setback is in its high volatility compared to MEA. There is also the loss of ammonia during regeneration [9, 14].

Adsorption-based system: the CO_2 is adsorbed on solid state materials with large surface areas such as zeolites, activated carbon and metal-organic frameworks (MOF). The cost of regeneration is a major drawback for using activated carbon and zeolites as

well as limited surface areas, limitation in structural design, and the limited possibility for surface modification. MOFs are a new class of hybrid materials built from metal ions with well-defined coordination geometry and organic linkers as bridges. They have pore structures or channels that can adsorb CO₂. With their exceptional or high surface areas, high storage capacity is possible and the heat requirement for recovery of the adsorbed CO₂ is low [9, 11, 14].

1.5 METAL-ORGANIC FRAMEWORKS

Metal-organic frameworks have attracted an enormous amount of attention in recent years as materials for gas sorption, gas separation, drug delivery and catalysis. MOFs consist of metal-oxygen vertices (secondary building units, SBU) held together with organic linkers creating pores and channels (Fig. 1.2). They are highly crystalline, porous and can be made inexpensively in large quantities [1-4, 7-14, 37-60]. They are comparatively light and stable over a fairly wide range of temperatures and pressures [4-9, 11, 12,]. MOFs can be tailored fairly easily by changing metals and organic ligands. The reactants are mixed in high boiling point polar solvents such as water, dialkyl formamide, dimethyl sulfoxide and acetonitrile under mild temperatures (below 300 °C) and autogenous pressures (up to 100 atm) [1, 3-8, 12, 37-39]. Since most products can be considered kinetically driven and lie on local thermodynamic minima, factors such as solubility of the organic linker and metal salt, solvent polarity, ionic strength of the medium, temperature and pressure play critical roles in determining the character of products. Indeed, slight perturbations in synthetic parameters have been the basis for the preparation of what seems to be a flood of new MOF compounds [31, 39,].

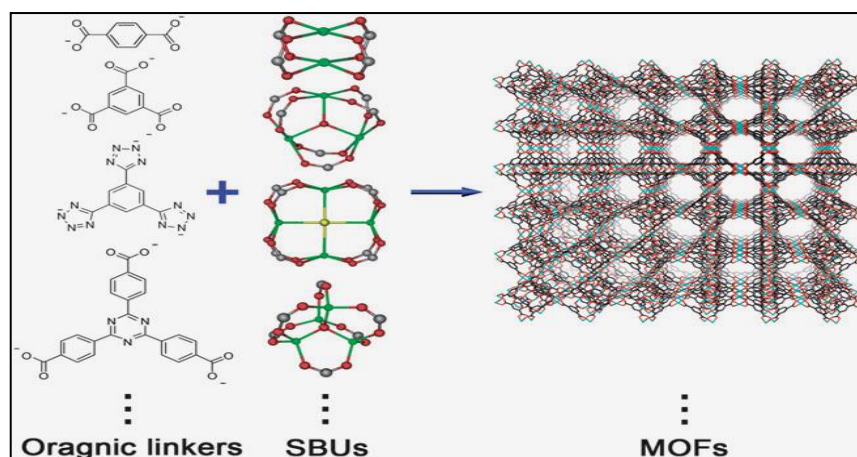


Figure 1.2 Illustration of MOF synthesis and chemical composition [4]

With the concept of reticular synthesis, the pore sizes of MOFs can be easily tuned (angstroms to nanometers) by controlling the length of the organic linker to give new MOFs with similar topology but with higher surface area, smaller pores or more rigid structure[14, 39]

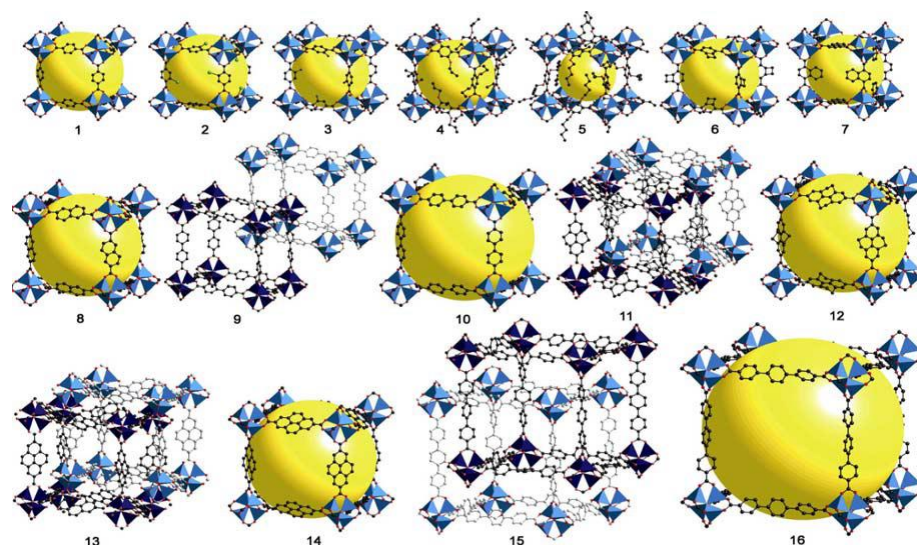


Figure 1.3 Isorecticular metal–organic frameworks (IRMOFs). Members sharing the same cubic topology are (IRMOF-1 to -7) and in length (IRMOF-8 to -16). The expansion of the links increases the internal void space (represented by yellow spheres), it also allows the formation of catenated phases (IRMOF-9, -11, -13 and-15) [39].

The thermal stability of MOF materials is expected to be lower than that of zeolites and zeolite analogues. The main reason for this is the lower metal linker binding energies as compared to the strong Si–O and Al–O bonds in the zeolites. Nevertheless, many MOF materials show relatively high thermal stabilities, uniform pore sizes, large effective surface area and pore volume and decomposition often occurs at temperatures above 573 K which is sufficient for the present application [4, 9, 11, 12, 31, 39].

MOFs not only have coordination bonds but also other weak interactions or non-covalent bonds (H-bonds, π –electron stacking or van der Waals interaction), resulting in the structural transformation ability. The transition metal ions (d and f blocks) and electron acceptors (Lewis acid) are usually used as joints [4, 34]. Because of the variety of the coordination numbers of metal ions (SBU), one can obtain various coordination geometries (e.g. linear, T-shape, trigonal-planar, tetrahedral, octahedral), as seen in Figure 1.2 above. Consequently, various structural architectures of 1D, 2D or 3D conformations can be formed [14, 34]. The linkers are electron donors (Lewis bases), in particular, the highly symmetrical multidentate ligands with N, O and S donor atoms [14, 31]. The use of MOFs as sorbents for storage for gases has been studied by many groups. Bhatia and Myers have initially studied the optimum conditions for adsorptive gas storage (hydrogen storage). They found that adsorption of significant amounts of H₂ at room temperature and moderate pressure requires a heat of adsorption for H₂ of about 15 kJ/mol [4, 12, 16].

The first notable characteristic of porous materials is specific surface area (SSA). There is a positive relationship between the surface area and the hydrogen uptake in

carbon-based sorbents. Theoretically, it has been determined that a minimum surface area of $\sim 1400 \text{ m}^2/\text{g}$ is needed for a material to reach an excess hydrogen adsorption of 6 wt% (or $\sim 2100 \text{ m}^2/\text{g}$ for 9 wt %) Zhao et. al.[4]. Among MOFs, Yaghi and co-workers first reported that a MOF (MOF-5 also known as isorecticular metal-organic framework, IRMOF-1) had a SSA of $3534 \text{ m}^2/\text{g}$. The inorganic $[\text{OZn}_4]^{6+}$ groups are joined to an octahedral array of $[\text{O}_2\text{C}-\text{C}_6\text{H}_4-\text{CO}_2]^{2-}$ (1, 4-benzenedicarboxylate, BDC) to form a porous cubic framework. It had a 4.5 wt% H_2 uptake at 78 K and 0.8 bar and it stored 1 wt% of H_2 at 298 K and 20 bar. Although the H_2 uptake for MOF-5 at 77 K was reported again later as 1.30 wt% at 1.01 bar (1 atm) and 1.51 wt% at 1.13 bar, the result was still exciting enough to encourage many researchers to study this topic. The recyclability of the sample has also been tested and was found to adsorb and desorb hydrogen 24 times. MOF-177 ranks highest for gravimetric hydrogen uptake, with a value of 7.6 wt% at 77 K and 70 bar. It also has a very large surface area of around $\sim 4500 \text{ m}^2/\text{g}$ [2-4, 7, 8, 12]. In a latter study by Saha et al.[7], the Langmuir surface area was found to be $5994 \text{ m}^2/\text{g}$ with excess hydrogen adsorption of 11.0 wt% and at ~ 100 bar and 77 K. IRMOF-20 with a SSA of $4593 \text{ m}^2/\text{g}$ at 77 K and 70-90 bar had a hydrogen storage capacity of 6.5-6.7 wt%. IRMOF-6 on the other hand had a surface area of $3300 \text{ m}^2/\text{g}$, the hydrogen adsorption at 77 K and 45 bar was reported as 4.8 wt% [2-4, 7, 14]. Another well studied MOF, is $\text{Cu}_3(\text{BTC})_2$ also known as HKUST-1 or MOF-199. It has a Langmuir surface area of about $\sim 2300 \text{ m}^2/\text{g}$, the hydrogen adsorption at 50 bar and 77 K is 3.6 wt%. MIL-101, on the other hand, possesses a higher surface area (Langmuir surface area is ~ 5500 or $5900 \text{ m}^2/\text{g}$), the hydrogen adsorption capacity is 6.1 wt% at 77 K and 80 bar. The current

record for surface area is held by UMCM-2, which possesses an exceptional surface area of over 6000 m²/g with a hydrogen storage capacity of 6.9 wt % at 46 bar and 77 K. In the above examples, the binding energies are less than 10 kJ/mol and the hydrogen uptake dropped significantly when the temperature was raised to ambient temperature to value ≤ 2 wt%. [2-4, 7, 10, 12, 14].

Recent theoretical and experimental studies have demonstrated that an enthalpy value of 20-25 kJ/mol is needed for ambient hydrogen energy storage and delivery between 30 and 1.5 bar of pressure [2, 3, 12, 14, 53]. Two main strategies are currently used to increase the hydrogen storage capacity in MOFs. The most important step towards practical application of MOF-based hydrogen storage is increasing the interaction between hydrogen and MOF. The other is increasing the internal surface area or pore volume [2-4, 12, 42]. There are several routes to increasing the binding energy of hydrogen to an MOF. These includes: catenation (interweaving or interpenetration) which divides larger pores into smaller ones, the introduction of unsaturated metal centers, linker functionalization which reduces the SSA and pore volumes, metal doping and spillover. The focus is on reducing the pore size since it has been shown in more recent studies that there is no direct correlation between surface area and hydrogen uptake. Many MOFs with high surface areas have rather low hydrogen storage capacity. Theoretical and experimental results have also shown that the optimal pore size is 6 Å. This is twice the kinetic diameter of hydrogen which is 2.9 Å and 9 Å for maximum hydrogen uptake at high pressure [2-4, 12, 14, 42].

In methane storage, Kuppler et al., Llewelly et al., and Ma et al. [11, 12, 14, 16] reported a series of MOFs that has been tested for their CH₄ storage capacity. The results show that the methane uptake in an MOF can exceed the DOE target. PCN-14 Cu₂(ADIP) with surface area of 1753 m²/g and pore volume of 0.87 cm³/g had a storage capacity of 220 v/v (16-18 wt % at 35 bar). The heat of adsorption was calculated to be 30 kJ/mol. In the same review article, other MOFs studied were PCN-11 Cu₂(SBTC) with surface area of 1931 m²/g, pore volume of 0.91 cm³/g, CH₄ capacity of 171 v/v (~14 wt % at 35 bar), and heat of adsorption of 14.6 kJ/mol. HKUST-1 (Cu₃(BTC)₂) gave a storage capacity of 15.7 wt% at 150 bar with surface area of 1502 m²/g and pore volume of 0.76 cm³/g or 200 cm³/g (109 v/v) at 35 bar. MIL-53(Al) Al(OH)(BDC) having surface area, pore volume and heat of adsorption of 1100 m²/g, 0.59 cm³/g and 17 kJ/mol respectively had a 155 v/v (10.2 wt %) methane adsorption capacity at 35 bar. MIL-53(Cr) Cr(OH)(BDC), had a SSA of 1100 m²/g, pore volume of 0.56 cm³/g and enthalpy of 17 kJ/mol. It also had a storage capacity of 10.2 wt % (165 v/v CH₄ storage capacity at 35 bar) .MIL-101 Cr₃FO(BDC)₃, was reported to have a storage capacity of 14.2 wt% which corresponds to 72 v/v at 125 bar. The surface area was 2693 m²/g with a pore volume of 1.303 cm³/g. The analyses were done at room temperature and the report shows that surface area is necessary but not a decisive factor for high methane adsorption. What is required is increasing the packing density. Just like hydrogen storage, factors such as surface areas, pore sizes, ligand functionalization, and heat of adsorption influence methane adsorption. For example, Kitagawa and coworkers demonstrated the

contribution of interpenetration for a series of azopyridine-based MOFs, with the highest of the series adsorbing 60 v/v (STP) [11, 12, 14, 16].

In the IRMOF series, the ability of IRMOF-6 (SSA of $\sim 2800 \text{ m}^2/\text{g}$) to uptake a higher amount of methane was ascribed to both the highly accessible surface area and the functionality of the ligand. In IRMOF-6, the phenyl ring of the typical BDC ligand was modified to generate 1,2-cyclobutane-3,6-benzenedicarboxylate. The resulting porous MOF was found to adsorb 155 v/v (STP) (or $240 \text{ cm}^3/\text{g}$) methane at 298 K and 36 atm, which was significantly higher than any zeolites material or any other porous MOF at the time. IRMOF-1 (MOF-5) and IRMOF-3 having surface areas of 2300 and $2500 \text{ m}^2/\text{g}$ had methane storage capacities of 135 and 120 v/v respectively. Theoretical simulations indicated that further functionalization of the ligand by insertion of an anthracene ring would improve methane uptake further, perhaps within reach of the DOE goal. Attempts to synthesize this proposed porous MOF, however, resulted in a material with very limited methane uptake, due to the ultramicroporous nature of the porous MOF, with pores too small to accommodate methane molecules [11, 12, 14, 16].

A few MOFs have shown good CO_2 storage capacity even at elevated pressures e.g. MOF-177, MIL-100 and MIL-101 [9, 11, 14]. Other advantages of MOFs are low energy requirement for regeneration, low cost, good thermal stability and tolerance to contaminants [9, 11, 14]. In a study by Llewellyn et al. [11], MIL-101 with BET surface area of $3780\text{--}4230 \text{ cm}^3/\text{g}$ was shown to adsorb a CO_2 record capacity of 40 mmol/g or $390 \text{ cm}^3 \text{ STP}/\text{cm}^3$ at 50 bar and 303 K. The heat of adsorption was calculated as 44 kJ/mol compared to conventional adsorbent material such as silicate, zeolite NaX and

SBA having CO₂ storage capacities of 2.5, 7.8 and 6 mmol/g respectively at same temperature and pressure of 30 bar. However, the heat of adsorptions is of the same order as the zeolites. Other metal-organic frameworks studied are HKSUT-1, IRMOF-1, and MOF-177 with CO₂ adsorption of 10.7, 21.7 and 33.5 mmol/g or 210, 290 and 320 cm³ STP/ cm³ at ~40 bar and 298 K respectively. CO₂ uptake can be enhanced in porous MOFs, by the incorporation of pendant alkylamine functionalities within the pores by the direct use of an amine-based bridging ligand, or via post-synthetic approaches. These can be achieved by covalently modifying a bridging ligand or grafting alkylamine functionality onto a UMC.

1.5.1 IUPAC CLASSIFICATION OF POROUS MATERIALS AND TYPES OF ADSORPTION ISOTHERMS

As defined by the International Union for Pure and Applied Chemistry (IUPAC), MOFs can be classified into three groups based on their pore sizes. Microporous materials are those with pore size less than 20 Å, mesoporous materials have pore sizes in the range of 20–500 Å and are more desirable in host–guest chemistry because they can accommodate larger guest molecules, while the microporous materials results in a stronger interaction between gas molecules and pore walls. This makes them good candidates for gas storage and separation. Macroporous materials have pore sizes greater than 500 Å [12, 18, 31 51].

Six different classes of isotherms were determined for physical adsorption according to the IUPAC classification. These correlate the amount of gas adsorbed with the applied gas pressure. Microporous materials typically exhibit a type I adsorption

isotherm which shows an initial steep increase, corresponding to progressive filling of the micropores. Then a plateau is reached at higher pressures, corresponding to monolayer coverage. Types II and IV isotherms are indicative of nonporous adsorbent or adsorbent with large pores (mesoporous materials). Types III and V arise when the adsorptive molecules have stronger affinity for one another than for the solid (adsorbent). Type VI is a recent addition and is indicative of nonporous solid having an almost completely uniform surface (fig. 1.4) [31, 37, 51, 52]. The presence of a hysteresis loop in IV, which can also be seen in type II, is typical of mesoporous and macroporous materials. If present in type I isotherms, it suggests the presence of mesopores in the adsorbent [31, 37, 44, 51, 52].

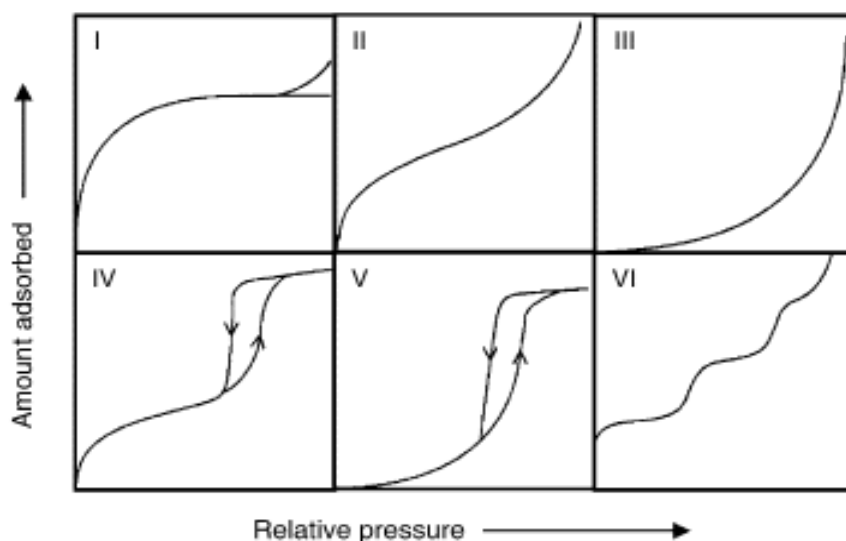


Figure 1.4 IUPAC classifications of adsorption isotherms [31, 37, 51].

1.5.2 PRINCIPLES OR FUNDAMENTALS OF PHYSISORPTION

Typically, gas molecules physisorb to MOF surfaces interacting with the atoms of the framework by attractive dispersive (or van der Waals) and short range repulsive interaction. The adsorption of hydrogen molecules takes place at low temperatures such as 77 K due to the binding energy which is typically less than 10kJ/mol for hydrogen gas with just two electrons [2]. Even though room temperature hydrogen storage technologies are more desirable in vehicles, cryogenic tanks working at 80 K are far easier to manage than vessels with liquid hydrogen at 20 K. The investigation of hydrogen (with kinetic diameter of 2.9Å) adsorption on porous materials for mobile application has become a big challenge. The adsorption of other molecules such as methane and carbon dioxide having kinetic diameters of 3.78 and 3.30 Å, however, occurs at much higher temperatures due to their size, conformation and electronic properties such as quadrupole moment and polarization [1-4, 11, 16, 18, 37, 40]. In physical adsorption, no diffusion barriers are present. The process is also non-activated and has fast kinetics because there are no energy barriers to prevent the molecules of the gas approaching the surface from entering the physisorption well. Fig.1.5 below shows the potential energy curve for the hydrogen molecule as a function of the distance from the adsorbent during chemisorption and physisorption [18, 37].

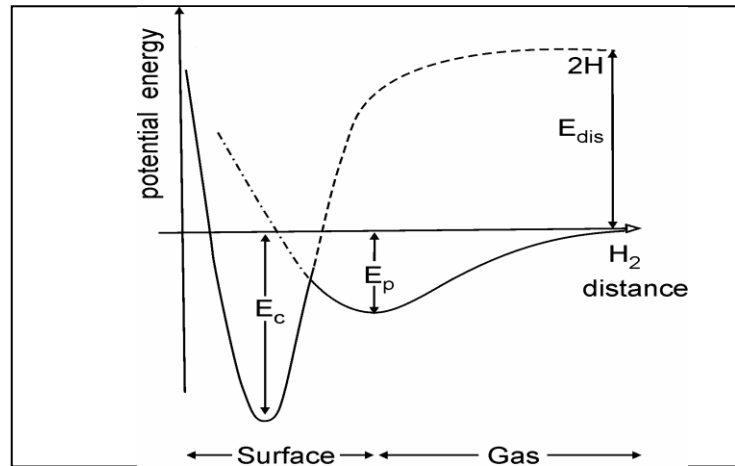


Figure 1.5 Potential energy curve for chemisorbed and physisorbed hydrogen. The minima of the two curves correspond to the equilibrium distance for physisorbed (E_p) and chemisorbed (E_c) hydrogen.

Two values are typically calculated from these measurements to allow the porosity to be compared: surface area and pore volume. Type I isotherms can often be described by the Langmuir model, which assumes that a homogenous monolayer of the adsorbate is formed on the walls of the adsorbent. The Langmuir equation is applied to materials having uniform surface that forms a monolayer with the adsorbate. The collision of the gas molecules with a solid are taken to be inelastic. This is assumed so that the gas molecules remain in contact with the adsorbent for a while before returning to the gas phase. This model yields the equation below, which relates the quantity of gas adsorbed (coverage) V_a , at pressure P [18, 23, 31, 50-52].

$$V_a = \frac{V_m bP}{1 + bP} \quad (4)$$

$$\frac{V_a}{V_m} = \frac{bP}{1 + bP} \quad (5)$$

$$\frac{P}{V_a} = \frac{1}{V_m b} + \frac{P}{V_m} \quad (6)$$

V_m is the volume at monolayer coverage, b is the adsorption coefficient which depends on the heat of adsorption ΔH and temperature T . Both are obtained from the slope when P/V_a is plotted against P to get a straight line graph (note that P is a relative pressure P/P^0)

The specific surface area SSA (s) can then be calculated from a set of limited data points (pressure range) by applying equation 7.

$$s = \frac{V_m \sigma N_A}{m V_o} \quad (7)$$

Where σ is the molecular cross sectional area of the adsorbate (16.2 \AA^2 or $16.2 \times 10^{-20} \text{ m}^2$ for nitrogen). N_A is Avogadro's constant (6.023×10^{23} molecules /mole), m is the mass of the adsorbent in grams and V_o is the molar volume of gas (22414 cm^3). The equation is thus reduced as seen below [18, 23, 31, 50-52].

$$s = \frac{4.35 V_m (\text{cm}^3 \text{ at STP})}{m(\text{g})} \quad (8)$$

An extension to the Langmuir model to describe multilayer adsorption has given rise to the commonly used Brunauer, Emmett, and Teller (BET) equation, which is primarily used to determine the point at which monolayer coverage is obtained. In materials with multiple pores, the narrow pores are filled first and the larger pores are filled at slightly higher pressure. The Langmuir equation, in the estimation of the surface area of MOFs, may not provide accurate results due to the localized adsorption in

microporous MOFs and multilayer adsorption in microporous MOFs (due to pore filling effect at very low relative pressure). BET theory takes into account multilayer adsorption. The BET equation is used universally for the calculation of surface area as a standard method because of its simplicity. It has been shown that BET surface area calculated from the N₂ adsorption isotherm, obtained by the Grand Canonical Monte Carlo (GCMC) simulation, is very similar to the experimental BET surface area. Care must be taken in using the BET equation to determine the surface area of the MOFs since the calculated surface area of the framework depends on the pressure range used in the calculation [18, 23, 31, 50-52].

$$V_a = \frac{V_m C P}{(P_o - P) \left[1 + (C - 1) \frac{P}{P_o} \right]} \quad (9)$$

C is a constant and P_o is the saturation pressure. Other terms have been previously defined. Equation 9 can be written in a linear form:

$$\frac{P}{V_a (P_o - P)} = \frac{1}{V_m C} + \frac{C - 1}{V_m C} \left(\frac{P}{P_o} \right) \quad (10)$$

A plot of $P/[V_a(P_o - P)]$ vs P/P_o will give a straight line with $1/V_m C$ as the intercept and $(C - 1)/V_m C$ as the slope. The values of C and V_m can then be calculated from the slope line. The surface area can thus be estimated too. Moreover the value of the specific surface often depends on the probe molecule used for the adsorption and on its accessibility in the pores of the adsorbent. Typically, adsorption isotherms of N₂, Ar and

CO₂ are used to determine the specific surface area of porous materials. [18, 23, 37, 50, 51]

The gravimetric (*wt %*) and volumetric (*vol*) capacities of the adsorbed gas can be estimated using the following equations.

$$wt\% = \frac{m_{H_2}}{m_{H_2} + m_s} * 100 \quad (11)$$

$$Vol = \frac{m_{H_2}}{V_s} = \frac{m_{H_2}}{m_s} \cdot \rho_s \quad (12)$$

Where m_{H_2} , is the mass of the adsorbed hydrogen, m_s is the mass of the solid adsorbent and ρ_s is the packing density (when the sample is subjected to mechanical compaction). For mobile applications, the packing density is considered in calculating the volumetric uptake. However, the bulk density (obtained more easily from X-ray diffraction analysis or mercury pycnometry) is considered [18, 37, 51].

1.5.3 WHY ISORETICULAR METAL-ORGANIC FRAMEWORK IRMOF-8

Isoreticular metal-organic framework-eight (IRMOF-8) was chosen for this study because of the many reported sorption properties of the porous material itself or of its linker [2, 4, 14, 17, 18, 20, 28, 33, 36, 38, 48, 49, 54-68]. On the account of spillover, in which selected porous solids were mechanically-formed by mixing Pt/C catalyst, consisting of 0.05 g of 20 wt% Pt nanoparticles on activated carbon, with (C₃H₂BO)₆(C₉H₁₂) (COF-1), Cu₃BTC₂ (MOF-199 or HKUST-1), Zn₄O(NDC)₃ (IRMOF-8), Zn₄O(BDC)₃ (IRMOF-1 or MOF-5), Zn₄O(BTB)₂ (MOF-177) and Al(OH)(BDC) (MIL-53(Al)). At 298 K and 100 bar, the hydrogen capacities were found to increase by at

least two-fold relative to the pristine materials. IRMOF-8 with BET and Langmuir SSA of 1466 and 1818 m²/g and pore volume of 0.69 cm³/g) has the highest capacity (~4 wt % at 298 K and 100 bar) till date even higher than IRMOF-1, MOF-177 or MIL-101 with higher surface areas. Its capacity was increased by a factor of 8 and by applying the Clausius-Clapeyron equation, the isosteric heat of adsorption was estimated to be 20-23 kJ/mol [2, 4, 14, 17, 18, 20, 33].

At low temperature of 77 K (-196 °C) and 1 atm, IRMOF-8 having surface areas of 890, 1466, or 1599 m²/g depending on the method of synthesis and activation had hydrogen storage capacities of 1.45, 1.50 and 1.76 wt% respectively. Other MOFs such as MOF-177, IRMOF-1 and IRMOF-18 with surface areas of 4526, 3362 and 1501 m²/g had H₂ capacities of 1.25, 1.32 and 0.89 wt% respectively. This is attributed to the longer linker length of IRMOF-8, forms a rigid conformation or its pore size which accounts for better adsorption at low pressure [20, 24, 28, 33, 36, 54, 55]. Wang et al.[63], studied the effect of metal doping on IRMOF-8. They found that the hydrogen capacity at room temperature increased by 90 %. The surface area and pore volume were conserved in the doping process.

It can be synthesized using a direct mixing or solvothermal method in an acid digestion bomb at temperatures up to 180 °C. The products are porous 3 dimensional (3D) or nonporous materials which have found applications in gas storage as a preconcentrator in the military and in industry, as a component of plastic explosives or chemical sensing of large molecules [36, 54-59, 64]. In CH₄ storage, Siberio-Perez et al. [60] have shown that compared to isorecticular counterparts, IRMOF-8 binds more

strongly than other IRMOFs to the gas due to its smaller pores when the interpenetrated form is synthesized. In a study by Yao et al.[62], the interpenetrated form of IRMOF-8 (SUMOF-3 with two pore sizes of 6.6 and 9.5 Å) had the most adsorption for CO₂ (77 cm³/g or 15.1 wt%) at pressures relevant for CO₂ capture from flu gas (1-1.5 bar). A computational study done by Yang et al.[65, 66], suggested that the suitable pore size for porous material for CO₂ capture is between 1-2 nm. IRMOF-8 with pore size of 1.25/1.71 nm meets this requirement.

1.6 GOALS AND OBJECTIVES OF THIS RESEARCH

The goals of this research were:

- To develop a rapid and facile method to synthesize metal-organic frameworks for gas storage to just a few hours at the same time obtaining high yield.
- To add nitro-functional group(s) to the organic linker of IRMOF-8 and to use this new linker to synthesize a new metal-organic framework for gas storage in an attempt to study the effect of functionalization on the IRMOF-8-NO₂.
- To improve the hydrogen desorption temperature of sodium alanate (NaAlH₄) by nanoconfinement in IRMOF-8 using the wet infiltration method.
- To characterize the metal-organic frameworks using the X-ray diffraction, infrared spectroscopy, nuclear magnetic resonance, thermo-gravimetric analysis, residual gas analysis, particle size analysis, surface area and porosity analysis (BET and Langmuir surface area) and high pressure volumetric analysis.

- To investigate the hydrogen, methane and carbon dioxide storage properties of the metal-organic frameworks.
- To compare the hydrogen, methane and carbon dioxide binding energies on IRMOF-8.

CHAPTER TWO

2 EXPERIMENTAL DETAILS

2.1 MATERIALS AND METHODS

All the samples used in this research were obtained from commercial providers (such as Sigma-Aldrich, TCI America and Fisher Scientific,) and used without further purification. Potassium bromide FT-IR grade (99+ %) was used for the infrared analysis, zinc nitrate hexahydrate, $Zn(NO_3)_2 \cdot 6H_2O$ (≥ 99.0 % pure) was used as the metal source. 2,6- Naphthalenedicarboxylic acid, referred to as 2,6- H_2NDC (99.0 % pure) was the organic linker for the synthesis while anhydrous N,N-dimethylformamide (DMF, 99.8 % pure) was the solvent of choice. Tetrahydrofuran (THF: 98%) was used as the dispersing solvent for sodium alanate ($NaAlH_4$ 99.8 %) for nanocomposite formation in IRMOF-8 and mesoporous carbon. Mesoporous carbon, MC (99.8%) was used as a comparison in nanoconfinement study. N,N-dimethylformamide- d_7 (99.5 atom % D) was used for proton (H) and carbon (C) NMR studies. High purity gases (H_2 , CO_2 and CH_4) were used as adsorbate. All sample handling, weighing and preliminary evacuations were performed in a glove box to prevent contamination from air and moisture. The glove box antechamber was vacuum cleaned several times using argon gas to remove air or moisture and keep its level below 10 ppm.

2.1.1 CONVECTIONAL AND RAPID SOLVOTHERMAL SYNTHESIS OF IRMOF-8 (C-IRMOF-8 AND RS-IRMOF-8)

Synthesis of C-IRMOF-8 was performed following some of the reported procedures [58, 59, 69, 70] with a few modifications. A quantity of 1.19 g (4 mmol) of $\text{Zn}(\text{NO}_3)_2 \cdot 6\text{H}_2\text{O}$ and 0.43 g (2 mmol) of 2,6- H_2NDC were weighed out in an argon-filled glove box and dissolved in 40 mL of DMF in a 125 mL capacity Parr acid digestion bomb. The reaction was carried out at the above temperatures for 20 hours in a Fisher Scientific Isotemp oven 630G. After the Parr bomb was allowed to cool to room temperature, the yellow supernatant was decanted. The crystals were washed with DMF (3 x 5 mL) then filtered and dried under vacuum. The yield was approximately 96 % at the optimum synthesis temperature of 120 °C.

Rapid solvothermal synthesis of IRMOF-8 (RS-IRMOF-8) was carried out using the same amounts of $\text{Zn}(\text{NO}_3)_2 \cdot 6\text{H}_2\text{O}$ (1.19 g) and 2,6- H_2NDC (0.43 g) placed in a 50 mL Pyrex conical flask and dissolved in 40 mL of DMF. The flask was sealed with glass stoppers and placed into a Fisher Scientific ultrasonic cleaner, FS60H, and sonicated at room temperature for 1 hour to obtain a clear solution. The flask was then transferred to a Fisher Scientific isotemp/stirrer with aluminum foil wrapped half way round the flask to reduce exposure to air and to hold a thermometer in place leaving just enough room for the stirrer. The stirrer was set at 350 rpm to prevent hot spot generation in the flask and to allow even distribution of heat. At temperatures of 100, 110, 120, 130, 150 and 155 °C, the solution turned yellow within 25 minutes to 1 hour. Crystal formation was recorded within 30 minutes to 1 hour of heating. Then the reaction was allowed to proceed for 1

hour at 155 °C and 3 hours at other temperatures (except at 80 °C, which lasted for about 24 hours). At the end of the process, the solution was allowed to cool to 40 -50 °C while still stirring. The yellow supernatant was decanted and the crystals washed with DMF (3 x 5 mL) filtered and put under vacuum to dry. A quantitative yield of 98 % was obtained at 155 °C. The yield decreased as temperature decreased to 88 and 75 % (at 130 and 120 °C respectively). The need for the development of a rapid solvothermal method, by combining sonication, stirring and sealing of the vessel used in this research was obtained from literature [71-76].

2.1.2 SYNTHESIS OF IRMOF-8-NO₂

The nitro-IRMOF-8 was prepared by the same procedure reported by Orefuwa et al. [36] based on modifications from Dailly et.al. [59], Li and co-worker [58] at 120 °C. 4,8-dinitro-2,6-naphthalenedicarboxylic acid (4, 8-DN-H₂NDC) was prepared from the reaction of 2,6-H₂NDC and concentrated nitric acid with a few modification with subsequent purification and crystallization [77]. Pure IRMOF-8 was also synthesized at 155 °C. The same amounts of Zn(NO₃)₂.6H₂O (1.19 g) and 4,8-DN-H₂NDC (0.43 g) were weighed out into a 50 mL Pyrex conical flask and dissolved in 40 mL of DMF. The solution was sonicated and then heated. The solution turned yellow within 25 minutes to 1 hour. Crystal formation was recorded within 30 minutes to 1 hour of heating and the reaction was allowed to proceed for 2-3 hours based on the temperature used and to prevent excess loss of solvent to evaporation. Post-synthetic handling was carried out in an argon filled glovebox.

2.1.3 NANOCONFINEMENT OF NaAlH₄ IN IRMOF-8 AND MC

IRMOF-8 was prepared based on the method described in paragraph two of section 2.1.1 at the optimum temperature (155 °C). Exactly 3g of bulk sodium alanate was dissolved in 30 mL of tetrahydrofuran as solvent and filtered through a 0.02 µm whatmann filter paper to exclude bigger particles. Before the infiltration of the sodium alanate solution into the scaffolding material (IRMOF-8), the IRMOF-8 as synthesized and evacuated was degassed at 200 °C for 20 hrs using the ASAP 2020 (surface area and particle analyzer) to exclude the synthesis solvent (DMF). Surface area and porosity of the material was also determined using the ASAP 2020. This was done to determine the pore volume in order to know what volume of sodium alanate solution should be infiltrated. In this case, the pore volume was determined to be 0.66 cm³/g and with a micro pipette, 0.66 mL of the solution was measured and infiltrated into the degassed IRMOF-8 (here known as NaAlH₄@IRMOF-8). Approximately 0.33 mL solution of NaAlH₄ was also infiltrated into MC (here known as NaAlH₄@MC) based on its pore volume. The composite was evacuated at room temperature in the vacuum box overnight to dryness. To obtain the loading capacity, the evacuated composites were degassed at 110 °C for 3 hrs. to obtain the new surface areas and pore volumes.

2.2 SAMPLE HANDLING, CHARACTERIZATION AND MEASUREMENTS

2.2.1 THE GLOVE BOX

All sample measurements/weighing, solution filtration, infiltration (composite formation) and post-synthetic handling were done in the Vacuum Atmosphere glove box (VAC, Model HE-493) fitted with a dynamic vacuum pump. The sample chamber was vacuum

cleaned about five times to remove air and moisture trapped in it during the transfer of the vessels, sample holders and other materials.



Figure 2.1 Glove box

2.2.2 X-RAY DIFFRACTION (XRD) ANALYSIS

The X-ray diffraction analysis of the samples was done to confirm their crystal purity or the formation of a new phase(s) upon reaction or the infiltration of sodium alanate into the scaffold. The instrument used was an X'pert Pro PANalytical X-ray Diffractometer (model PW3040 Pro) which used copper radiation at a step size of 0.0167° in 2θ . The peak signals were collected on an X'Celerator RTMS detector. The voltage and current applied were 40 kV and 20 mA respectively. All sample loadings were done in the glove box. Each sample was transferred into the sample holder and a razor was used to level the sample in order to ensure an even surface. A thin transparent Kapton polymer film was used to cover the sample to prevent exposure to air and moisture when it was out of the

glove box and the lid was fastened to hold the thin film tightly onto the x-ray sample holder.

The sample holder was then removed from the glove box and transferred to the PANalytical X'pert Pro X-ray Diffractometer. The program for running the x-ray diffraction analysis was started by clicking X'pert data collector on the desktop which prompted the instrument's connection. The total run time for each analysis was 15 minutes based on the settings. The post-analysis was performed by using the X'pert data viewer software on the desktop which helped in determining whether new compounds were formed from mixing the different reactants or compounds. Also the crystal structure and cell volumes of the samples under investigation could be determined. A picture of the PANalytical X'pert Pro X-ray Diffractometer is shown in Fig 2.2 below.



Figure 2.2 X'pert Pro PANalytical X-ray Diffractometer

2.2.3 THERMOGRAVIMETRIC ANALYSIS (TGA)

The thermal stability of the samples was determined using a Perkin-Elmer Diamond TG/DTA Thermogravimetric Analyzer TGA (Model: Pyris Diamond High Temp 115) equipped with an air cooling control unit. Samples were scanned at a rate of 5 °C/minute and temperatures up to 600 °C under argon gas flow to prevent sample contamination by air and moisture. The TGA instrument was turned on by switching the power button on and allowing the instrument to initialize for some minutes until linkwait was displayed on the LCD monitor. The program software was launched and the sample and program information were entered. The sample stage was opened by pushing the open button on the side of the TGA machine. Two identical high temperature ceramic pans located on two beams covered by the stage served the purpose of the reference pan and the sample pan. Pushing the close button on the side of the TGA will close the sample stage. The weight of the two pans was zeroed. This was repeated three times to ensure equilibration of the weight of the pans. The sample stage was then opened by pushing the open button and the sample pan was carefully removed with forceps. A small amount (not less than 5 mg) of the sample to be analyzed was put into the pan and carefully placed on the beam. The stage was closed and the weight of the sample was measured by clicking on the weigh icon on the program file displayed on the computer monitor. This was repeated three times to ensure equilibration. The program was then started by clicking the start button on the program. The results from the TGA/DTA analysis are valuable in setting up a program for degassing the sample before the surface area and porosity analysis. The picture of the TGA instrument is shown in Fig 2.3 below.

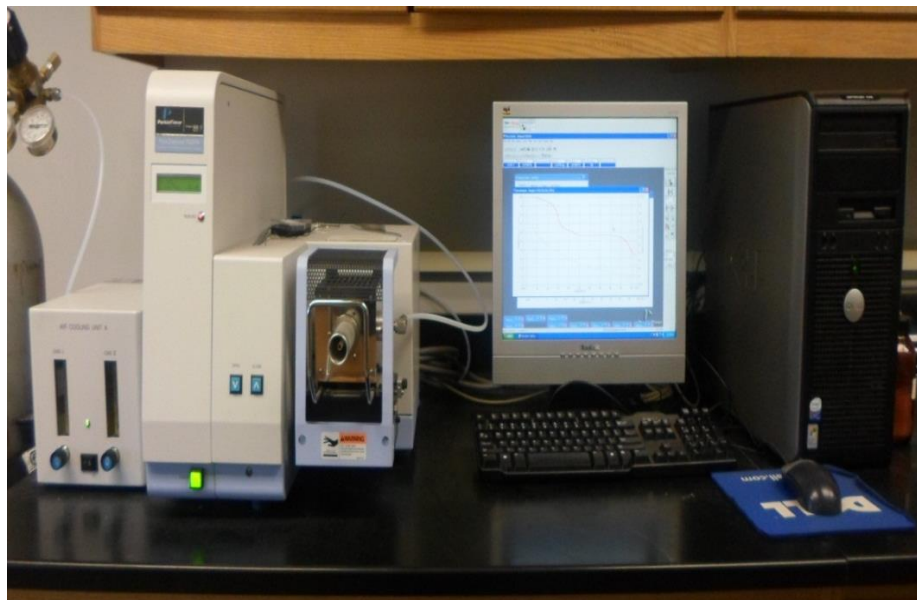


Figure 2.3 Thermogravimetric Analyzer

2.2.4 INFRA RED SPECTROSCOPY ANALYSIS

Solid-state infrared spectroscopy was carried out according to the method described by Mamatha et al [78]. The FTIR analysis reveals the functional groups present in the synthesized molecule and also the functional group(s) responsible for bond formation. Samples were pelletized in KBr (ratio 1: 10) and the solid state infrared spectra were recorded in the range of $400 - 4000 \text{ cm}^{-1}$ at ambient conditions using a IR Prestige-21 Fourier Transform Infrared Spectrophotometer (8400S from the Shimadzu Corporation). In an air tight container, the sample was taken out of the glove box and further pressed into a very thin pellet using the hydraulic press. The IR instrument was turned on and the IR solution icon on the computer was clicked. The measure button on the displayed page was clicked; the data and comment of the sample to measure were entered. Initialization was done by clicking on the measurement button this time after the

appearance of the green lights. When initialization was completed, a background scan was taken, a total of 16 scans at a resolution of 2. The sample was then placed in the sample holder and transferred into the sample compartment for data recording. This was done for the pure IRMOF-8, IRMOF-8-NO₂ as well as the reactants. The picture of the FTIR instrument used in this research is shown in Figure 2.4 below.

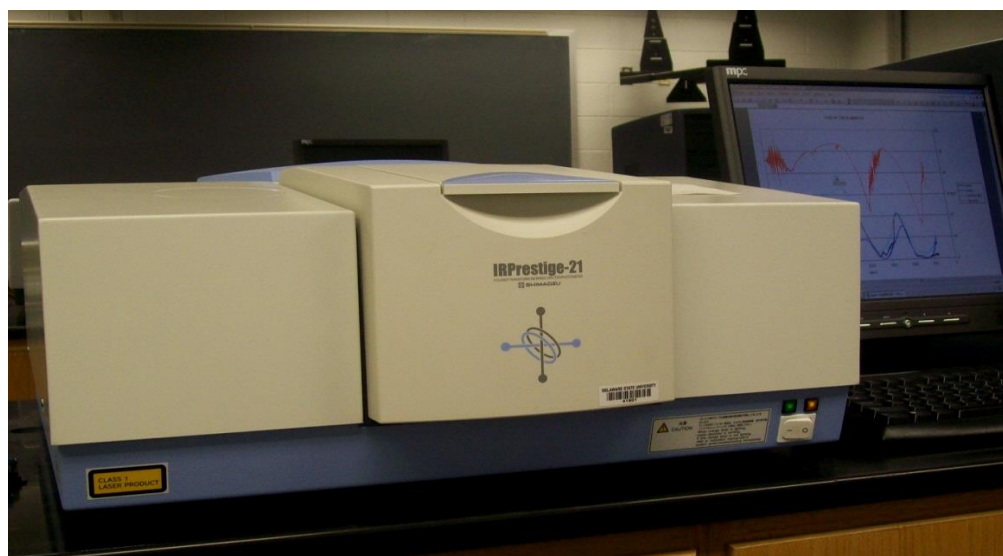


Figure 2.4 IRPrestige-21 Spectrometer

2.2.5 NUCLEAR MAGNETIC RESONANCE (NMR)

The ¹H and ¹³C resonance signals of the organic linkers were recorded using a JEOL ECX 400/100 MHz Delta 2-NMR spectrophotometer. A frequency range up to 15 ppm was used at 25 °C with deuterated DMF-d₇ as the solvent. The NMR spectrum of the functionalized linker was predicted and confirmed using ChemDraw[®] Ultra 8.0 software [79]. Before using the instrument, the air control unit was turned on and then the DELTA icon on the computer was clicked to establish a communication with the NMR instrument. The standard sample holder in the NMR was ejected and the sample was

loaded onto the equipment. The magnetic spin was turned on at 9 Hz using the software. The solvent used in dissolving the analyte was locked and a gradient shim was done either manually adjusting from the software or automatic. Once the shim bar turned green and at their maximum values, the sample information was entered in the new dialogue box and the analysis was run choosing the appropriate file for proton or carbon run.



Figure 2.5 Oxford JEOL ECX 400 MHz Delta 2-NMR Spectrophotometer

2.2.6 LASER DIFFRACTION PARTICLE SIZE ANALYZER (LDPSA)

The particle size distribution of the IRMOF-8 and IRMOF-8-NO₂ was recorded using a laser diffraction particle size analyzer (Model: SALD-2201) from Shimadzu. The instrument was turned on first before clicking the WIND-SALD icon on the PC for the instrument to communicate with the software. Once communication was established, the initialization was carried out to check for the adjustment of the rays. Approximately 60 mg of the sample was weighed and dispersed in 20 mL of water in a beaker. With a Pasteur pipette, distilled water was put into the glass sample holder and transferred to the

sample compartment of the instrument. The instrument sonicator was set to the desired speed. A blank measurement was carried out which would be subtracted from the sample analysis. To run the sample, a portion of the blank was taken off and with a clean pipette, a portion of the dispersed sample suspension was introduced into the sample holder and using the same sonicator speed (to keep the particles in constant motion and in the direction of the light rays) the particle size was determined.

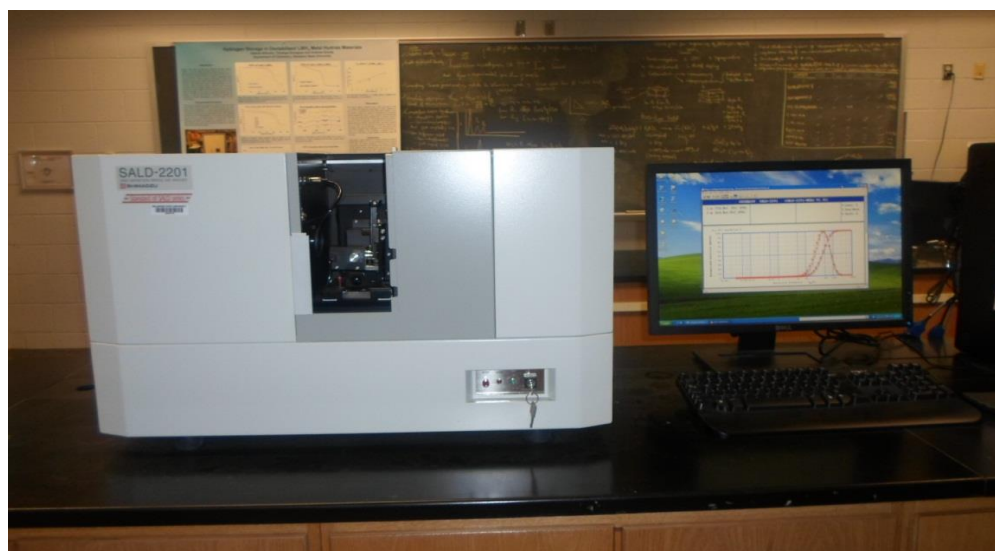


Figure 2.6 Laser Diffraction Particle Size Analyzer

2.2.7 SURFACE AREA AND POROSITY ANALYZER

The surface area, pore volume and pore size of the synthesized samples were obtained using on a Micromeritics ASAP 2020 surface area and porosity analyzer (Norcross, GA). The equipment was fitted with two independent vacuum systems which allowed simultaneous preparation (degassing) of two samples and analysis of another. The two-station degassing systems were fully automated with precise controlled heating profiles. Before degassing or analysis of the sample, the computer was first turned on

before turning the instrument on to allow for communication. The cold trap was filled with liquid nitrogen to allow good pressure pull down by the vacuum pumps during degassing or sample analysis. The standard ASAP 2020 comes equipped with six analysis gas inlets and a 1000-mmHg transducer

Approximately 200-300 mg of IRMOF-8, IRMOF-8-NO₂ or NaAlH₄@IRMOF-8 was measured in the glove box into the standard ASAP 2020 sample tube (1/2- inch stem). A filler rod was put into the sample holder to reduce gas usage during measurement and a seal frit was used to cover the holder. The sample was weighed and evacuated under vacuum based on the thermal stability of the sample from the TGA analysis until the outgas rate was <10 μ mHg. The IRMOF-8 samples were degassed under vacuum at room temperature for 1 hour and at 200 °C for 20 hours. The IRMOF-8-NO₂ samples were degassed under the same conditions for 10 hours and the nanoconfined NaAlH₄@IRMOF-8 and NaAlH₄@MC was degassed at 110 °C for 3 hours. The sample tube was reweighed to obtain a consistent mass for the degassed sample. After degassing and cooling, the sample tube was slipped into the isothermal jacket and the tube was transferred to the analysis port.

N₂ adsorption/desorption isotherms were measured volumetrically at 77 K. Multipoint BET and Langmuir measurements were taken at relative pressures in the linear range of $P/P_0 = 0.01-0.05$ for BET plots and $0.05-0.3$ for Langmuir plots. The pore volume was calculated from N₂ adsorption measurements at -196 °C and $P/P_0 = 0.50$. Nitrogen is commonly used because it is readily available in high purity, the most appropriate coolant (liquid nitrogen) is also readily available and cheap. Thirdly, the

interactions of nitrogen with most solid surfaces are relatively strong and there is a wide acceptance of its cross-sectional area. Hydrogen, carbon dioxide and methane (99.999% pure H₂, CO₂ and CH₄) adsorption/desorption isotherms were also measured by the Micromeritics ASAP 2020 running on version 3.0 of the software package. Free space was measured using helium (99.9999% purity). The gases were purchased from Keen gas and Matheson Gas Companies and used as received. All isotherms were measured using samples that were activated *ex situ*: that is, other than the initial evacuation of the sample in the sample cell for sorption measurements to commence. No other treatment of the sample was performed. This was done to ensure that the nature of the material used in the surface area measurements was the same as that being used in the gas sorption experiments. Figure 2.7 below is the picture of ASAP 2020 surface area and porosity analyzer.

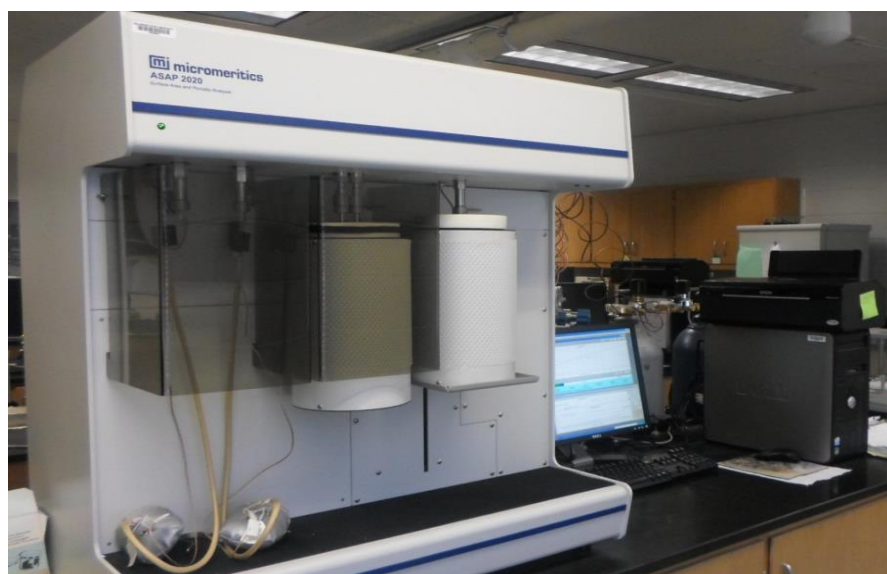


Figure 2.7 ASAP 2020 surface area and porosity analyzer

2.2.8 HIGH PRESSURE VOLUMETRIC ANALYZER (HPVA)

Equilibrium gas adsorption/desorption isotherms were measured using the static volumetric method in an HPA-100 (High Pressure Analyzer VTI) from the Micromeritics Corporation (Norcross, GA, USA). The system was equipped with two electronic Bourdon gauge-type transducers (Mensor) that covered the range 0 - 1500 psi (accuracy 0.010% full scale). One was used to measure the pressure in the dosing manifold, while the other monitored the pressure in the sample cell. The working temperature of the manifold was kept at 40 °C by heating the manifold compartment. Vacuum was provided by a TSH 071 E turbomolecular pumping station (Pfeiffer) capable of reaching pressures of $< 1 \times 10^{-6}$ mbar. The sample cell was a 2- piece assembly that consisted of a sample chamber (~ 2 mL) and a high pressure bellows valve. The two were connected via ¼” VCR fittings and the materials of construction were all stainless steel. Connection to the system was achieved by a ¼” VCO fitting. Two ports were available: one for outgassing the sample and an analysis port, outfitted to hold either a recirculating bath or a small cryogenic dewar. Ultra-high purity He (99.999%), H₂ (99.999%), CH₄ (99.999%) and CO₂ (99.999%) were purchased from Keen and Matheson gas and used as received. In a typical experiment ~500 mg of sample was activated (at same temperatures used in the ASAP 2020) then transferred to the analysis port and evacuated at room temperature to 10^{-6} mbar prior to sorption experiments. After degassing, an isothermal jacket was worn around the sample holder, attached to the analysis port and the free space of the sample was first measured at room temperature. The value was then subtracted from the volume

of the empty tube. The volume (V_{sp}) obtained and the mass (m_{sp}) of the sample after analysis was used to determine the skeletal density (ρ_{sk} in g/cm^3) [18]

$$\rho_{sk} = \frac{m_{sp}}{V_{sp}} \quad (13)$$

The equation above can also be used to obtain the bulk or packing density of the metal-organic framework

$$V_{pore} = \frac{1}{\rho_{bulk}} - \frac{1}{\rho_{sk}} \quad (14)$$

Where V_{pore} is the pore volume in cm^3/g , ρ_{bulk} is the crystallographic density of the sample. In real time analysis, at temperatures other than ambient, the free space of the sample was measured first before logging in the information for the particular gas. At room temperature the sample free space and real time analysis were run at the same time.



Figure 2.8 High Pressure Volumetric Analyzer (HPVA-100)

2.2.9 PRESSURE COMPOSITION ISOTHERM (PCI) INSTRUMENT FOR TEMPERATURE PROGRAMMED DESORPTION (TPD)

The Advanced Materials Corporation hydriding apparatus was used to run TPD's on the sample (NaAlH_4 and $\text{NaAlH}_4@$ IRMOF-8) to determine their reversibility. The TPD plots obtained were also used to further confirm the desorption curves obtained from the TGA. The samples were heated at a rate of $4\text{ }^\circ\text{C}/\text{min}$ from room temperature to $475\text{ }^\circ\text{C}$. The desorption curves of each sample was recorded and converted to an excel file.

Pressure Composition Isotherm analysis was carried out using the Advanced Materials Corporation hydriding apparatus. The sample chamber was detached from the instrument, cleaned and transferred to the glove box where the sample was loaded into it. Approximately 0.4 g of the samples was placed inside the sample holder. The chamber was attached to the hydriding apparatus via a quick connect fitting. Labview software installed on the computer that was interfaced to the apparatus was used to control the system as well as to collect and analyze the data. The pressure composition isotherms for the samples, both absorption and desorption were obtained.

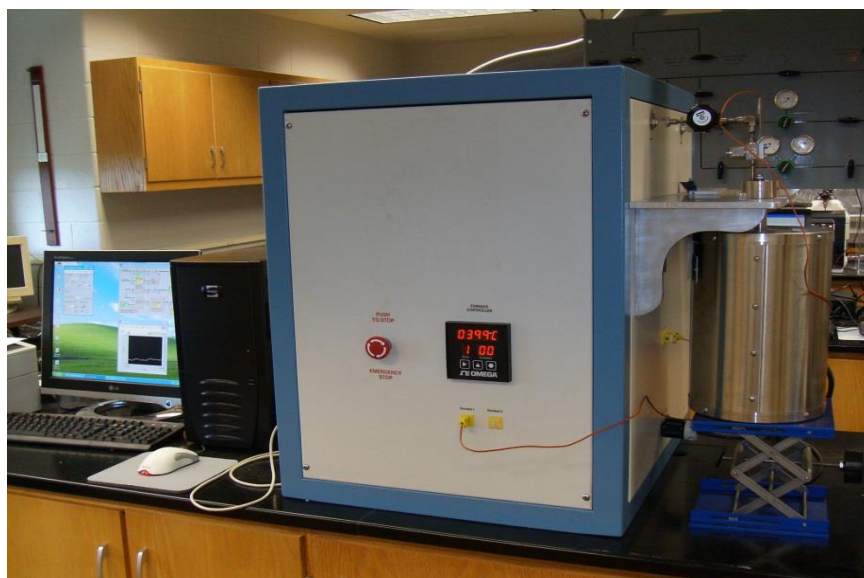


Figure 2.9 Advanced Automated Hydriding Apparatus

2.2.10 RESIDUAL GAS ANALYZER (RGA)

A Standard Research Systems Residual Gas Analyzer (SRS RGA) model RGA Pro-2500 fitted with a quadrupole mass filter, faraday cup detector and a thoria-iridium filament was used to quickly identify the gas species present in the desorbed gases and monitor the level of N_2 , CH_4 , CO_2 , CO , NO_2 and H_2 in the desorbed gases of heated samples. The instrument calibration was confirmed from ultrahigh purity H_2 as 99.9% and air analysis was 78% N_2 , 20% O_2 and 0.3% CO_2 before use. The RGA was coupled to the Advanced Materials Corporation PCI unit. The sample holder was filled with about 0.4 g of the sample to be analyzed in argon-filled glove box. The sample holder compartment was clamped on to the PCI unit and connected to the RGA via a 1/8" sampling line. With the sample holder valve closed, a leak test was carried out and the sample and system were purged. The air pressure which controlled valve opening was set at 40 psi. The RGA was turned on. The roughing pump was turned on followed by the

RGA switch. The turbo pump was turned on and monitored until the pressure in the chamber/frequency was around 10^{-4} mbar/1500 Hz. It should be noted that The RGA must only be operated if the pressure in the chamber is not greater than 10^{-4} Torr. The manifold was cleared of residual gases before use. The pressure versus time (P v T) mode was selected. The background measurement was done at room temperature. Sample measurements were carried out with the temperature ramped to about 470 °C. After few seconds, the display of the selected species being monitored appeared on the screen with different pressure readings as the temperature rose.



Figure 2.10 Residual Gas Analyzer coupled to Advanced Materials PCI unit

CHAPTER THREE

3 RAPID SOLVOTHERMAL SYNTHESIS OF IRMOF-8

Existing methods for the preparation of MOFs are generally very time-consuming or they yield low surface area materials. One spot solvothermal reaction conditions have been reported for growing high purity crystals large enough for single crystal diffraction . However, the conditions have the drawback of long reaction times, involvement of large amount of solvent or too high temperature resulting in nonporous material [32, 34, 54, 69, 90]. Another solvothermal method that has been introduced to cut down on the long reaction times is microwave assisted solvothermal method. However, it suffers the disadvantage of formation of crystals that are not large enough for obtaining good structural data [12, 72]. The slow diffusion method at room temperature also yields crystals large enough for crystallographic studies (which often approach 100 % of the sample) but this method lasts for days or weeks and requires mixtures of solvent. Room temperature synthesis can take a few hours with rapid stirring and mixtures of two or more solvents or several days or a month in one spot. The yields however are low and often times have low surface area [34, 36, 38, 39, 56, 58, 71]. DMF was chosen as the solvent of choice over DEF because of the smaller solubility of larger links and lower cost [48]. Bae et al. [71] and Khan et al. [72] have reported that for practical applications, and laboratory testing, a more rapid and inexpensive solvothermal production of larger

quantities may be desired because many MOFs, with good thermal stability, require hydro/solvothermal synthesis conditions.

It is in light of this, that the advantages of sonication, rapid stirring and sealing of the containing vessel [72-76], were all combined to come up with a new rapid solvothermal method that is relatively inexpensive and uses less solvent for synthesis and activation compared to the convectional solvothermal methods.

3.1 X-RAY ANALYSIS OF C-IRMOF-8 AND RS-IRMOF-8

Figures 3.1 and 3.2 show the XRD patterns of C-IRMOF-8 and RS-IRMOF-8, respectively. Figs. 3.1(a-b), 3.2(a) and (b) depict the starting materials. The powder XRD patterns of the C-IRMOF-8 (Fig. 3.1(d)–(f)) synthesized using the convective solvothermal method at different temperatures revealed the formation of the product at temperatures between 100 °C and 150 °C. When compared with the literature [59, 62, 63, 69, 80], the patterns in Figs. 3.1(d) and (f), 3.2(d) and (f) were in good agreement with published data. Table 3.1 shows the peaks (2θ peak values and the corresponding d-spacing in Å) for the RS-IRMOF-8 prepared at 155 °C. Table 3.1 also shows six peaks including the typical peaks of 6.30° and 8.44° as reported by Yaghi et al. [47, 62, 80]. A typical peak of 6.30 degrees was also reported in Ref. [63], however other peak values were not stated. The variations seen in the XRD pattern at synthesis temperature of 150 °C (Fig. 3.1(f)) may be attributed to the high temperature and pressure build-up in the reaction vessel. Another possible explanation is that, since the sample product turned brown after synthesis, perhaps decomposition of the product occurred. Solvothermal syntheses are normally done in the temperature range of 85–125 °C and exceeding this

temperature in a closed vessel can possibly result in a nonporous material [54, 81]. At 80 °C the peaks in Fig. 3.1(c), indicate that an intermediate phase different from that in Fig. 3.1(d)–(f) may be formed. Fig. 3.2(c)–(f) show the XRD patterns of RS-IRMOF-8 synthesized using the rapid solvothermal method. The patterns for RS-IRMOF-8 synthesized at 100 °C in Fig. 3.2(c) and 110 °C (not shown) were similar to each other but somewhat different than those in Fig 3.2(d)–(f) which do not contain the peaks from the starting materials in Fig. 3.2(a) and (b). The patterns in Fig. 3.2 show a comparison between C-IRMOF-8, taking Fig. 3.2(g) as a good representative, and RS-IRMOF-8. Fig. 3.2(d)–(f) show similar patterns to that in Fig. 3.2(g). This indicates that the phases formed in the C-IRMOF-8 and RS-IRMOF-8 samples are the same.

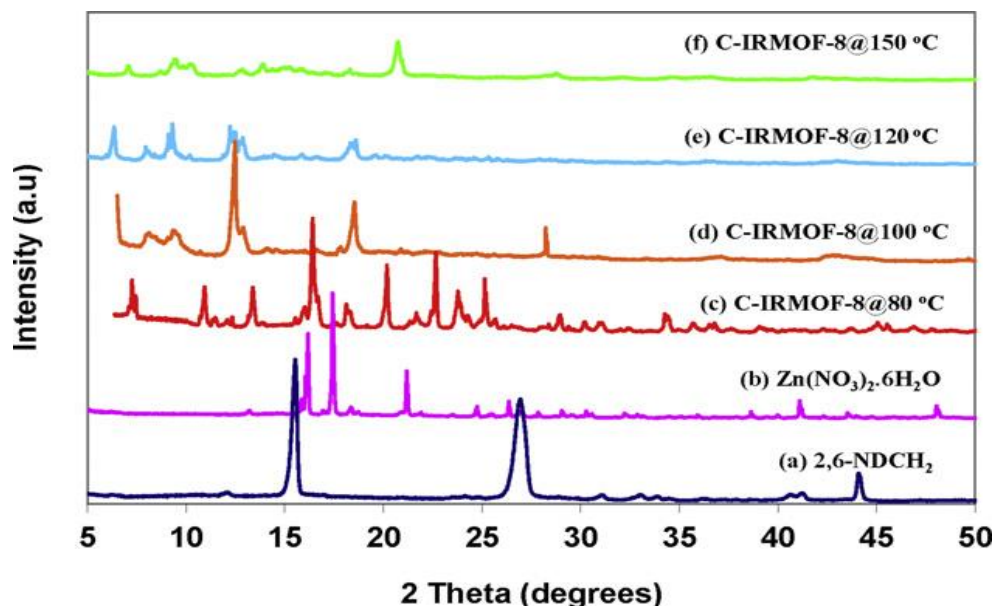


Figure 3.1 XRD patterns of reactants (a) 2,6-H₂NDC, (b) Zn(NO₃)₂·6H₂O and products (C-IRMOF-8) prepared by a convectional one-spot solvothermal method at (c) 80 °C, (d) 100 °C, (e) 120 °C, (f) 150 °C.

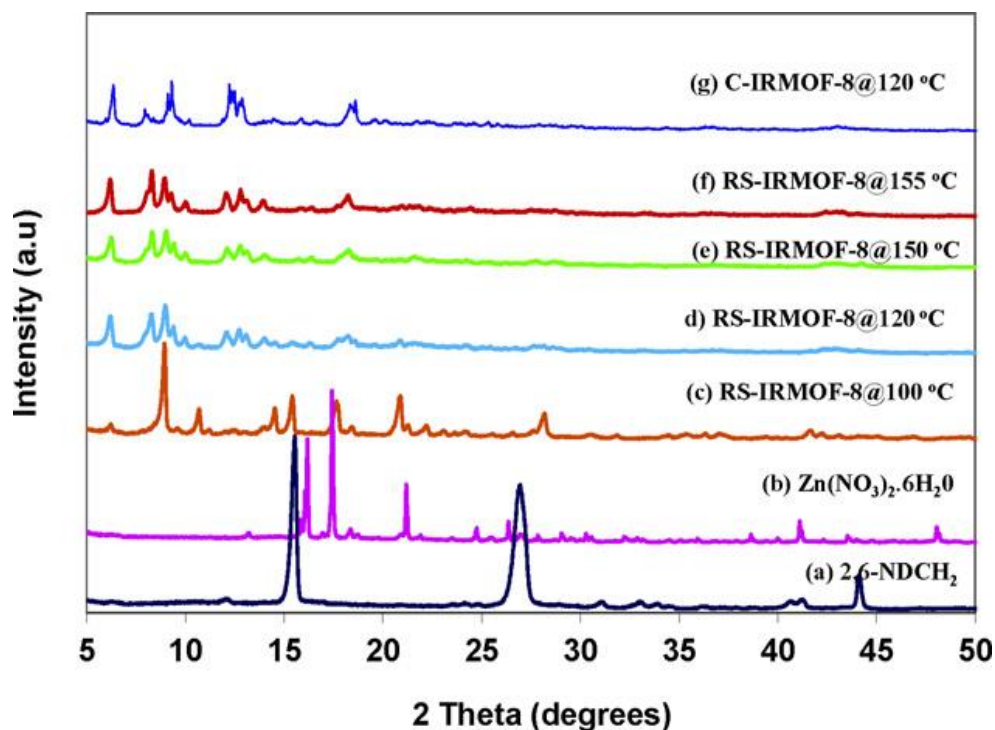


Figure 3.2 XRD patterns of reactants (a) 2,6- H₂NDC, (b) Zn(NO₃)₂.6H₂O and products (RS-IRMOF-8) prepared by rapid solvothermal method at (c) 100 °C, (d) 120 °C, (e) 150 °C, (f) 155 °C compared to (g) C-IRMOF-8 at 120 °C.

TABLE 3.1 XRD reflections and d-spacings of RS-IRMOF-8 and reference IRMOF-8

Sample	Peak values in 2θ(degree)	Corresponding d-spacing [Å]	Reference:
RS-IRMOF-8@155 °C	6.22 , 8.31 , 8.97 , 10.06, 12.05, 12.79, 13.95, 16.25, 18.24	14.21, 10.64, 9.84, 8.78, 7.33, 6.92, 6.34, 5.39, 4.85	This work ,, ,,
IRMOF-8	6.30, 8.44, 11.91, 13.28, 16.73, 17.90	14.82, 10.46, 7.42, 6.68, 5.39, 4.96	59, 69, 80
IRMOF-8	6.30, other peaks not listed	Not given	63

3.2 INFRARED SPECTROSCOPY OF C-IRMOF-8 AND RS-IRMOF-8

Solid- state infrared spectroscopy was carried out at ambient conditions. Fig. 3.3(a) and (b) contains the bands for the organic linker and metal cluster precursor, respectively. The green dot in Fig. 3.3(a) near 1700 cm^{-1} shows the IR band of the carbonyl functional group of the ligands. The IR bands of the C-IRMOF-8 synthesized at $120\text{ }^{\circ}\text{C}$ in a Parr acid digestion bomb, seen in Fig. 3.3(h), are identical to the bands in Fig. 3.3(e)–(g), which is RS-IRMOF-8 synthesized at $130, 150$ and $155\text{ }^{\circ}\text{C}$. The product obtained at $120\text{ }^{\circ}\text{C}$ using the rapid method is also identical but not shown in the figure. The rapid solvothermal RS-IRMOF-8 synthesized at 100 and $110\text{ }^{\circ}\text{C}$ (Fig. 3.3(c)–(d)) shows the presence of an additional band at 920 cm^{-1} not seen in Fig. 3.3 (e)–(h) indicating a different phase. Another band at 1490 cm^{-1} appears in all the spectra but its intensity diminishes at higher temperatures. The absence of carbonyl (C=O) stretching vibration IR bands between 1650 and 1730 cm^{-1} in Fig. 3.3(c)–(h) shows that the H_2NDC is fully coordinated. The IR bands in Fig. 3.3(e)–(h) recorded at 1660 cm^{-1} , 1617 cm^{-1} , 1589 cm^{-1} , 1410 cm^{-1} , 1360 cm^{-1} , 1200 cm^{-1} , 1106 cm^{-1} , 788 cm^{-1} are in agreement with the literature [47, 54, 58].

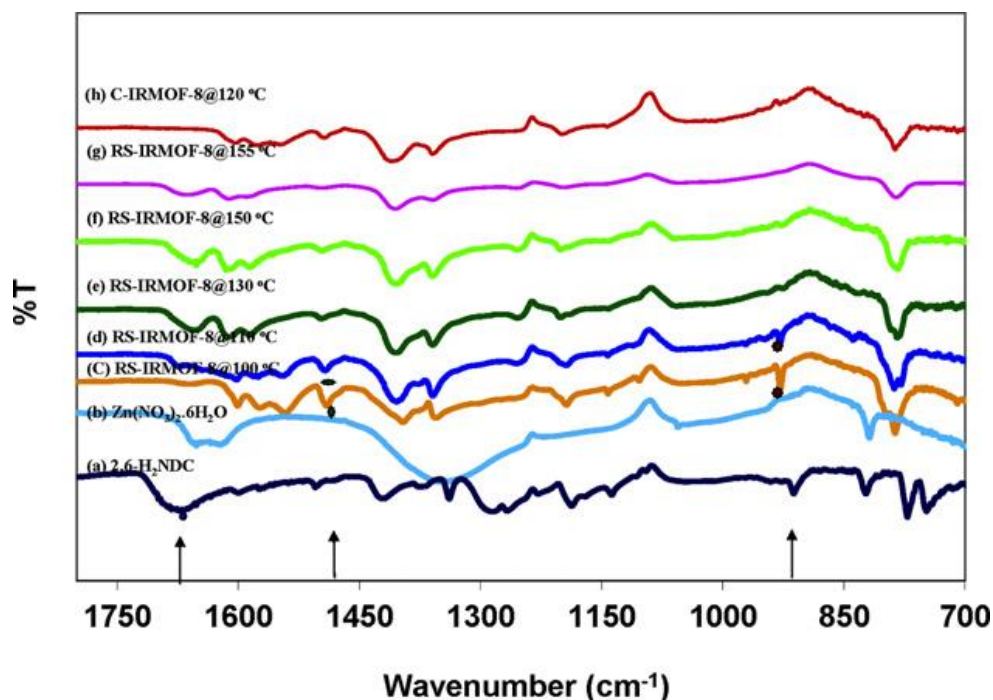


Figure 3.3 FTIR spectra of reactants (a) 2,6-H₂NDC (b) Zn(NO₃)₂·6H₂O and products (RSIRMOF- 8) at (c) 100 °C, (d) 110 °C, (e) 130 °C, (f) 150 °C, (g) 155 °C compared to a convectional one-spot solvothermal method (h) C-IRMOF-8 at 120 °C.

3.3 THERMOGRAVIMETRIC ANALYSIS OF C-IRMOF-8 AND RS-IRMOF-8

Thermogravimetric analysis was done to compare the thermal stabilities of the C-IRMOF-8 and RS-IRMOF-8. Fig. 3.4 shows the TGA curves comparing the thermal stabilities of the C-IRMOF-8 and RS-IRMOF- 8. The RS-IRMOF-8 samples prepared at 120, 130, 150 and 155 °C, as seen in Fig. 3.4(b)–(e), all have similar weight losses. Initially there is a gradual weight loss which increases to about 30% between 100 °C and 200 °C. This is in the range of the boiling point of water (100 °C) and DMF (153–155 °C). This loss is higher than the weight loss seen for C-IRMOF-8 (an initial 20% weight loss) in Fig. 3.4(a). One possible explanation for this is that the RS-IRMOF-8 may have a smaller mean particle diameter than the C-IRMOF-8. The smaller particle sizes in the

case of RS-MOF-8 would result in a greater percentage of the pores being near the surface thereby more accessible to the synthesis solvent and thus resulting in a greater solvent uptake. In the case of C-IRMOF-8, a greater percentage of the pores may be occupying positions that are deep within the particle and thus, they are blocked from the synthesis solvent. This blockage creates pores that are empty or void thus resulting in less solvent uptake. The products, regardless of their synthetic route, were stable up to 400 °C until a sharp drop occurred which could be attributed to the linker decomposition to finally give zinc oxide (ZnO).

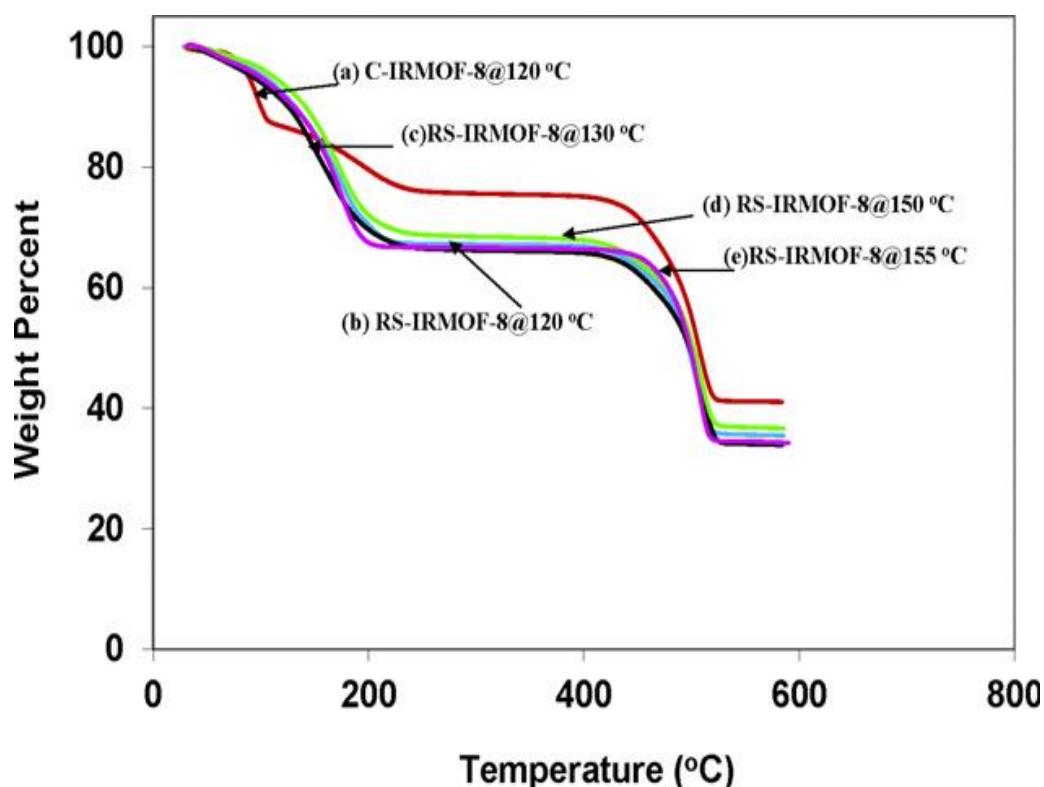


Figure 3.4 TGA curves of the as-synthesized IRMOF-8 using the rapid conventional solvothermal method (RS-IRMOF-8) at different temperatures (b) 120 °C, (c) 130 °C, (d) 150 °C, (e) 155 °C compared to (a) C-IRMOF-8 prepared by a conventional one spot solvothermal method at 120 °C.

3.4 LASER DIFFRACTION PARTICLE SIZE ANALYSIS OF C-IRMOF-8 AND RS-IRMOF-8

In order to better understand the trend in the TGA curve or to confirm that RS-IRMOF-8 has smaller particle sizes than C-IRMOF-8, the particle size distributions were measured using a laser diffraction particle size analyzer (SALD-2201). The C-IRMOF-8 and RS-IRMOF-8 samples had particle diameters in the range of 128–177 μm (average of $143.50 \pm 0.04 \mu\text{m}$) and 9.49–114 μm (average of $33.50 \pm 0.40 \mu\text{m}$), respectively. The slight variation in particle distribution in the RS-IRMOF-8 at 130 and 150 $^{\circ}\text{C}$, can be attributed to the variation in temperature or pressure difference during synthesis which are conditions necessary (or factors that affect MOFs) for solvothermal synthesis of MOFs. The particle size difference however explains the initial weight loss in the TGA curves above.

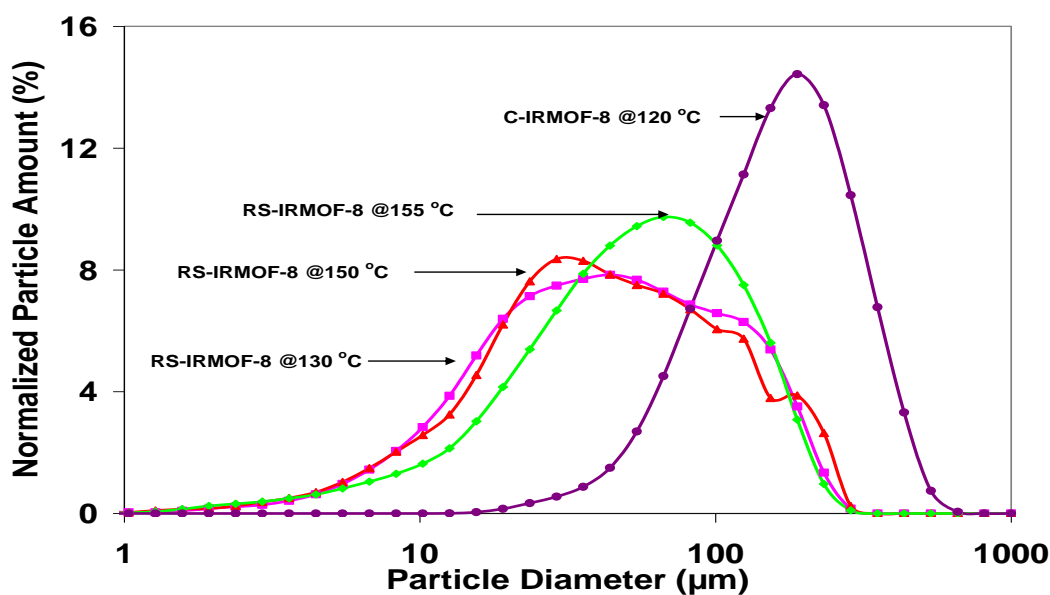


Figure 3.5 Laser diffraction particle size distributions of RS-IRMOF-8 and C-IRMOF-8

3.5. SPECIFIC SURFACE AREA AND POROSITY OF C-IRMOF-8 AND RS-IRMOF-8

The porosity of the as-synthesized materials, C-IRMOF-8 and RSIRMOF-8 was determined volumetrically from the N₂ adsorption–desorption isotherms at -196 °C in the range of $1.00 \times 10^{-3} \leq P/P_0 \leq 1.00$. The samples were initially degassed at room temperature for 1 h, and then the temperature was increased at a rate of 5 °C/min to 200 °C and held there for 20 h. Several Type-I isotherms shown in Fig. 3.6(a)–(d) were determined for C-IRMOF-8 in the range 100–130 °C. The specific surface areas of these samples based on the BET and the Langmuir equations were calculated, with the sample prepared at 120 °C (Fig. 3.6(a)) having the highest surface area of 1477 m²/g (BET) and 1694 m²/g (Langmuir). The total pore volume was 0.6030 cm³/g at relative pressure of $P/P_0 = 0.50$. The steep rise usually seen at the end of the isotherm was barely noticeable. The pore size was found to be 1.62 nm, which falls into the category of micropores. This is consistent with the shape of the sample's isotherm. Table 3.2 gives a summary report of the other C-IRMOF-8 samples prepared at several synthesis temperatures with equal volumes (40 mL) of solvent.

An effort was also made to compare the adsorption behavior of C-IRMOF-8 prepared at 120 °C to that of RS-IRMOF-8 prepared at several temperatures. Fig. 3.7(b) contains the isotherm for the C-IRMOF-8 sample prepared at 120 °C and Fig. 3.7(a), and (c)–(e) contain those for the RS-IRMOF-8 sample prepared at 120, 130, 150 and 155 °C. Since the highest surface area of 1801 m²/g STP (Langmuir) and 1599 m²/g STP (BET) occurred at 155 °C, it appears that this is the optimum synthesis temperature for this

sample. The pore volume at this temperature is $0.693 \text{ cm}^3/\text{g}$ at $P/P_0 = 0.50$ and the pore size is 1.59 nm . Table 3.3 gives a summary of the data collected at the various temperatures for RS-IRMOF-8. Fig. 3.7(a) and (c)–(e) all show a Type-I reversible isotherms with permanent porosity. This finding is based on reports that the presence of little or no hysteresis in N_2 adsorption isotherms is an indication of permanent porosity [8, 38, 39, 82-85]. The pore sizes of the samples in Tables 3.2 and 3.3 are virtually identical further confirming the efficiency and effectiveness of this rapid route for the synthesis of MOFs. The data in Tables 3.2 and 3.3 also show that the pore volume is at a maximum at the optimum synthesis temperatures of $120 \text{ }^\circ\text{C}$ for C-IRMOF-8 and $155 \text{ }^\circ\text{C}$ for RS-IRMOF-8. Fig. 3.8 contains a chart showing the correlation between synthesis temperature and specific surface area (SSA). Using the convective oven synthesis in a Parr acid digestion bomb, the SSA of C-IRMOF-8 increased to a maximum at $120 \text{ }^\circ\text{C}$ and then decreased as seen Fig. 3.8(A) and (B). However with the rapid solvothermal synthesized material; RS-IRMOF-8 (Fig. 3.8(C) and (D)), the optimum synthesis temperature was observed at $155 \text{ }^\circ\text{C}$. With this method, IRMOF-8 was not formed at 100 and $110 \text{ }^\circ\text{C}$ and is therefore not shown. The precision of the data in Fig. 3.8 is very good as indicated by the small error bars.

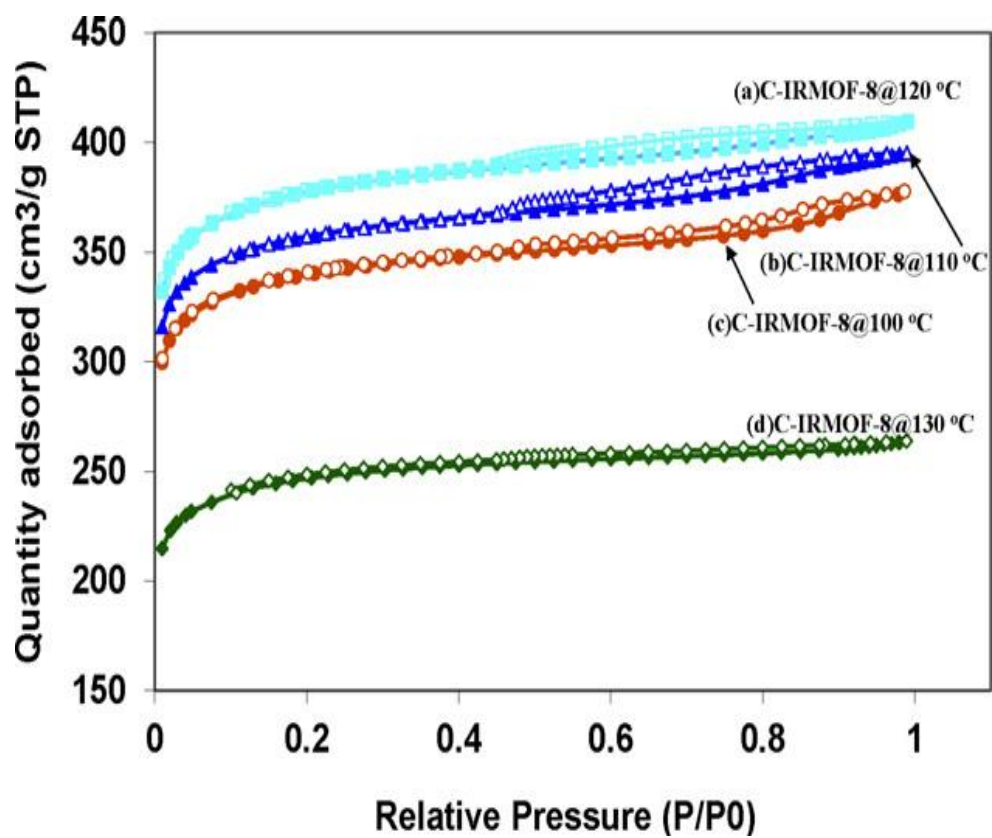


Figure 3.6 N₂ adsorption–desorption isotherms of C-IRMOF-8 synthesized by a conventional one-spot solvothermal method at (a) 120 °C, (b) 110 °C, (c) 100 °C, (d) 130 °C. The Open symbols represent desorption and filled symbols represent adsorption.

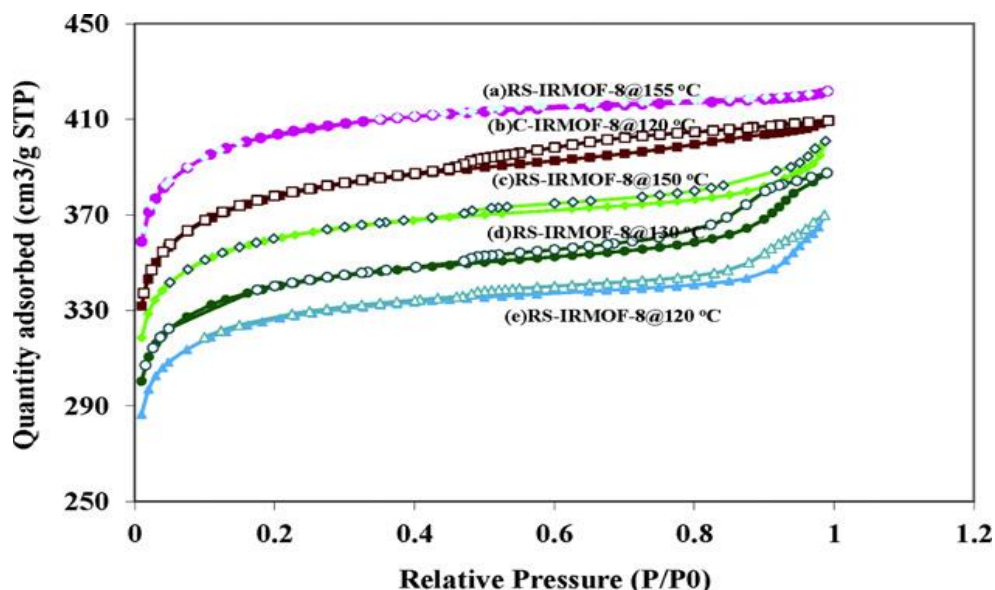


Figure 3.7 N₂ adsorption-desorption isotherms for IRMOF-8 prepared by the rapid solvothermal method (RS-IRMOF-8) (a) 155 °C, (c) 150 °C, (d) 130 °C, (e) 120 °C compared to conventional one-spot solvothermal method (b) (C-IRMOF-8) at 120 °C. Open symbols represent desorption and filled symbols represent adsorption

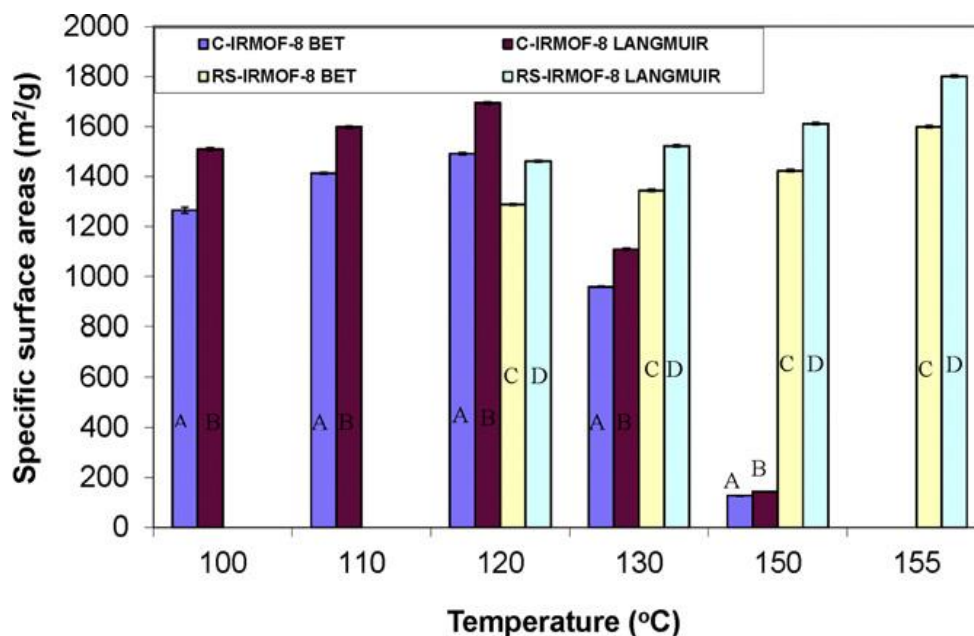


Figure 3.8 Correlation between SSA and temperature of IRMOF-8 prepared by the rapid solvothermal method (RS-IRMOF-8 (C and D)) compared to a conventional one-spot solvothermal method (C-IRMOF-8 (A and B)).

Table 3.2 Summary of synthesis parameters and results of C-IRMOF-8

OVEN TEMP. (°C)	COLOR OF PRODUCT.	SURFACE AREA (m ² /g)	PORE VOL. (cm ³ /g) @P/Po=0.50	PORE SIZE (nm)	H ₂ Wt.% @ -196°C, 1 atm
80	Cream	89.0L, 69.4B	0.0347.(t-plot micropore vol. =0.00649)	2.26	0.20
100	Cream	1509L, 1265B	0.5421.(t-plot micropore vol= 0.4551)	1.71	1.58
110	Yellow	1598L, 1413B	0.5701.(t-plot micropore vol= 0.4812)	1.60	1.70
120	Yellow	1694L, 1491B	0.6030.(t-plot micropore vol= 0.5036)	1.62	1.74
130	Yellow	1109L, 959B	0.3933.(t-plot micropore vol= 0.3246)	1.63	1.20
150	Light brown	143L, 127B	0.0507.(t-plot micropore vol=0.0445)	1.59	0.36

Table 3.3 Summary of synthesis parameters and results of RS-IRMOF-8.

OVEN TEMP. (°C)	COLOR OF PRODUCT.	SURFACE AREA (m ² /g)	PORE VOL. (cm ³ /g) @ P/Po=0.50	PORE SIZE (nm)	H ₂ Wt.% @ -196°C, 1 atm
100	White	315L, 269B	0.1149.(t-plot micropore vol. =0.083)	1.71	N.A
110	White	708L, 610B	0.2539.(t-plot micropore vol= 0.1963)	1.66	0.82
120	Cream	1461L, 1288B	0.5189.(t-plot micropore vol= 0.4384)	1.61	1.58
130	Cream	1522L, 1344B	0.5428.(t-plot micropore vol= 0.4619)	1.61	1.70
150 for 2.5h	Yellow	1611L, 1423B	0.5722.(t-plot micropore vol= 0.4861)	1.61	1.73
155 for 1h	Yellow	1801L, 1599B	0.6932.(t-plot micropore vol=0.5512)	1.60	1.76

3.6 H₂ ADSORPTION ISOTHERM OF C-IRMOF-8 AND RS-IRMOF-8

Low temperature and low pressure H₂ sorption isotherms of C-IRMOF-8 and RS-IRMOF-8 were also investigated. The data in Tables 3.2 and 3.3 show that, as expected, the materials adsorbed a considerable amount of dihydrogen. The H₂ wt. % adsorption increases to 1.74 as the synthesis temperature reached 120 °C and then decreases. The curves in Fig. 3.9(a)–(f), which compare the as-synthesized C-IRMOF-8 and RS-IRMOF-8, are Type-I reversible isotherms with no hysteresis. This is another indication that these are microporous materials. The unsaturation in the H₂ adsorption isotherms suggests that additional H₂ uptake will occur at higher pressure. Based on Fig. 3.9(f), the RS-IRMOF-8 sample prepared at 155 °C adsorbs 1.76 wt. % H₂ at 1 atm and -196 °C. This value is comparable to the C-IRMOF-8 sample in Fig. 3.9(a) prepared at 120 °C with an uptake of 1.74 wt. %. This further indicates that the rapid solvothermal method is an effective method for the preparation of IRMOF-8.

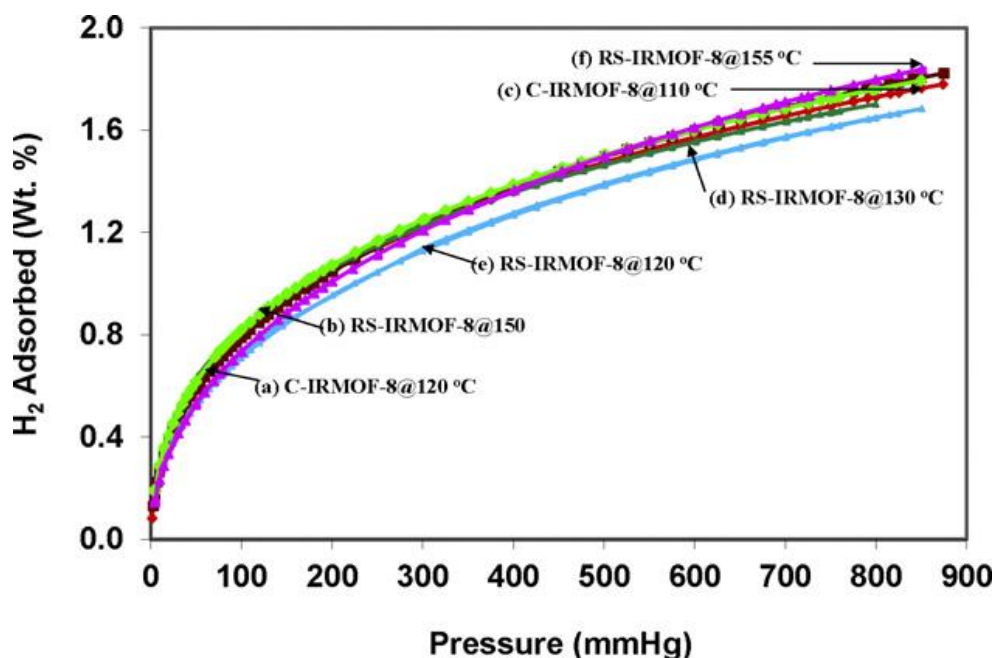


Figure 3.9: Hydrogen sorption isotherms for C-IRMOF-8 at (a) 120 °C, (c) 110 °C and RSIRMOF-8 at (b) 150 °C, (d) 130 °C, (e) 120 °C and (f) 155 °C at 1 atm.

3.7 CONCLUSION

This research has shown that rapid solvothermal synthesis of IRMOF-8 with permanent porosity can be carried out in 2–4 h, as opposed to traditional solvothermal methods which may take several hours (20 h) to days. BET analysis showed that the C-IRMOF-8 and RS-IRMOF-8 samples had pore volumes of 0.603 cm³/g STP and 0.693 cm³/g STP with SSA of 1694 and 1801 m²/g, respectively at the optimum temperatures. The fact that RS-IRMOF-8 had surface areas and hydrogen storage capacities that were equal to or greater than that obtained for the C-IRMOF-8 indicates that the rapid solvothermal synthesis is not only faster; it is more efficient. No exchange solvent or extended immersion in other exchange solvents was necessary thus making this method more

environmentally friendly. The results of this research are hoped to be extrapolated to the synthesis of other MOFs.

CHAPTER FOUR

4 EFFECTS OF NITRO-FUNCTIONALIZATION ON THE GAS ADSORPTION PROPERTIES OF ISORETICULAR METAL-ORGANIC FRAMEWORK-EIGHT (IRMOF-8)

To the best of our knowledge, the functionalization of IRMOF-8 remains mostly unexplored to date. A study by Cao et al. [45] has shown that the introduction of strong electrophilicity (electron withdrawing group) on the BDC (benzene dicarboxylic acid) linker enhanced the spillover capacity. Other studies have also shown that the introduction of polar substituent group such as $-OH$, $-COOH$ or NH_2 on the aromatic linker increases the CO_2 -linker affinity and enhances the adsorption. Similar findings have also shown that the introduction of $-Br$ functionality can also improve the binding strength of other strategic gases (CH_4 or H_2) to the MOFs [3, 11, 14, 15, 18, 28, 29, 33, 34, 38, 40, 43, 46-49, 57, 64, 86-96] It is in the light of this that we attempt to functionalize the organic linker of IRMOF-8 for improved gas storage capacity. This research reports the synthesis of IRMOF-8- NO_2 synthesized by functionalizing the linker of IRMOF-8 (that is 2, 6-naphthalenedicarboxylic acid). The new linker is 4, 8-dinitro-2, 6 naphthalenedicarboxylic acid.

4.1 X-RAY DIFFRACTION OF IRMOF-8 AND IRMOF-8- NO_2

X-ray diffraction analysis was done to confirm the formation of any new phases upon reaction of the organic linkers with $Zn(NO_3)_2 \cdot 6H_2O$. A comparison of the patterns in

Figs. 4.1(a-e) reveals some significant differences. Fig. 4.1(a) shows the x-ray diffraction pattern of the organic linker (2, 6-H₂NDC) for pure IRMOF-8. The peaks at 15, 27 and 41° are totally absent or diminished in the functionalized linker (4, 8-DN-H₂NDC) in Fig. 4.1(b). However, both linkers show a similar peak at 44.1° which is greatly increased in intensity in Fig. 4.1(b). There are also two peaks at 11.6 and 25.9° that were present in the functionalized linker and not in the 2, 6-H₂NDC. All of this indicates the formation of a new crystal system. The XRD pattern in Fig. 4.1(c) for Zn(NO₃)₂·6H₂O has been included for comparison. The XRD peaks in Fig. 4.1(d) are those of IRMOF-8-NO₂. As expected, these peaks are very similar to the peaks of IRMOF-8 in Fig. 4.1(e) but with a missing peak at 6.38° due to symmetry changes upon solvent removal [62, 97, 98].

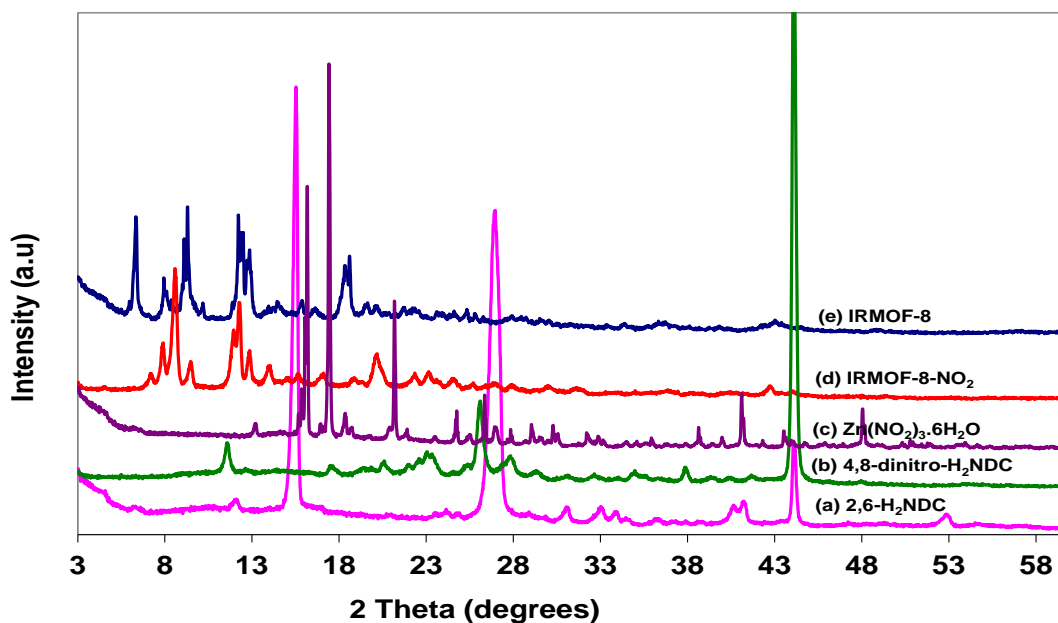


Figure 4.1 XRD patterns of reactants and products (d) IRMOF-8-NO₂ (e) IRMOF-8.

4.2 INFRARED SPECTROSCOPY OF IRMOF-8 AND IRMOF-8-NO₂

Infrared Spectroscopy was done to confirm the XRD findings that functionalization of the IRMOF-8 was achieved. Figs. 4.2(a, b) contain the FTIR spectra for the organic linkers used in the synthesis of IRMOF-8 (Fig. 4.2(c)) and IRMOF-8-NO₂ (Fig. 4.2(d)) respectively. Both spectra for the linkers have strong carboxylic acid C=O bands (stretching vibration) between 1700-1650 cm⁻¹ (the red dots). It is evident that these bands are absent in Figs. 4.2(c, d). This suggests that both IRMOF-8 and IRMOF-8-NO₂ are fully coordinated to the zinc oxide metal cluster through their carbonyl functional groups [99, 100]. Fig. 4.2(b) has most of the bands in Fig. 4.2(a) except for the band at 1530 cm⁻¹ (indicated by a green square). This band is related to the N=O stretching vibration. Fig. 4.2(d) has the same bands as Fig. 4.2(c) except for a band at 1530 cm⁻¹. The IR spectra in Fig. 4.2(b, d, e) further confirms the presence of the nitro-functional groups in the linker (4, 8-dinitro-2, 6-naphthalenedicarboxylic acid), Fig. 4.2(b) and IRMOF-8-NO₂, Fig. 4.2(d). The strong bands at 711, 721 and 720 cm⁻¹ seen in Fig. 4.2(b, d and e) are C-H stretches caused by aromatic monosubstitution on the benzene ring (700-750 cm⁻¹ and 690-710 cm⁻¹ range). It is evident from all this that the modified MOF is IRMOF-8 but with a nitro-functional group. Fig. 4.2(e) is the FTIR spectrum of IRMOF-8-NO₂ after the BET and HPVA sorption analysis at different temperatures. It is observed that before and after analyzing the nitro-functionalized MOF (Fig. 4.2(d and e)), maintained its integrity and was not converted to an amine (NH₂) functionality. Also, after synthesis, the nitro group was not compromised (Fig 4.2 b and d).

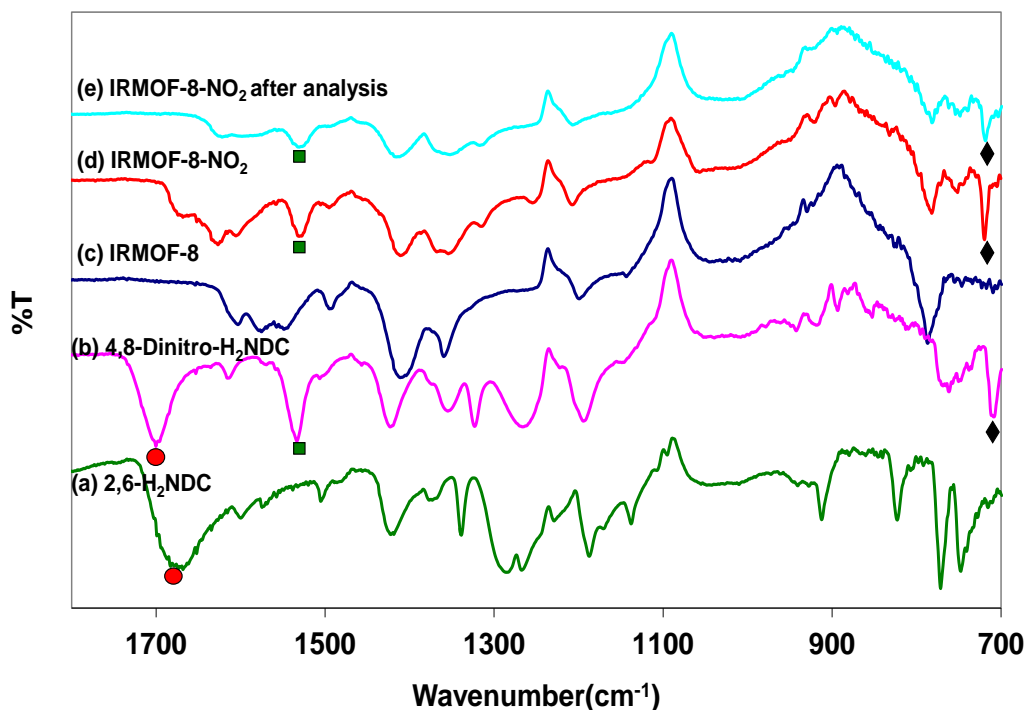
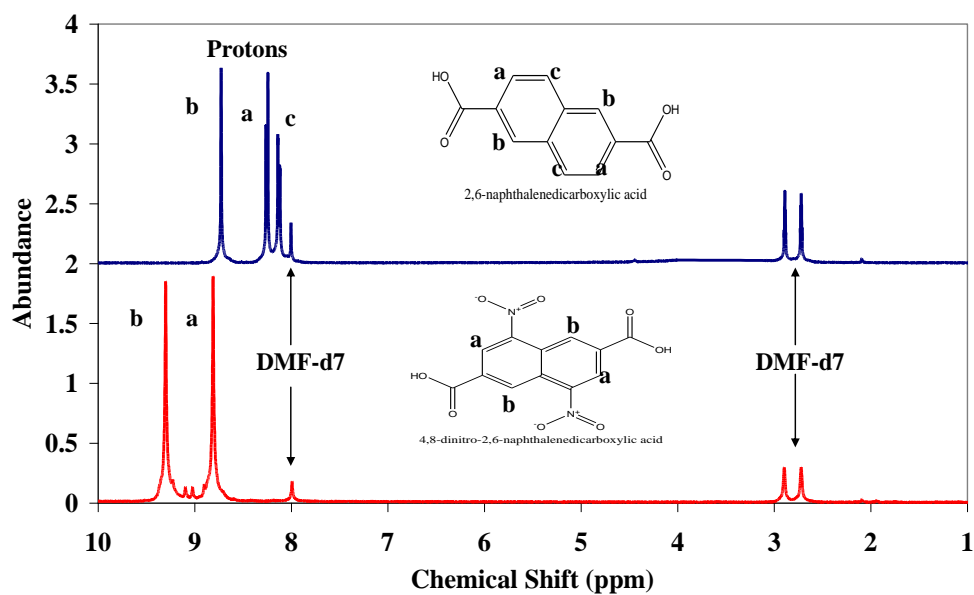
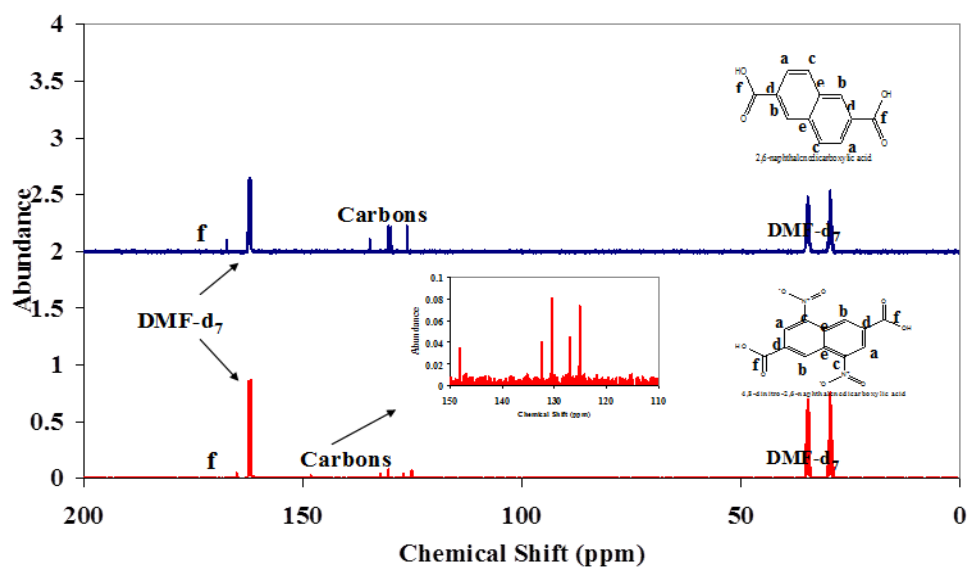


Figure 4.2 Comparative FTIR patterns of organic linkers and products, before and after gas sorption analysis (■ represents the nitro functional group, ● is the carboxylic functional group).

4.3 ^1H AND ^{13}C NMR OF LINKERS

NMR spectroscopy was used to further characterize the linkers and confirm that the functionalization of 2, 6- H_2NDC was achieved. Fig. 4.3(a) shows the ^1H NMR spectrum of 2,6- H_2NDC (top blue spectrum) and 4,8-dinitro-2,6- H_2NDC (lower red spectrum). DMF- d_7 (solvent) chemical shift values are seen at 2.72, 2.90 and 7.99 ppm respectively. These values are in close agreement with the predicted resonance (signal) values of 2.75, 2.92 and 8.03 ppm using the ChemDraw[®] Ultra 8.0 [79]. The ^1H NMR spectrum of 2,6- H_2NDC showed that this molecule has three types of protons (doublet (a), singlet (b), doublet (c)) based on the chemical environment of the neighboring hydrogen atoms (six

protons in all). Their chemical shift values are 8.73, 8.24 and 8.14 ppm (b, a, and c respectively). These chemical shift values are in reasonable agreement with the predicted values (8.54, 8.19 and 7.88 ppm). On functionalization, the molecule; 4,8-dinitro-2,6-H₂NDC (lower red spectrum) had four protons (2 types based on the new chemical environment). The protons 'b' and 'a' are further deshielded as a result of the electronegative nitrogen group attached. The electron density around the neighboring protons decreases causing the peaks to appear further downfield at 9.30 and 8.90 ppm. The carboxylic acid OH was not seen, but the presence of the carbonyl carbon was observed in the carbon-13 NMR (¹³C NMR from 0-200 ppm). Fig. 4.3(b) shows the ¹³C NMR for both organic linkers. The ¹³C NMR of 2, 6-H₂NDC (top blue spectrum) and 4, 8-dinitro-2, 6-H₂NDC (lower red spectrum) both showed the carbonyl carbon (f) at 167.4 and 165.2 ppm respectively and are in good agreement with the predicted software value of 169.4 ppm. However due to the nitro group in the 4,8-dinitro-2,6-H₂NDC, carbon "C" was further deshielded to a chemical shift value of 148.2 ppm (148.5 ppm predicted ppm) as opposed to the 134.7 ppm (134.0 ppm predicted) of the non-functionalized linker. These results confirm that the functionalization of 2,6-H₂NDC was achieved. This is in accordance with the conclusion of the FTIR analysis that the nitro group was present in the linker and the carbonyl group was responsible for the complex formation.

^1H NMR OF THE ORGANIC LINKERSFigure 4.3(a) ^1H NMR of 4,8-Dinitro-2,6- H_2NDC and 2,6- H_2NDC . ^{13}C NMR OF THE ORGANIC LINKERSFigure 4.3(b) ^{13}C NMR of 4,8-Dinitro-2,6- H_2NDC and 2,6- H_2NDC .

4.4 THERMOGRAVIMETRIC ANALYSIS OF IRMOF-8 AND IRMOF-8-NO₂

Thermogravimetric analysis was done to determine the effect of nitro-functionalization of the thermal stabilities of the linkers and MOFs. Fig. 4.4(a-d) shows the TGA curves depicting the thermal stabilities of IRMOF-8-NO₂, 4,8-dinitro-2,6-H₂NDC, 2,6-H₂NDC and pristine IRMOF-8 respectively. Both linkers have thermal stabilities up to 350 °C as seen in Fig 4.4(b, c). The decomposition curve in Fig. 4.4(c) dropped almost to 0 (zero) weight % while the decomposition curve in Fig. 4.4(b) plateaus out at about 40 weight %. This difference can be attributed to the presence of nitro-functional group in the linker in Fig. 4.4(b). The IRMOF-8-NO₂ in Fig. 4.4(a) has thermal stability up to 350 °C whereas the pristine IRMOF-8 in Fig. 4.4(d) is stable up to 450 °C. In effect, pristine IRMOF-8 shows a stronger coordination between the zinc oxide cluster and its linker than the IRMOF-8-NO₂ [34]. In Fig 4.4(a), there is an initial gradual weight loss which increases to about 25% between 100-250 °C. This temperature range is related to the boiling point of water (100 °C) and the synthesis solvent, DMF (153-155 °C). The TGA curve decomposed to 13 wt% indicating the release of more gaseous products, which is likely due to weak binding caused by the functionalization.

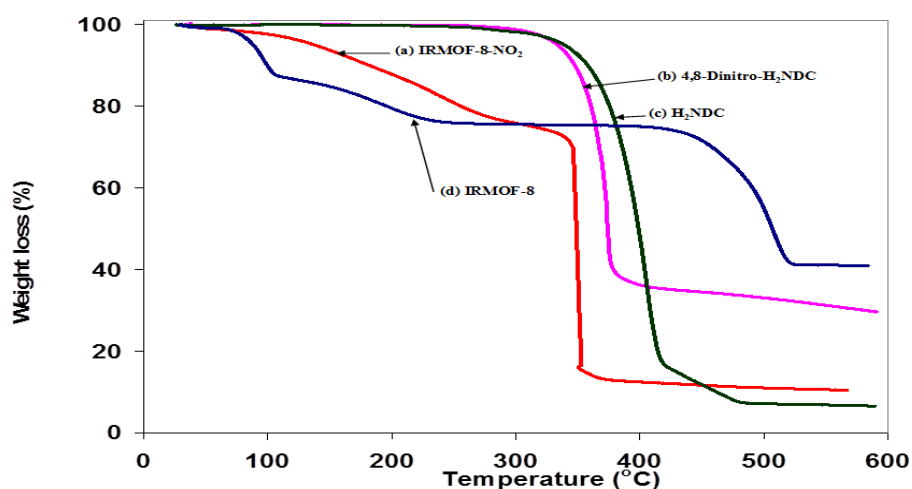


Figure 4.4 TGA curve of organic linker (b, c) and products (a, d)

4.5 RESIDUAL GAS ANALYSIS OF IRMOF-8 AND IRMOF-8-NO₂

Residual gas analysis was done to determine the nature and relative amounts of gases released upon decomposition of the pristine and functionalized MOFs. Figs. 4.5(a i-v) and 4.5(b i-ii) show the residual gas analyses of degassed IRMOF-8-NO₂ and pristine IRMOF-8 respectively. A comparison of the gas analysis curves in Figs. 4.5a and 4.5b for IRMOF-8-NO₂ and IRMOF-8 confirmed the TGA findings that the IRMOF-8-NO₂ releases more gaseous products than the pristine IRMOF-8. Hydrogen, carbon dioxide and carbon monoxide were released in both materials but much more was released in the functionalized material. Nitrogen and methane were released from the IRMOF-8-NO₂ but not from the IRMOF-8.

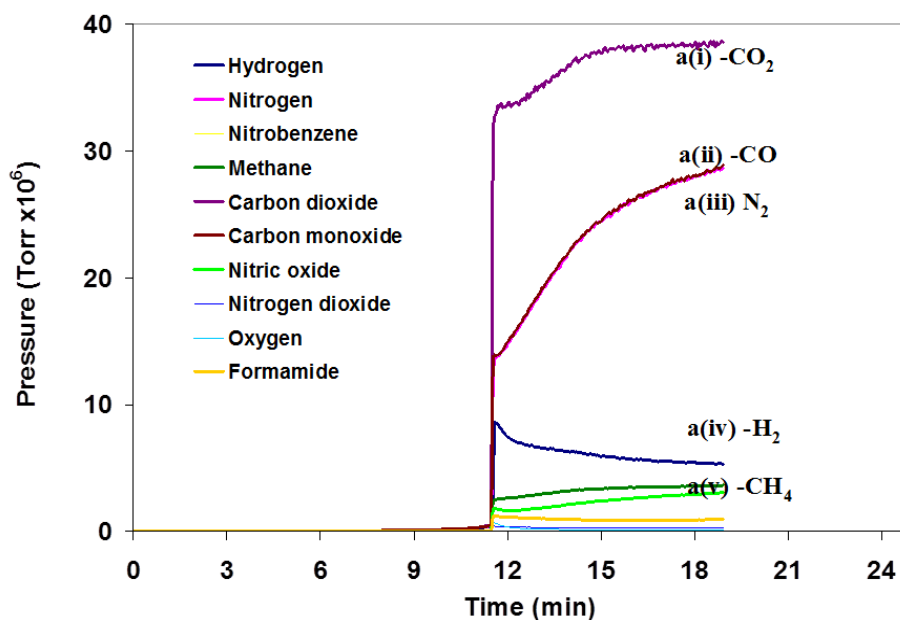


Figure 4.5a RGA signal of degassed IRMOF-8-NO₂

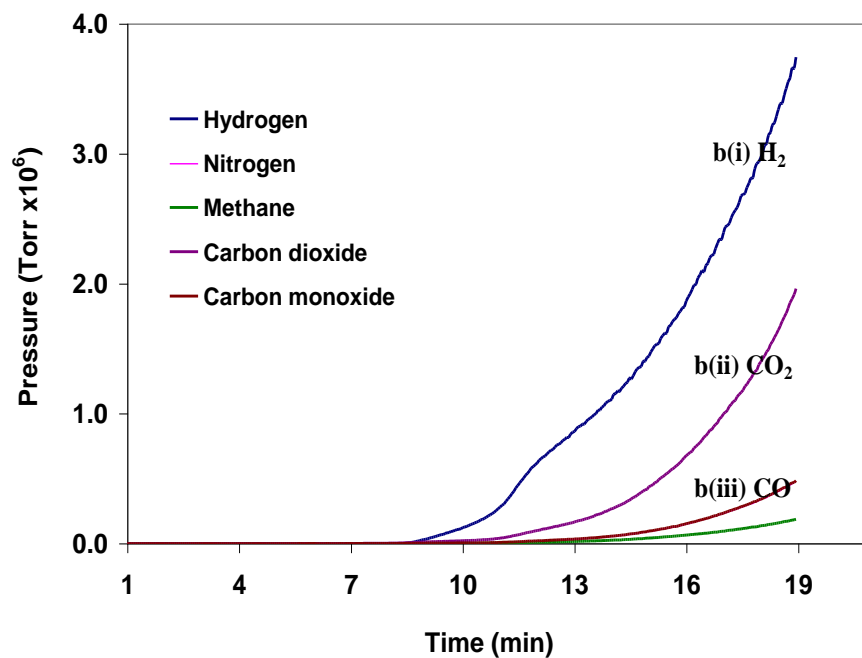


Figure 4.5b RGA signal of degassed IRMOF-8

4.6 LASER DIFFRACTION ANALYSIS OF IRMOF-8 AND IRMOF-8-NO₂

Laser diffraction particle size analysis was done to determine if there were any differences in particle size between IRMOF-8-NO₂ and IRMOF-8. Figure 4.6 showed that the nitro-functionalized IRMOF-8 had a smaller particle size (a mean value of $15.65 \pm 0.406 \mu\text{m}$ as opposed to $24.185 \pm 0.377 \mu\text{m}$ for the bulk IRMOF-8). While the pristine metal-organic framework showed a uniform particle size distribution, the functionalized material on the other hand had a bimodal particle size distribution. The smaller particle size observed in the functionalized material can serve as a positive property in its gas storage ability. Zhao et al [4] had earlier discussed about the effect of small particle size leading to higher hydrogen adsorption. This may be one of the factors that is partially

responsible for the higher than expected capacity of IRMOF-8-NO₂ even with its smaller pore volume and SSA as seen in section 4.8.

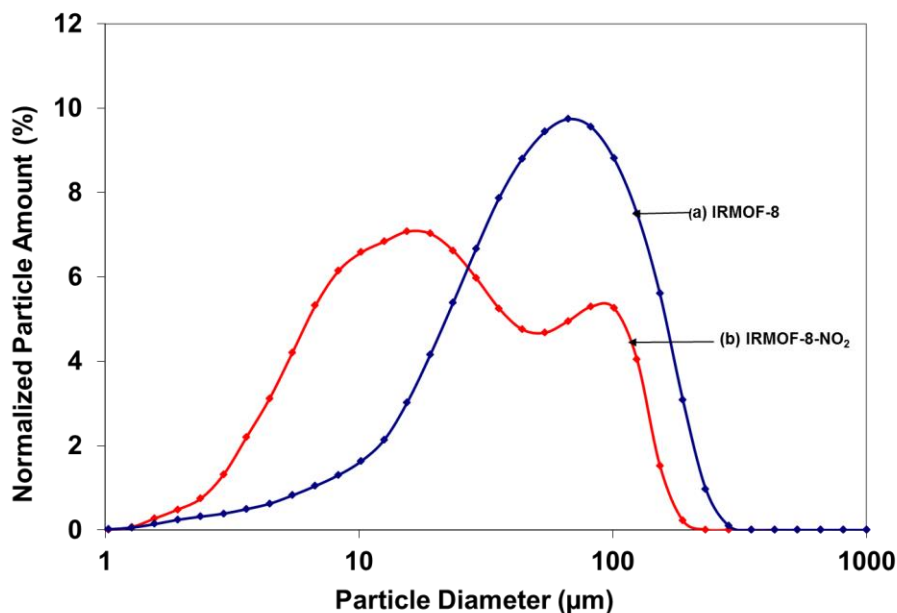


Figure 4.6 Particle size distributions of IRMOF-8 and IRMOF-8-NO₂

4.7 SURFACE AREA AND POROSITY OF IRMOF-8 AND IRMOF-8-NO₂

The surface areas and porosities of IRMOF-8 and IRMOF-8-NO₂ were determined volumetrically from the N₂ adsorption-desorption isotherms at -196 °C in the range of $1.00 \times 10^{-3} \leq P/P_0 \leq 1.00$. The Type-I isotherms shown in Fig. 4.7(a, b) are those of the pure IRMOF-8 and the IRMOF-8-NO₂ obtained with hysteresis in the desorption isotherm. This is indicative of different pore size distribution (mesoporous or macroporous pores in addition to micropores) [36, 43, 44, 48, 101]. The insert is the IRMOF-8-NO₂ showing the hysteresis with specific surface areas (SSA) of 823 m²/g and 926 m²/g based on the BET and the Langmuir equations. The pore volume was found to

be $0.3218 \text{ cm}^3/\text{g}$ at a relative pressure of $P/P_0 = 0.50$. This value is 50 % of that for the pure IRMOF-8 as seen in Table 4.1. The steep rise usually seen at the end of the isotherm was barely noticeable. The average pore size was found to be 1.57 nm, which falls into the category of micropores. This pore size is smaller than the pore size of the pure IRMOF-8 synthesized at $155 \text{ }^\circ\text{C}$ (1.61 nm with surface areas of $1801 \text{ m}^2/\text{g}$ Langmuir, $1599 \text{ m}^2/\text{g}$ BET and pore volume of $0.639 \text{ cm}^3/\text{g}$). This variation in physisorption properties is confirmed by the earlier statement of Duren et al. [88] that “the extra functional groups lead to a decrease in the free volume and surface areas.”

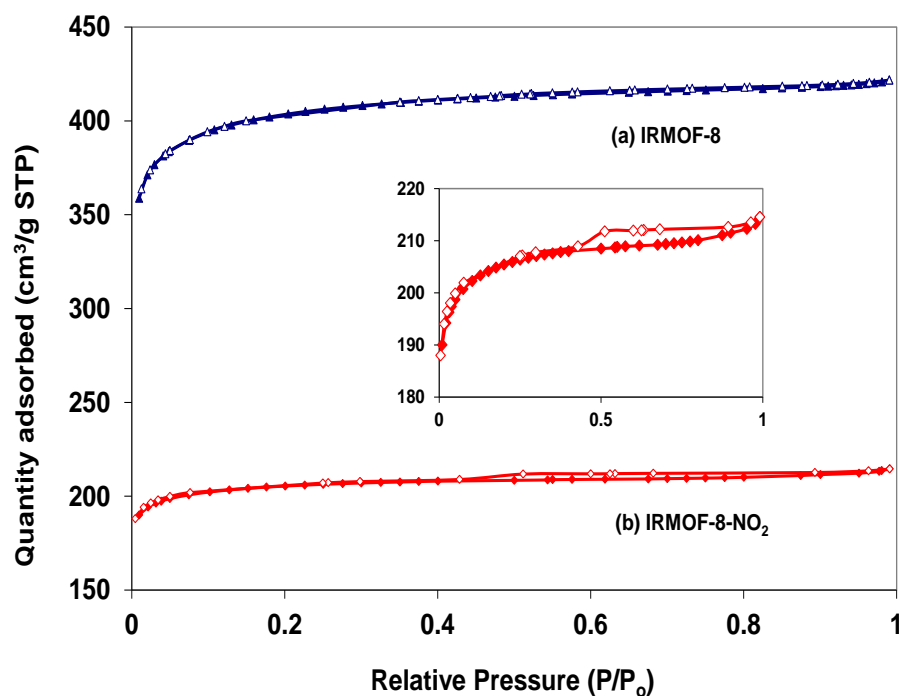


Figure 4.7 (a) LN_2 Nitrogen-adsorption-desorption isotherms of (a) pure IRMOF-8 (b) IRMOF-8- NO_2 (\square is desorption \blacksquare is adsorption isotherm). The inset is LN_2 Nitrogen-adsorption-desorption isotherms for IRMOF-8- NO_2

Table 4.1 Physisorption properties of IRMOF-8-NO₂ and IRMOF-8

PROPERTIES	IRMOF-8-NO ₂ @120 °C	IRMOF-8 @155°C
Surface area(m ² /gSTP) BET / Langmuir	832/ 926	1599/ 1801
Pore Volumes (cm ³ /g) @P/Po =0.50 and 0.99	0.322 and 0.341	0.639 and 0.660
t-plot micropore volume @P/Po =0.50 and 0.99	0.292 and 0.292	0.551 and 0.551
Pore Size nm @P/Po =0.50 and 0.99	1.567 and 1.612	1.598 and 1.631
H ₂ Wt.% at 1atm and different temperatures	1.20% at -196 °C 0.043% at-78.5 °C 0.012% at 0 °C 0.007% at 25 °C	1.67% at -196 °C 0.04% at-78.5 °C 0.01% at 0 °C 0.01% at 25 °C
H ₂ Wt.% at high pressure and different temperatures (approximately 96 bar for IRMOF-8-NO ₂)	2.20% at -196 °C 1.35% at-78.5 °C 0.50% at 0 °C 0.43% at 25 °C	3.2% at -196 °C at 93 bar 1.50% at-78.5 °C at 90 bar 0.49% at 0 °C at 80 bar 0.43% at 25 °C at 80 bar
Enthalpy of adsorption of the MOFs. (ΔH) in kJ/mol.	6.99±0.25 kJ/mol at low H ₂ pressure and 6.57±0.26 kJ/mol at high H ₂ pressure	6.1 kJ/mol ref 2, 4, 18, 59. 5.90±0.35 kJ/mol at low pressure and 6.01±0.05 at high pressure in this work.
Sticking Factor, θ (g m ⁻²) At High Pressures	0.0026 at -196 °C 0.0016 at-78.5 °C 0.00060 at 0 °C 0.00052 at 25 °C	0.0020 at -196 °C 0.00094 at-78.5 °C 0.00031 at 0 °C 0.00027 at 25 °C

4.8 H₂, CH₄ AND CO₂ ADSORPTION ISOTHERMS OF IRMOF-8 AND IRMOF-8-NO₂

Low and high pressure sorption isotherms of IRMOF-8-NO₂ and pristine IRMOF-8 were investigated at -196, -78.5, 0 and 25 °C in order to determine the amounts of H₂, CH₄ and CO₂ that would adsorb on the MOFs at different temperatures. In Fig. 4.8(a, b) a comparison is made of the low pressure hydrogen adsorption capacity of the pure IRMOF-8 and IRMOF-8-NO₂ respectively at -196 °C. The hydrogen capacity of IRMOF-8-NO₂ was 1.20 wt. %, which is fairly close to that of the pristine IRMOF-8 (1.67 wt.% at 1 atm.) even though the surface areas differ by a factor of two. It has been reported that at low temperature and pressure, functionalization and catenation will increase hydrogen uptake [2, 3, 16, 48, 88, 102-104]. In both materials, saturation was not reached indicating higher uptake as pressure increases. At high pressure, saturation was reached at about 20-30 bar and the full H₂ uptake capacities, as seen in Fig. 4.9, were 3.2 and 2.2 wt% for IRMOF-8 and IRMOF-8-NO₂ respectively. A comparison of the physisorption properties of IRMOF-8 and IRMOF-8-NO₂ is given in Table 4.1.

Methane and carbon dioxide adsorption analyses were also carried out at low pressure Fig. 4.10(a i-iv) and 4.10(b i-iv) and at high pressures Fig. 4.11 (a i-iv) and 4.11 (b i-iv). The results are summarized in Tables 4.2 and 4.3. The results show that the MOFs have a much higher adsorption affinity for these gases than they have for hydrogen. Perhaps the larger kinetic diameter of CO₂ and CH₄ (3.3 and 3.8 Å) favors their adsorption at near ambient temperatures. CO₂ also has a high quadrupole moment which makes it interact more with the framework [12, 16, 34, 35, 61, 68, 86-88, 91, 105-109]. At low pressure in

Fig. 4.10(b), the CO₂ capacity in the pristine IRMOF-8 was 13.75 wt%, which is equivalent to 70 cm³/g. This is in agreement with the report of Yao et al. [62] (77 cm³/g) at 273 K. In Fig. 4.11(a), saturation was not reached in both samples and this agrees well with simulation study carried out by Duren and co-worker as reported by Getman et al. [16] and also supported in ref [11]. The results also show that the pristine IRMOF-8 has an uptake of CO₂ at both low and high pressures that was much higher than that of IRMOF-8-NO₂. This is attributed to the higher SSA and pore volume of IRMOF. However, the amount of gas that was adsorbed is greater than expected based solely on the differences in particle size and pore volume. Since the surface area and pore volume of the IRMOF-8-NO₂ is only about half that of IRMOF-8 it was expected that the gas adsorption would only be half as well. The results in Tables 4.1–4.3 clearly show that the functionalized materials adsorbed significantly more than this.

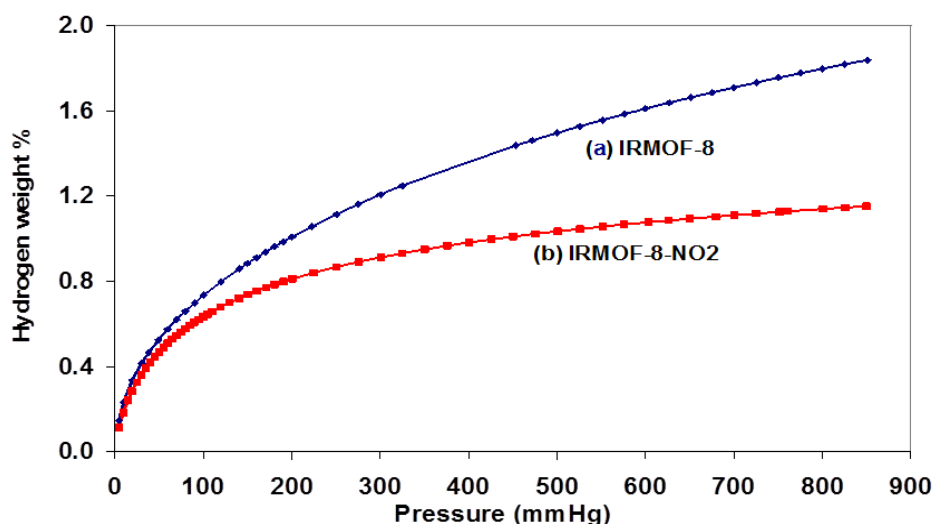


Figure 4.8 Low pressure H₂ sorption isotherm of (a) pure IRMOF-8 (b) IRMOF-8-NO₂ at -196 °C.

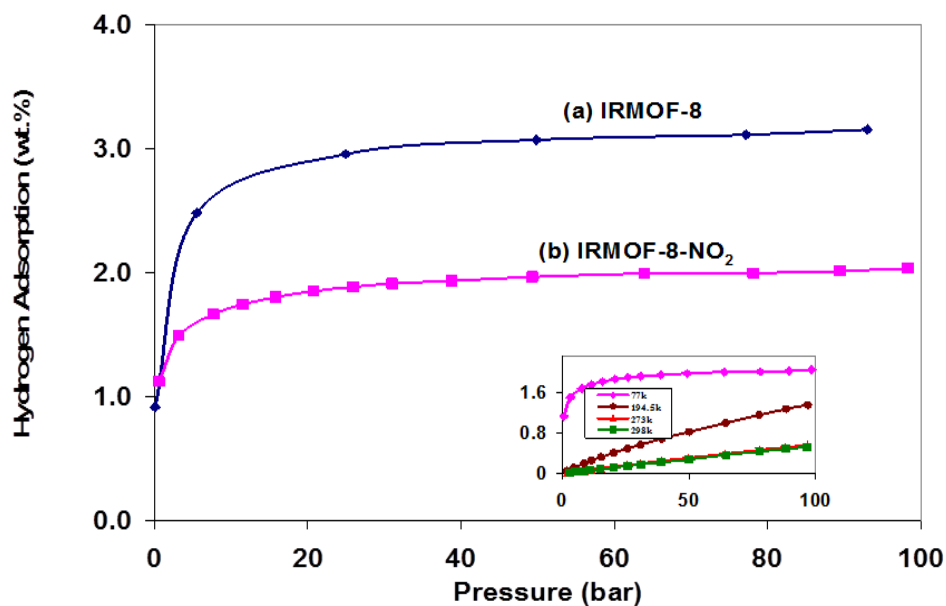


Figure 4.9 High pressure hydrogen sorption isotherms (a) pure IRMOF-8 (b) IRMOF-8-NO₂ at -196 °C. The inset shows the high pressure H₂ isotherm at different temperature for IRMOF-8-NO₂

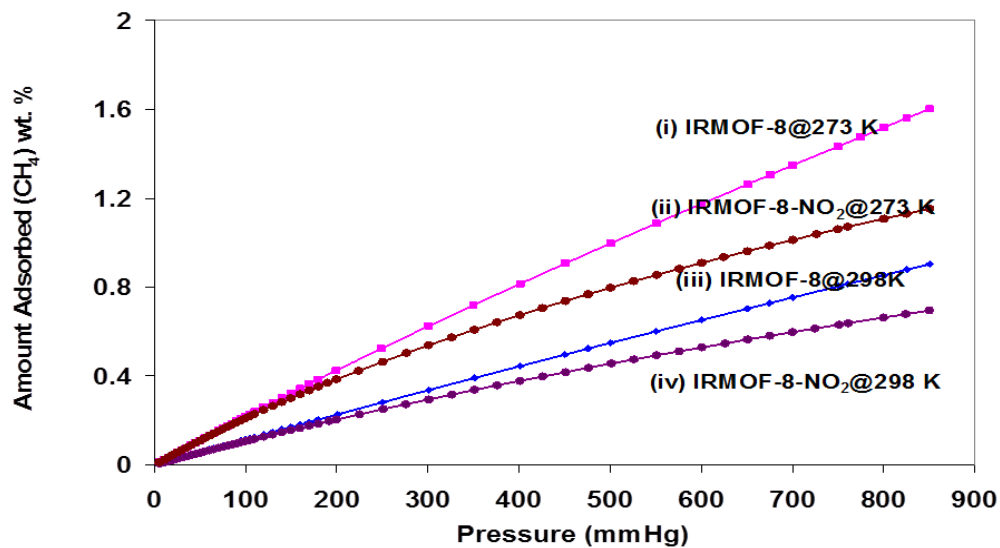


Figure 4.10a Low pressure CH₄ storage capacities of IRMOF-8-NO₂, Pure IRMOF-8 at 0 and 25 °C.

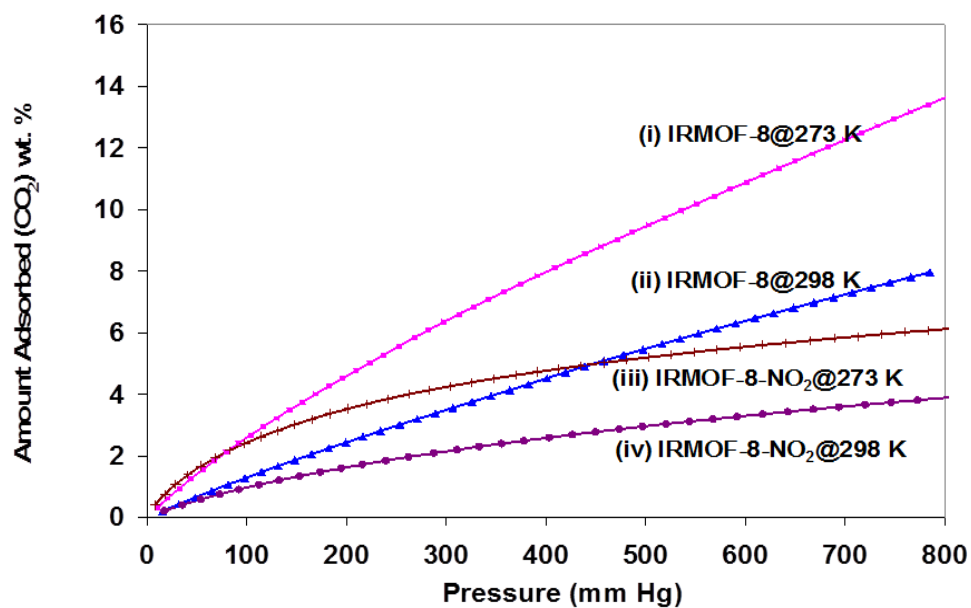


Figure 4.10b Low pressure CO₂ storage capacities of IRMOF-8-NO₂ and pure IRMOF-8 at 0 and 25 °C

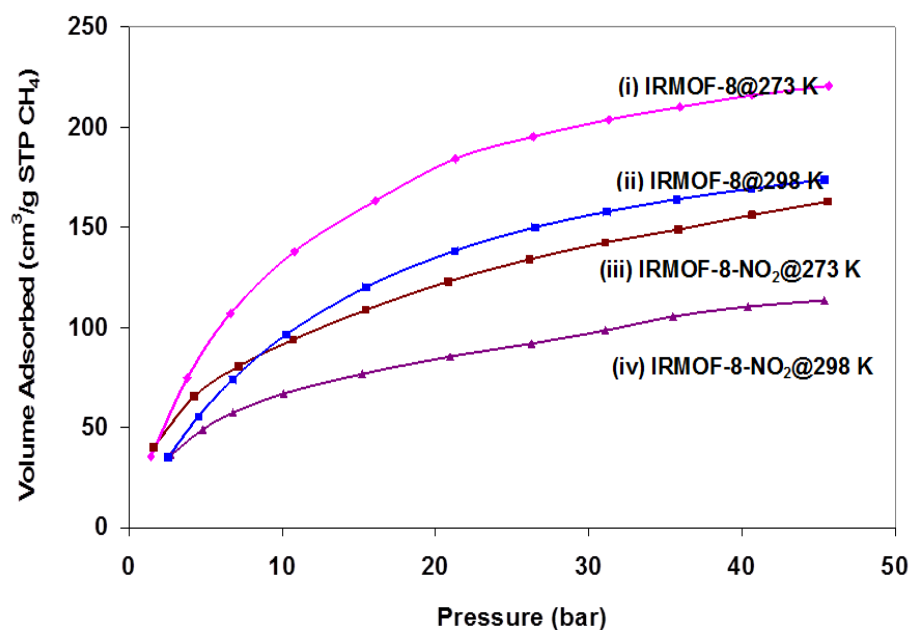


Figure 4.11a High pressure CH₄ storage capacities of IRMOF-8-NO₂, Pure IRMOF-8 at 0 and 25 °C.

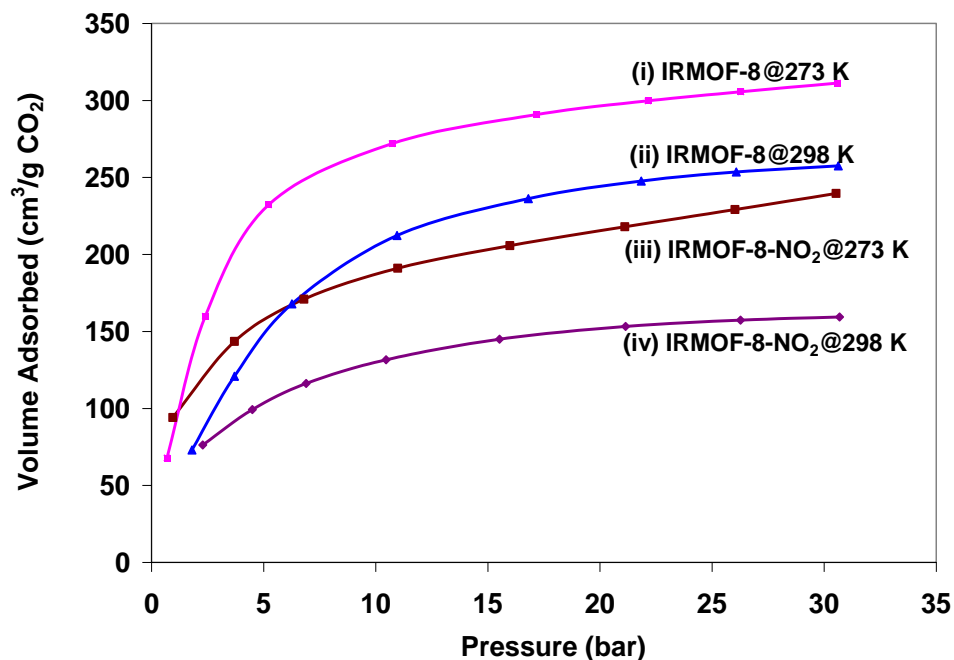


Figure 4.11b High pressure CO₂ storage capacities of IRMOF-8-NO₂ and pure IRMOF-8 at 0 and 25 °C

Table 4.2: Methane adsorption and the sticking factor (θ)

Materials	Surface area (m ² /g)		Pore vol. (cm ³ /g)	Temp. (K)	CH ₄ wt.% (bar)	v/v	cm ³ /g	ΔH (kJ/mol)	θ (g m ⁻²)	Ref
	BET	Langmuir								
IRMOF-8	1599	1801	0.66	273	15.03(35)		210	16.9	0.0094	this work
IRMOF-8	1599	1801	0.66	298	11.74(35)		164	16.9	0.0073	this work
IRMOF-8-NO ₂	832	936	0.34	273	10.68(35)		149	21.8	0.013	this work
IRMOF-8-NO ₂	832	936	0.34	298	7.80 (35)		108	21.8	0.0094	this work
IRMOF-991	2171	3179	0.68	298	- (35)		169	9.1		90
MIL-53(Al)	1100	1590	0.59	298	10.0 (35)	155		17		12, 14
MIL-53(Cr)	1100	1500	0.56	298	10.0 (35)	165		17		12, 14
PCN-14	1753		0.87	290	16.0 (35)	220	252	30		12, 14
PCN-11	1931	2442	0.91	298	14.1 (35)	171	228	14.6		12
HKUST	1502	2214	0.76	298	15.7(150)	228				12
HKUST	1502	2216		298	- (36)	109	200			14
MIL-101	2693/4230	4492/5900	1.303	298	14.2 (35)	72(110)	220			12, 14
MOF-5	2296	3840		-	(36)	135				14
IRMOF-3	2264	3062		298	(36)	120				12
IRMOF-6	2804	3305		298	(36)	155	240			12

Table 4.3: Carbon dioxide adsorption and the sticking factor (θ)

Materials	Surface area (m^2/g)		Pore vol. (cm^3/g)	Temp (K)	CO ₂ wt.% (bar)	v/v	mmol/g	ΔH (kJ/mol)	θ (g m^{-2})	Ref
	BET	Langmuir								
IRMOF-8	1599	1801	0.66	273	63.3(30)	----	14.4	21.1	0.040	this work
IRMOF-8	1599	1801	0.66	298	51.2(30)	----	11.7	21.1	0.032	this work
IRMOF-8-NO ₂	832	936	0.34	273	47.0(30)	----	11.0	35.4	0.056	this work
IRMOF-8-NO ₂	832	936	0.34	298	31.3(30)	----	7.2	35.4	0.038	this work
MIL-53(Al)	-----	1500	0.59	298	30.6(25)	225	10.0	21		12, 14, 35, 86
MIL-53(Cr)	-----	1500	0.56	298	30.6(25)	225	10.0	21		12, 14, 35, 86
MIL-101	4230	5900	1.303	298	---- (50)	390	40.0	44		12, 14, 35, 11
MOF-5	2296	3840		298	----(35)	290	21.7	34		14, 35, 66, 91
IRMOF-6	2804	3305		298	(40)	286	19.8			12, 14
HKUST	1502	2216		303	40.1(40)	210	10.7	35		14, 35
MOF-177	4750	5640		298/313	60.8 (40/50)	320	33.7			14, 35, 91

4.9 ANALYSIS OF STICKING EFFICIENCIES

In order to better understand the greater-than-expected adsorption of gases on the IRMOF-8-NO₂, a new concept called the sticking factor (defined as the percent gas adsorbed per gram of material per m² of surface area) was determined for the adsorption of each gas on the two MOFs at various temperatures. The sticking factor (θ) was calculated for each gas based on the following equation:

$$\theta = \frac{\% \text{ Hydrogen Adsorbed}}{\text{Surface Area } \left(\frac{\text{m}^2}{\text{g}}\right)} \quad (15)$$

The sticking factors for H₂, CH₄ and CO₂ are given in Tables 4.1, 4.2 and 4.3, respectively. The results in Table 4.1 show that the sticking factors for H₂ on IRMOF-8-NO₂ were greater than those for IRMOF-8 at all temperatures. This indicated that nitro functionalization produces greater sticking ‘efficiency’ for gas adsorption. It is also apparent that the sticking factors increase as the temperature decreases. The curves of sticking factor (θ) versus temperature in Fig. 4.12 show an inverse correlation between θ and temperature. The sticking factors for CH₄ and CO₂ in Tables 4.2 and 4.3 respectively show a similar trend. For both of these gases, the sticking factor is larger for adsorption

on the IRMOF-8-NO₂. For CH₄ and CO₂, analyses were done only at 0 and 25 °C. For both gases, the sticking factor is larger at the lower temperature. These results confirm that gas sticking efficiency increase as the temperature decreases and increases with the heat of adsorption and molecular weight of the gasses in Fig. 4.13 and 4.14

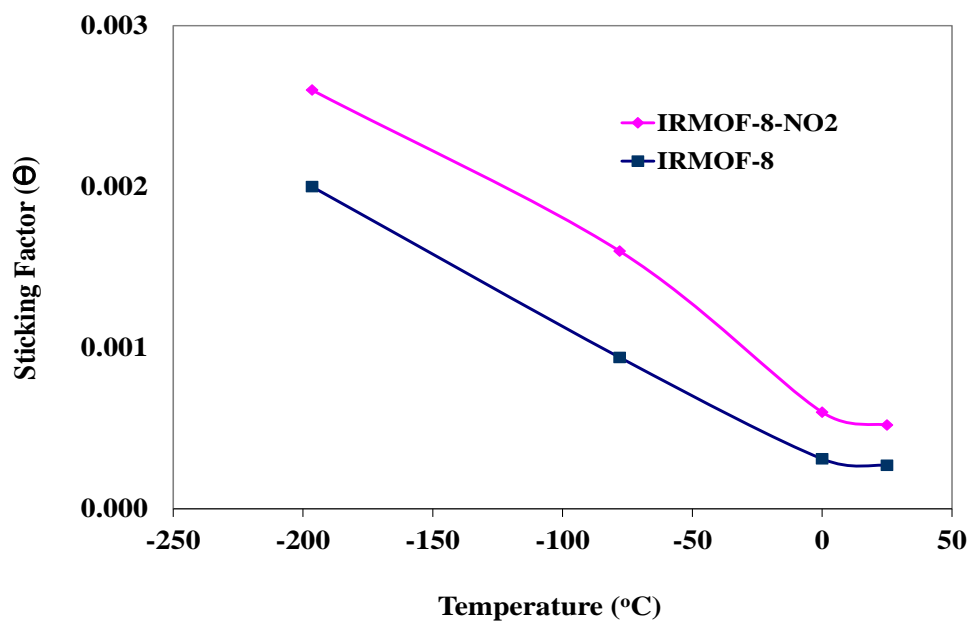


Figure 4.12 Sticking factor versus temperature for the adsorption of hydrogen on IRMOF-8-NO₂ and pristine IRMOF-8 at high pressure

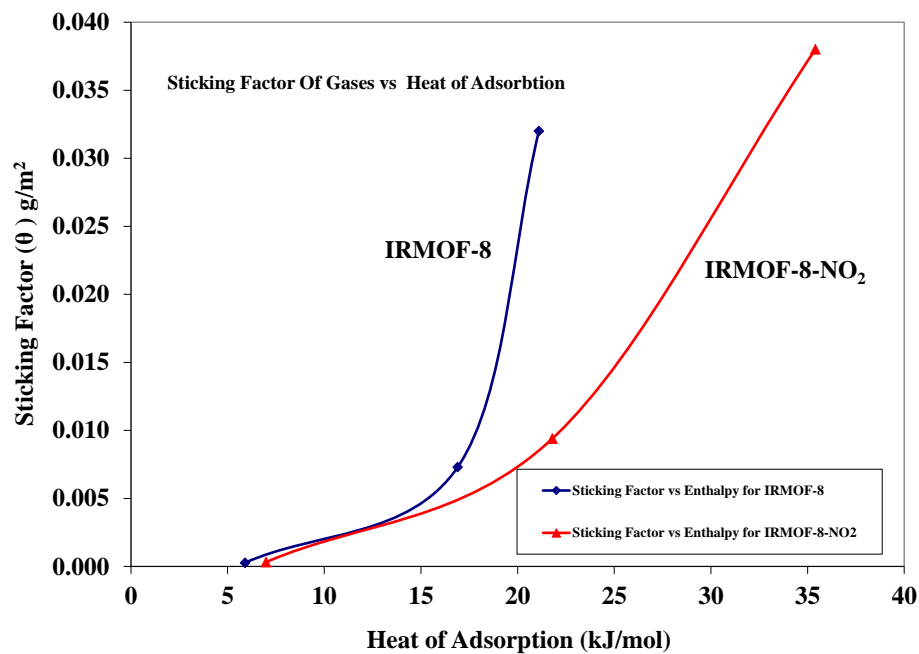


Figure 4.13 Sticking factor versus heat of adsorption of gases on IRMOF-8 and IRMOF-8-NO₂

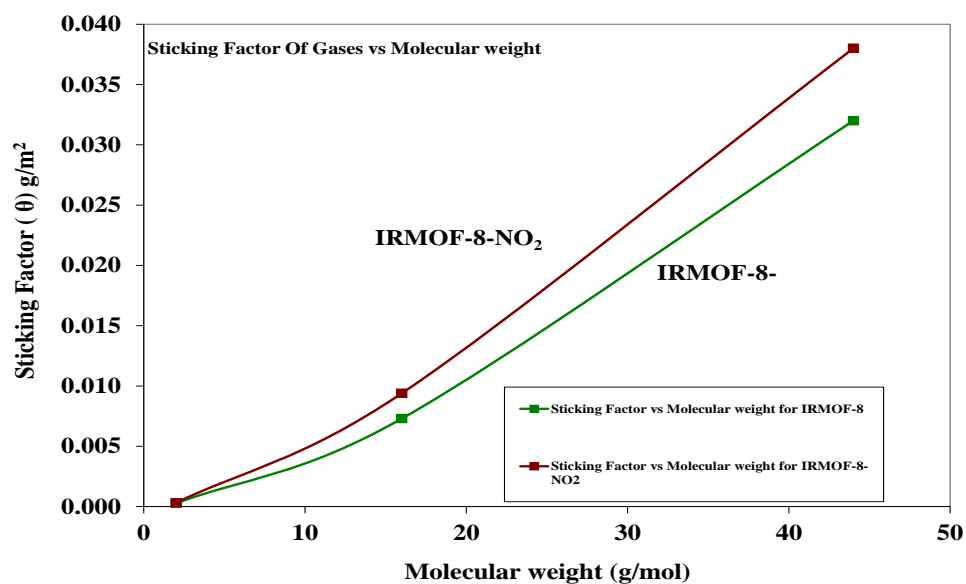


Figure 4.14 Sticking factor versus molecular weight of gases on IRMOF-8 and IRMOF-8-NO₂

4.10 HEAT OF ADSORPTION (ΔH) OF IRMOF-8-NO₂ AND IRMOF-8

In order to understand why sticking efficiencies are greater for IRMOF-8-NO₂ than IRMOF-8, isosteric heats of formation were determined for the adsorption of each gas on the two MOFs at various temperatures. Applying the Clausius-Clapeyron equation, the heat of adsorption was determined over a wide range of temperatures and pressures. The isotherms in Fig. 8 were converted to isobars and a van't Hoff plot of $\ln P$ versus T^{-1} (K⁻¹), obtained from these isobars, was used to calculate the isosteric heat of adsorption (Q_{st}). The van't Hoff equation [8, 18, 35, 107] is given as:

$$\frac{\Delta H}{RT^2} = -\left(\frac{\partial \ln P}{\partial T}\right)_q \quad (16)$$

Where ΔH is the isosteric heat of adsorption (kJ/mol), T (K) is the temperature, P is the adsorbate pressure in (bar), R is the universal gas constant and q is the constant adsorption amount.

Integrating equation 16 above gives:

$$\ln P = -\frac{\Delta H}{RT} + C \quad \text{Where } C \text{ is the constant of integration} \quad (17)$$

A plot of $\ln P$ vs T is given in Fig. 4. 15 and the ΔH can be calculated from the slope. The enthalpy value is 6.75 ± 0.26 kJ/mol. This is in agreement with Fig. 4.16 which contains plots of the isosteric heat of adsorption versus H₂ loading (wt. %) at high pressure up to 35 bar for IRMOF-8-NO₂ and IRMOF-8. The isosteric heats of adsorption for the functionalized material decrease systematically from an initial value of 6.99 kJ/mol to

4.06 kJ/mol at higher hydrogen loading. The isosteric heats of adsorption for the IRMOF-8 generally decrease up to a loading of 0.6 % H₂ then increase.

By modifying the van't Hoff equation and introducing two different temperatures (T₁, T₂) and pressures (P₁, P₂), Equation 18 was obtained and used in calculating the heat of adsorption at low and high CH₄ and CO₂ pressure for the parent IRMOF-8 and IRMOF-8-NO₂ in this study.

$$\ln P_1 - \ln P_2 = -\frac{\Delta H}{R} \left(\frac{1}{T_1} - \frac{1}{T_2} \right) \quad (18)$$

The enthalpies of adsorption obtained for methane adsorption on IRMOF-8-NO₂ at high pressure was 21.81±3.20 kJ/mol. The heat of adsorption of methane compares well with some selected IRMOFs studied by Duren et al. [90]. The adsorption capacities and enthalpies of this material also compare well with some other high SSA materials in Table 4.2, which meets the DOE target of 20 kJ/mol and 20% above the energy of the pristine material. Similar findings were observed for carbon dioxide uptake with comparable adsorption to some landmark MOFs for CO₂ capture at 273 K as seen in Table 4.3. Thermodynamically (enthalpy of 35.8 and 35.4 kJ/mol at low and high CO₂ uptake) it matches the enthalpy of the commercial zeolites or activated carbon material (-30 to -42 kJ/mol) [35]. The increased binding energy of CO₂ to IRMOF-8-NO₂ is a positive indication of the material's selectivity for the gas than pristine IRMOF-8, which has a lower value (21.1 kJ/mol) leading to a lower purity of the captured CO₂ [35].

A comparison of the adsorption enthalpies in Table 1 for IRMOF-8 and IRMOF-8-NO₂ reveals that the enthalpies for hydrogen adsorption on the nitro-functionalized MOF are

higher than those for the pristine MOF at both high and low pressures. The results in Tables 4.2 and 4.3 for CH₄ and CO₂, also show that enthalpies for gas adsorption on IRMOF-8-NO₂ are higher than those for IRMOF-8. The results also show that the enthalpies of adsorption are in the following order: CO₂>CH₄>H₂. This is to be expected since the van der Waals forces of attraction are in this same order. It is also interesting to see that the magnitudes of the sticking factors for these three gases are in the same order as the adsorption enthalpies. Thus it appears that nitro-functionalization strengthens the bonding of the gases to the surface thus resulting in greater sticking efficiency and larger than expected gas adsorption for the functionalized MOF.

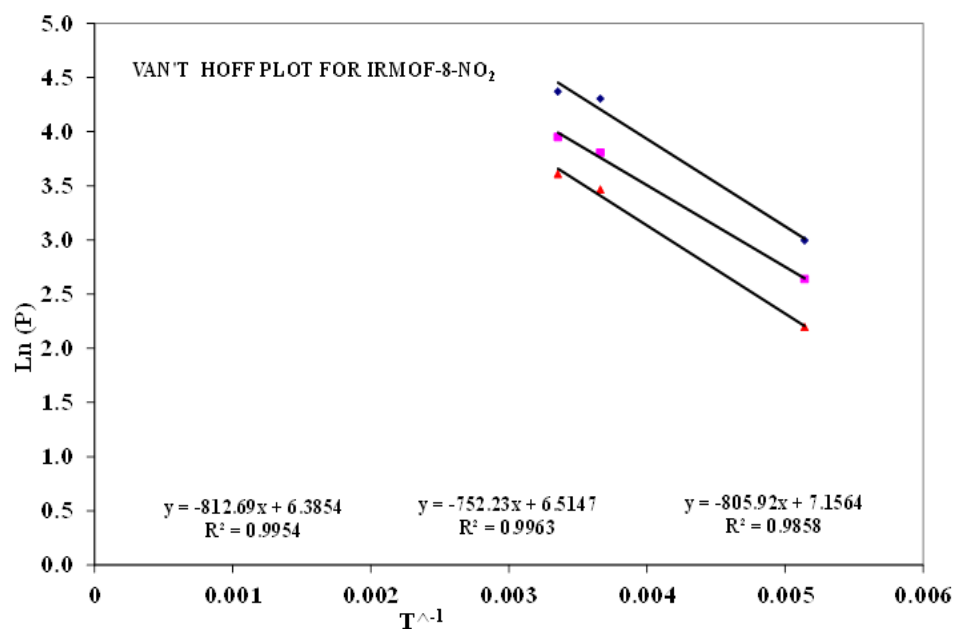


Figure 4.15 Van't Hoff plots for heat of adsorption of IRMOF-8-NO₂ at high pressure

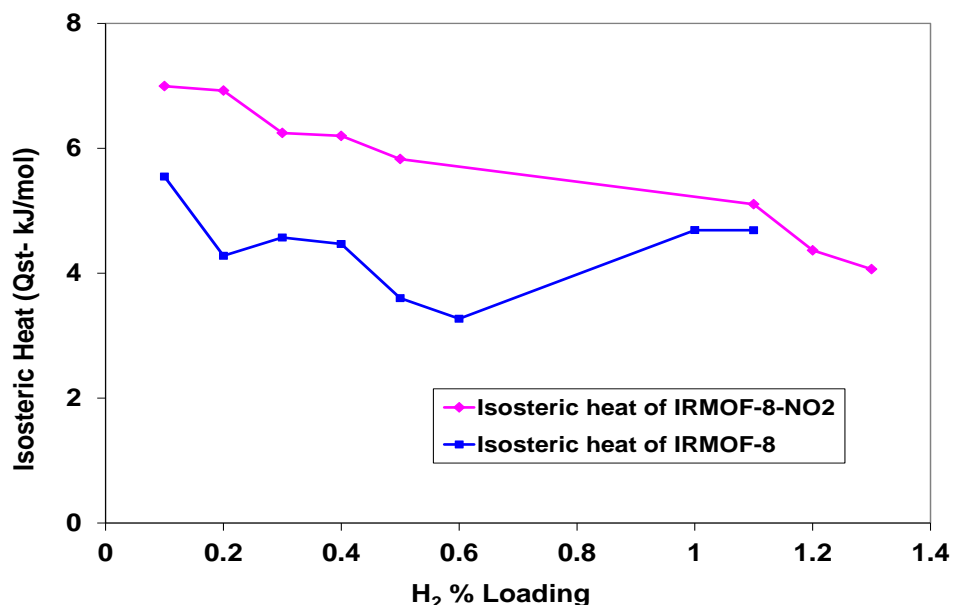


Figure 4.16 Isosteric heat of adsorption of IRMOF-8-NO₂ and pristine IRMOF-8 versus hydrogen loading at high pressure

4.11 CONCLUSION

The results of this research have shown that the nitro-functionalization of IRMOF-8 leads to a reduction in the surface area and a decrease pore volume. It was found that the surface area and pore volume of the IRMOF-8-NO₂ was only about 50% as large as that for the IRMOF-8. This resulted in decreased ability of the IRMOF-8-NO₂ to adsorb H₂, CH₄, and CO₂ gases at various temperatures. However, the decrease is not as great as one would expect based solely on the change in surface area and pore volume. A novel concept called the sticking factor (defined as the percent gas adsorbed per m² of surface area per gram of material) was determined for the adsorption of each gas on the two MOFs at various temperatures. Since the sticking factors for gases adsorbed on the IRMOF-8-NO₂ were greater than those for gas adsorbed on the IRMOF-8, this indicated

that nitro-functionalization of IRMOF-8 increases the sticking efficiency of gases. This increased sticking efficiency can be explained, in part, based on the fact that there was a large increase in the adsorption enthalpies for these gases upon functionalization.

CHAPTER FIVE

5 NANOCONFINEMENT OF NaAlH₄ IN IRMOF-8 (NaAlH₄@IRMOF-8)

Reversible solid state hydrogen storage in metal complex hydrides such as alanates, aminodiboranes, borohydrides and nitrides are promising options for chemical hydrogen storage due to their high storage capacities (5.5-18.5 wt.%). [5, 6, 13, 17, 19, 20, 110-117]. NaAlH₄ is one of the complex hydrides that has shown favorable thermodynamics and high hydrogen storage capacity. However, metal hydrides exhibit too slow kinetics and high thermodynamic stability [118]. Attempts have been made to decrease the hydrogen desorption temperature of NaAlH₄ which is approximately 186 °C. The pioneering works of Bogdanovic and Schwickardi [5, 6] introduced Ti-containing compounds into NaAlH₄ to catalyze the hydrogen absorption and desorption under milder conditions. These attempts have been limited by particle agglomeration, grain growth of the NaAlH₄ upon hydrogen release and uptake cycles at elevated temperatures and also by low maximum reversible storage on multiple cycles at temperatures less than 120 °C. High pressures (>200 bar) and long times are also needed for reloading depleted NaAlH₄. A number of approaches have been investigated for alleviating the problem of thermodynamics and stability such as cation/anion substitution, additives of hydrides of transition metals and size effects [5, 6, 13, 110-118].

Reducing the size of NaAlH₄ to the nanoscale dimension is a potential route to enhance its hydrogen storage capacity. Ball milling and nanoconfinement of metal

hydrides in scaffolds (mesoporous and microporous materials) are two potential techniques for size reduction. However, the positive effects (faster dehydrogenation kinetics and better reversibility than pristine sodium alanate) of ball milling diminish due to the inevitable particle agglomeration driven by high surface energy and the segregation of the Al domain after several cycles. Nanoconfinement either by wet infiltration or thermal melt infiltration on the other hand helps to maintain a stable nanostructure and nanoeffects during cycling by preventing particle agglomeration, grain growth and keeping the grains in close proximity [5, 6]. The stability of NaAlH_4 is the result of charge transfer from the sodium (Na) to the alane (AlH_4). This stability has been shown to be weakened by the introduction of carbon fullerenes or nanotubes which affect the charge transfer from Na to AlH_4 . The Al-H bond becomes weak, the dehydrogenation temperature decreases and the rehydrogenation reaction is enhanced [110, 111].

Several reports have demonstrated the enhanced dehydrogenation and rehydrogenation of the alanates or borohydrides using mesoporous carbon (MC) or other porous materials [5, 6, 13, 17, 19, 20, 110-123]. However, there are just a few reports on the use of MOFs for this purpose [112, 124].

5.1 X-RAY DIFFRACTION OF NaAlH_4 , $\text{NaAlH}_4@$ IRMOF-8 AND $\text{NaAlH}_4@$ MC

Figure 5.1 shows the X-ray diffraction patterns of the bulk NaAlH_4 , IRMOF-8, MC (Fig. 5.1 (a), (b) and (d)) and the nanoconfined NaAlH_4 . The peaks of the bulk NaAlH_4 in Fig. 5.1(a), were not seen after being nanoconfined in $\text{NaAlH}_4@$ IRMOF-8 and $\text{NaAlH}_4@$ MC (Fig. 5.1 c and e). This suggests that the NaAlH_4 has been confined in the

pores of the bulk materials, amorphosized or partly decomposed/too small to be observed [5, 6, 112]. There is however, a decrease in the peak intensities of the scaffolding material. This may be attributed to partial collapse of the framework during the wet infiltration process.

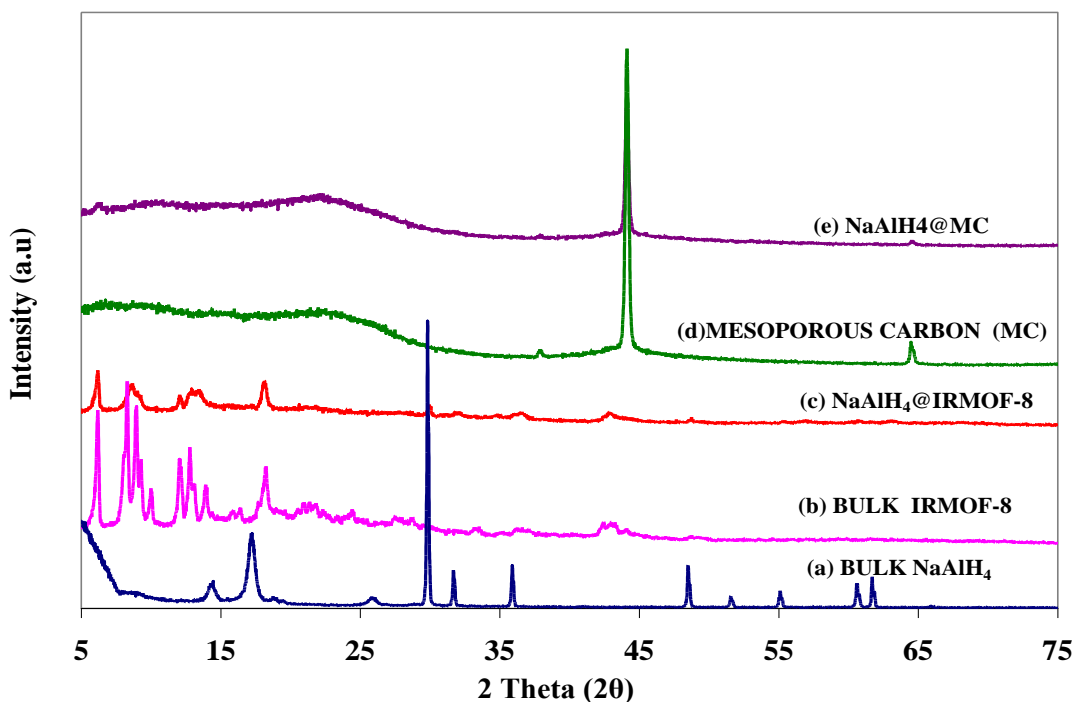


Figure 5.1 X-ray diffraction of bulk NaAlH₄, IRMOF-8, Mesoporous Carbon (a, b, d) and nanoconfined NaAlH₄@IRMOF-8 (c) and NaAlH₄@MC (e)

5.2 TGA ANALYSIS OF BULK AND COMPOSITE MATERIALS

Figure 5.2 shows the TGA-DTA curves of the bulk and nanoconfined materials. It can be observed that the DTA curves of the pristine IRMOF-8 and MC did not show any peaks between 0 and 450 °C. The bulk NaAlH₄ on the other hand showed the characteristic three peaks corresponding to the melting temperature and endothermic

release of H_2 at ~ 180 , 240 and ~ 450 $^{\circ}C$. However, when $NaAlH_4$ was infiltrated into IRMOF-8 and MC, one-step decomposition (H_2 release) reaction was observed. This pattern further confirms the possibility of nanoconfinement and the findings are in agreement with the literature reports of Rude et al.[5], Nielson et al.[6], Fichner [111] and Majzoub [114].

It has also been reported that below a certain particle size (~ 3 nm), a one-step reaction is favored. This is due to the effect of nanoparticle size on the thermodynamics of decomposition with the stabilization of $NaAlH_4$ as the hydrogenated state and $NaH + Al$ as the dehydrogenated state. This results in a suppression of the thermodynamically stable intermediate Na_3AlH_6 [5, 6, 111, 112, 114]. The porous materials used in this study, have pore sizes within this range.

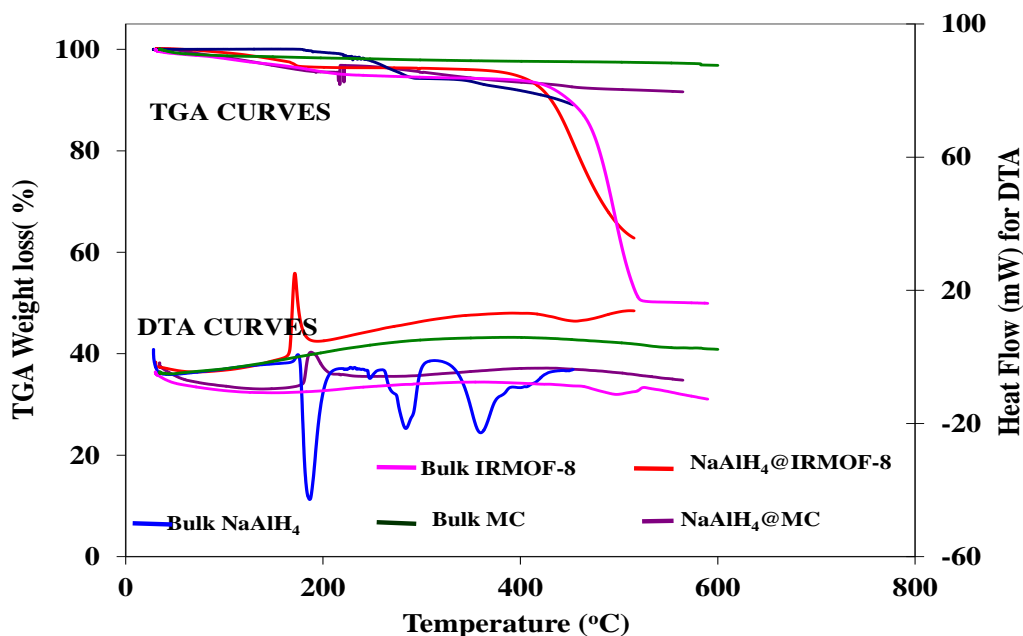


Figure 5.2 TGA-DTA of bulk IRMOF-8, MC and nanoconfined $NaAlH_4$ in IRMOF-8 and MC.

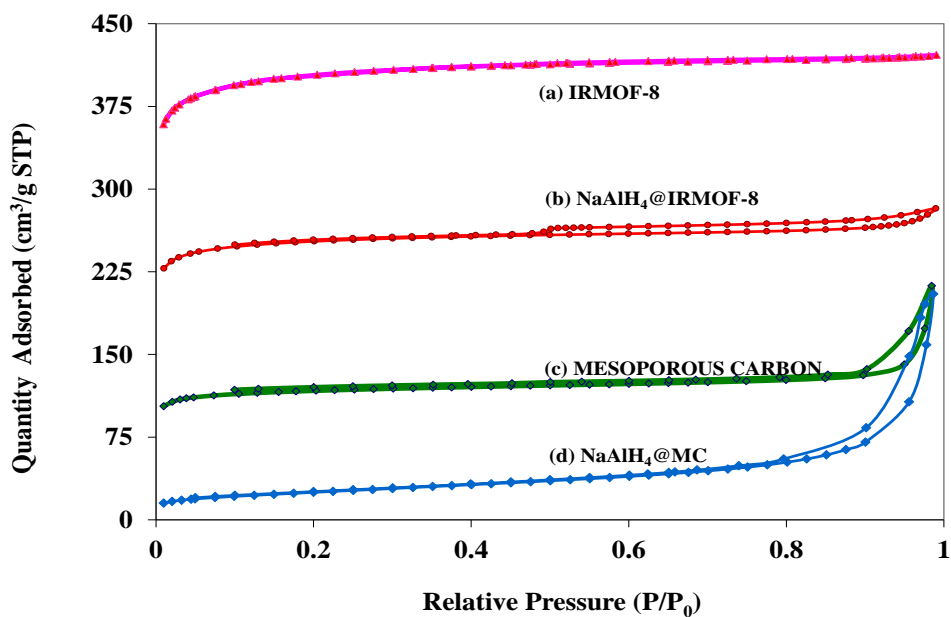
5.3 SURFACE AREA AND POROSITY STUDY OF THE COMPOSITES

The amount of NaAlH_4 infiltrated into the scaffolds was estimated from the surface area and pore volumes of the bulk materials before and after infiltration. The density and the difference in the pore volumes of the pristine materials were used to estimate the loading capacity of the porous materials. Figure 5.3(a)-(d) shows the nitrogen adsorption isotherms of bulk and nanoconfined materials. In Fig. 5.3 (a), the bulk IRMOF-8 had a BET surface area and pore volume of $1529 \text{ m}^2/\text{g}$ and $0.65 \text{ cm}^3/\text{g}$. The pore size was 1.70 nm . After infiltration, evacuation and degasing, the BET surface area, pore volume and pore size were $1005 \text{ m}^2/\text{g}$, 0.40 cm^3 and 1.74 nm respectively as seen in Fig. 5.3 (b). This represents $\sim 39 \%$ infiltration. The NaAlH_4 loading calculated from these data was estimated as 0.25 g NaAlH_4 per gram of sample. The density of IRMOF-8 obtained from literature was 0.45 g/cm^3 , and was used for the above loading calculation [47-48].

In Fig 5.3 (c) and (d), the bulk MC had a BET surface area and pore volume of $196 \text{ m}^2/\text{g}$ and $0.39 \text{ cm}^3/\text{g}$. The pore size was 2.72 nm . After infiltration, evacuation and degasing at $100 \text{ }^\circ\text{C}$ for 3 hours, the BET surface area, pore volume and pore size decreased to $83.0 \text{ m}^2/\text{g}$, 0.30 cm^3 and 2.70 nm respectively as seen in Fig. 5.3 (d). This represents $\sim 23 \%$ infiltration. The NaAlH_4 loading calculated from these data and the density of IRMOF-8 ($\rho = 1.89 \text{ g/cm}^3$) was estimated as $\sim 0.10 \text{ g NaAlH}_4$ per gram of sample. The results are summarized in Table 5.1.

Table 5.1 Physisorption and Thermodynamic Properties of Bulk and Nanoconfined Materials

Materials	NaAlH ₄	Bulk IRMOF-8 and NaAlH ₄ @IRMOF-8	Bulk MC and NaAlH ₄ @MC
Surface Area (m ² /g)			
BET	NA	1529 and 1005	196 and 83.0
Pore Size (nm)	NA	1.70 and 1.74	2.72 and 2.70
Pore Volume (cm ³ /g)	NA	0.65 and 0.40	0.39 and 0.31
Loading (g/g sample)	NA	~ 0.25	~0.10
TPD H ₂ % (T _{onset} = (onset temperature)	5.6 % (~184 °C)	3.3 % (~90 °C)	2.2 % (~114 °C)
RGA T _{onset}	~180 °C	100 °C)	120 °C

Figure 5.3 Nitrogen isotherms of bulk and nanoconfined NaAlH₄ in IRMOF-8 and MC

5.4 TPD ANALYSIS OF BULK AND COMPOSITE MATERIALS

Figure 5.4 (a-c) shows the TPD curves of the bulk NaAlH_4 , NaAlH_4 @IRMOF-8 and NaAlH_4 @MC respectively. The samples released 5.6, 3.3 and 2.2 wt.% H_2 respectively, which is lower than the expected value of 5.6 wt.% H_2 for NaAlH_4 reaction steps I and II in equations 1 and 2 in chapter 1. These results indicate that ~ 58 and 40 % of the added NaAlH_4 is successfully wet-infiltrated into IRMOF-8 and MC, respectively, while the remaining fraction apparently decomposes, forming Al(s) and NaH(s) [6]. The onset dehydrogenation temperatures are also in close agreement with the result from the RGA analysis as seen in section 5.5.

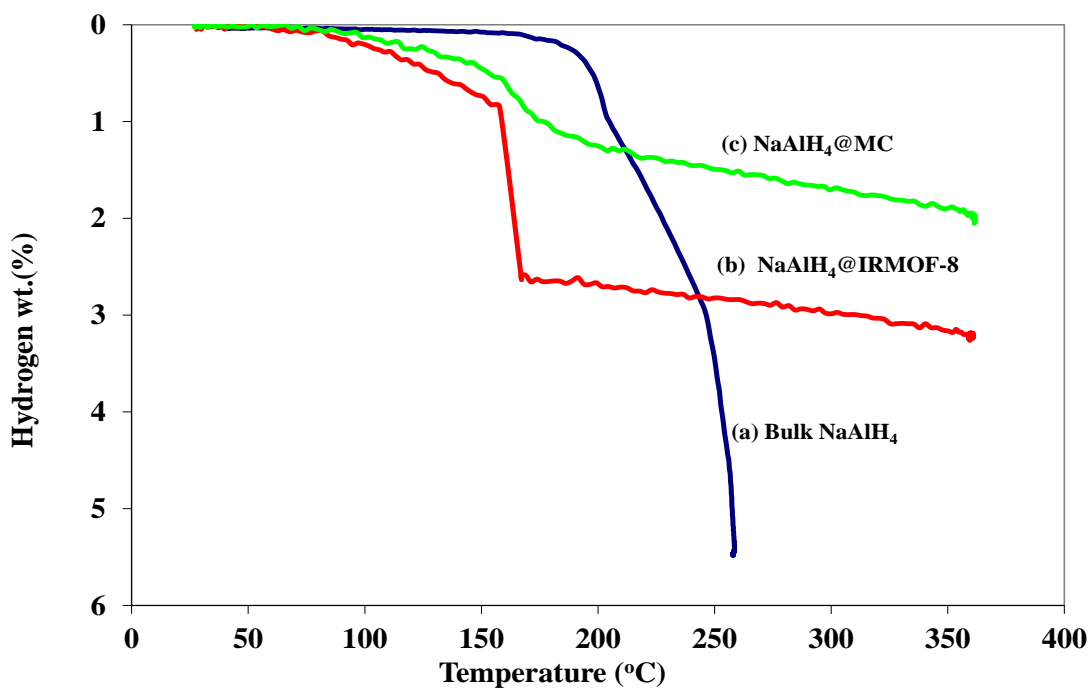


Figure 5.4 TPDs of pristine and nanoconfined NaAlH_4 in IRMOF-8 and MC

5.5 RGA ANALYSIS OF BULK AND COMPOSITE MATERIALS

The residual gas analysis was used to determine the gases evolved from the bulk NaAlH_4 , $\text{NaAlH}_4@IRMOF-8$ and $\text{NaAlH}_4@MC$ in Figures 5.4 (a-c) respectively. The results confirm that the only species given off was hydrogen. Other fragments such as nitrogen, oxygen, formamide, formaldehyde, methane, carbon dioxide were not visible or given off from the sample. The deep in Fig. 5.5a, shows the two-step dehydrogenation pattern observed in bulk NaAlH_4 . This is not seen in the composite. It was observed that the amount of hydrogen given off decreased from the bulk NaAlH_4 to $\text{NaAlH}_4@MC$. In effect, the smaller the pore size and bigger the pore volume, greater is the loading and greater is the amount of H_2 that is released. It was also observed that as the pore size decreases (particle size of NaAlH_4 decrease), the dehydrogenation temperatures decrease as well. The results are summarized in Table 5.1 and they are in close agreement with the TPD results.

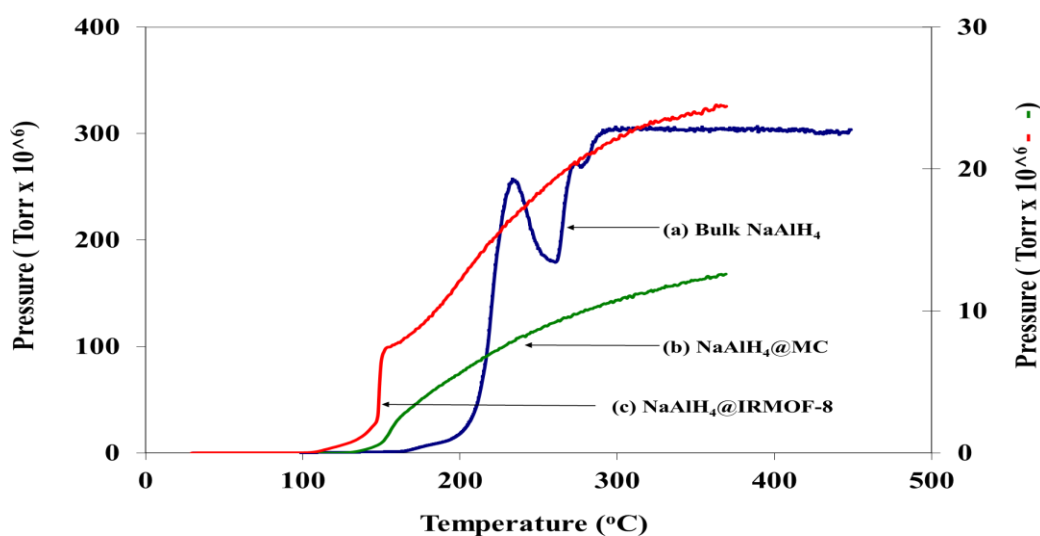


Figure 5.5 RGA of bulk and nanoconfined NaAlH_4 in IRMOF-8 and MC

5.6 CONCLUSION

Nanocomposite NaAlH_4 was prepared by wet infiltration of bulk NaAlH_4 into isorecticular metal-organic framework-eight (IRMOF-8). A mesoporous carbon material was also infiltrated to show the effect of pore size on the thermodynamic properties of nanoconfined sodium alanate. X-ray diffraction patterns of the composite did not show any peak(s) of the bulk NaAlH_4 , indicating that the NaAlH_4 was nanoconfined within the pores of the porous materials. The BET pore volume of NaAlH_4 @IRMOF-8 and NaAlH_4 @MC showed a 39% and 23 % infiltration. The TGA-DTA analysis of the composite revealed a one-step decomposition reaction of the bulk alanate. The residual gas analysis (RGA) of the composite showed the release of hydrogen at a temperature of 100 °C which is also much lower than bulk NaAlH_4 . These TPD results indicate that ~58 and 40 % of the added NaAlH_4 is successfully wet-infiltrated into IRMOF-8 and MC, respectively.

CHAPTER SIX

6 SUMMARY OF THE RESEARCH

This research focuses on the gas adsorption properties of IRMOF-8. However, due to the lack of rapid and inexpensive methods of synthesizing MOFs for industrial and practical application, chapter three of this research work was aimed at developing a new method for the synthesis of the metal-organic framework. The gas adsorption properties and methods of increasing or enhancing the gas storage capacity were investigated in chapters four and five. The results are summarized below.

In chapter three, the aim of this research was to develop a rapid inexpensive method for producing high quality IRMOF-8 (isoreticular metal–organic framework) crystals by a solvothermal method. IRMOF-8 crystals could be produced in 2–4 h, which is a significant improvement over traditional solvothermal convective oven syntheses or other methods that takes a day(s) to weeks. The effect of temperature on the pore volume, pore size, surface area and hydrogen storage capacity of convective oven synthesized IRMOF-8 (C-IRMOF-8) and the rapid solvothermal synthesized IRMOF-8 (RS-IRMOF-8) was also investigated. The optimum synthesis temperatures were 120 °C and 155 °C for C-IRMOF-8 and RS-IRMOF-8, respectively. BET analysis showed that the C-IRMOF-8 and RS-IRMOF-8 samples had pore volumes of 0.603 cm³/g STP and 0.693 cm³/g STP with Langmuir SSA of 1694 and 1801 m²/g, respectively at the optimum temperatures. The products of this rapid synthesis route had greater surface areas and

comparable hydrogen storage capacities to those prepared by traditional solvothermal convective oven syntheses.

Several methods have been suggested to increase the binding energy of gas molecules to the surface of MOFs. Pre or post-syntheses functionalization of MOFs is a positive step in the direction of increasing the gas binding energy or capacity. Chapter four deals with the effects of nitro-functionalization on the gas sorption properties of IRMOF-8. BET isotherm analysis showed that nitro-functionalization of IRMOF-8 caused the surface area to decrease from 1599 to 832 m²/g while the pore volume decreased from 0.639 to 0.322 m³/g. However, these large decreases in surface area and pore volume did not result in a proportionate decrease in gas sorption capability. For example, the IRMOF-8 adsorbed 3.2 wt% hydrogen while IRMOF-8-NO₂ adsorbed 2.2 wt% hydrogen. This is a relatively small reduction in hydrogen adsorption (~30%) compared to the large decrease in surface areas (~50%). The amounts of methane and carbon dioxide adsorbed by the IRMOF-8-NO₂ were also disproportionately high. A sticking factor was determined for the adsorption of each gas on the two MOFs at various temperatures. In all cases, the sticking factors for gases adsorbed on the IRMOF-8-NO₂ were greater than those for gas adsorbed on the IRMOF-8. Enthalpies were also measured for the adsorption of each gas on the two MOFs at various temperatures. It was found that, in all cases, the enthalpies for gas adsorption on IRMOF-8-NO₂ were greater than those for IRMOF-8. Thus it appears that nitro-functionalization strengthens the bonding of the gases to the surface thus resulting in greater sticking efficiency and larger than expected gas adsorption.

Finally, complex hydrides such as NaAlH_4 are good hydrogen storage materials. However, poor reversibility, kinetics and thermodynamics are major problems. In chapter five, the nanoeffects of IRMOF-8 on NaAlH_4 were studied. The results showed that NaAlH_4 was able to be nanoconfined in IRMOF-8. TGA-DTA analysis confirmed the one-step dehydrogenation pattern that is characteristic of nanoconfinement and the presence of NaAlH_4 . The BET analysis showed that the amount and percent loading were 0.25 g NaAlH_4 per gram of IRMOF-8. This represents ~ 39 % infiltration of the pore volume which was higher than ~ 23 % infiltration of MC ~ 0.10 g NaAlH_4 per gram of MC. TPD curves of the bulk NaAlH_4 , NaAlH_4 @IRMOF-8 and NaAlH_4 @MC showed that 5.6, 3.3 and 2.2 wt.% H_2 was released respectively, These results indicate that ~58 and 40 % of the added NaAlH_4 is successfully wet-infiltrated into IRMOF-8 and MC, respectively. Both TPD and RGA analysis revealed that the onset desorption temperature of bulk sodium alanate was reduced by ~90 and ~60 °C in NaAlH_4 @IRMOF-8 and NaAlH_4 @MC respectively. Therefore the bigger the pore volume the more the infiltration and the smaller the particle and pore size the lower the dehydrogenation temperature.

6.1 FUTURE RESEARCH RECOMMENDATION

- Develop or use new activation methods after the synthesis of the MOFs studied that can improve their surface areas.

- Develop an optimum synthesis condition for IRMOF-8-NO₂ and incorporation of other functional groups that will not only increase the binding energy but also increase the internal surface area and the pore volume.
- Studies have shown that IRMOF-8 has no unsaturated metal centers (UMCs). Transitional metal should be incorporated into the synthesis of IRMOF-8 to increase its binding capacity.
- Further study on nanoconfinement of NaAlH₄ should be carried out. Such as melt infiltration method.

REFERENCES

1. Jena, P. Materials for Hydrogen Storage: Past, Present, and Future. *J. Phy. Chem. Letts.* **2011**, 2, 206–211.
2. Murray, L. J.; Dinca, M.; Long, J. R. Hydrogen storage in metal-organic frameworks. *Chem. Soc. Rev.* **2009**, 38, 1294-1314.
3. Han, S. S.; Mendosa-Cortes J. L.; Goddard III, W. A. Recent advances on simulation and theory of hydrogen storage in metal-organic frameworks. *Chem. Soc. Rev.* **2009**, 38, 1460-1476.
4. Zhao, D.; Yuan D.; Zhou, H.C. The current status of hydrogen in metal-organic frameworks. *Energy Environ. Sci.* **2008**, 1, 222-235.
5. Rude1, L.H.; Nielsen, T. K.; Ravnsbæk, D. B.; Bosenberg, U.; Ley, M. B.; Richter, B.; Arnbjerg, L. M.; Dornheim, M.; Filinchuk, Y.; Besenbacher, F.; Jensen, T. R. Tailoring properties of borohydrides for hydrogen storage: A review. *Phys. Status Solid A.* **2001**, 208 (8), 1754-1773.
6. Nielsen, T. K.; Polanski, M.; Zasada, D.; Javadian, P.; Bystryzycki, J.; Skibsted, J.; Besenbacher, F.; Jensen, T. R. Improved Hydrogen Storage Kinetics of Nanoconfined NaAlH₄ Catalyzed with TiCl₃ Nanoparticles. *ACS NANO.* **2011**, 5(5), 4056-4064.
7. Saha, D.; Wei, Z.; Deng, S. Equilibrium, kinetics and enthalpy of hydrogen adsorption in MOF-177. *Int. J. Hydrogen Energy.* **2008**, 33, 7479-7488.
8. Schhmitz, B.; Muller, U.; Trukhan, N.; Schubert, M.; Ferey G.; Hirscher, M. Heat of adsorption for hydrogen in microporous high-surface-area materials *ChemPhysChem.*, **2008**, 9, 2181-2184.
9. Figueroa, J. D.; Fout, T.; Plasynski, S.; McIlvried, H.; Srivastava, R. D. Advances in CO₂ capture technology-The U.S. department of energy's carbon sequestration Program. *Int. J. Greenhouse Gas Control.* **2008**, 2, 9-20.
10. Hirscher, M.; Panella, B.; Schmitz, B. Metal-organic frameworks for hydrogen storage. *Micropor. Mesopor. Mater.* **2010**, 129, 335-339.

11. Llewellyn, P. L.; Bourrelly, S.; Serre, C.; Vimont, A.; Daturi, M.; Hamon, L.; Weireld, G. D.; Chang, J. S.; Hong, D. Y.; Huang, Y. K.; Jung, S. H.; Ferey, G. High uptakes of CO₂ and CH₄ in mesoporous metal-organic frameworks MIL-100 and MIL-101. *Langmuir*. **2008**, 24, 7245-7250.
12. Kuppler, R. J.; Timmons, D. J.; Fang, Q.-R.; Li, J.-R.; Makal, T. A.; Young, M. D.; Yuan, D.; Zhao, D.; Zhuang W.; Zhou, H. C. Potential applications of metal-organic frameworks. *Coordination Chem. Rev.* **2009**, 253, 3042-3066.
13. Satyapal, S.; Petrovic, J.; Read, C.; Thomas, G.; Ordaz, G. The U.S. department of energy's national hydrogen storage project: Progress towards meeting hydrogen-powered vehicle requirements. *Catalysis Today*. **2007**, 120, 246-256.
14. Ma, S.; Zhou, H. C. *Chem. Commun.*, Gas storage in porous metal-organic frameworks for clean energy applications. **2010**, 46, 44-53.
15. Orefuwa, S. A. Effects of dopants on the hydrogen storage properties of calcium alanate and infrared study of some selected alanates. DSU, *M.Sc. Thesis*, **2008**,
16. Getman, R. B.; Bae, Y.S.; Wilmer C. E.; Snurr, R. Q. Review and analysis of molecular simulations of methane, hydrogen, and acetylene storage in metal-organic frameworks. *Chem. Rev.*, **2012**, 112, 703-723.
17. McWhorter, S.; Read, C.; Ordaz, G.; Stetson, N. Materials-based hydrogen storage: Attributes for near-term, early market PEM fuel cells. **2011**, 15, 29-38.
18. Suh, M. P.; Park, H. J.; Prasad T. K.; Lim, D. W. Hydrogen storage in metal-organic frameworks. *Chem. Rev.*, **2012**, 112, 782-835.
19. Zuttel, A. Hydrogen storage methods. *Naturewissenschaften*. **2004**, 91, 157-172.
20. Sahaym, U.; Norton, M. G. Advances in the application of nanotechnology in enabling a 'hydrogen economy'. *J. Mater. Sci.* **2008**, 43(66), 5395-5429.
21. Sculley, J.; Yuan, D.; Zhou, H.C. The current status of hydrogen storage in metal-organic frameworks—updated. *Energy Environ. Sci.* **2011**, 4, 2721-2735.
22. Saha, D.; Wei, Z.; Deng, S. Hydrogen adsorption equilibrium and kinetics in metal-organic framework (MOF-5) synthesized with DEF approach. *Separation Purification Tech.* **2009**, 64, 280-287.
23. Moellmer, J.; Celer, E.B.; Luebke, R.; Cairns, A.J.; Staudt, R.; Eddaoudi, M.; Thommes, M. Insights on adsorption characterization of metal-organic frameworks: A benchmark study on the novel soc-MOF. *Micropor. Mesopor. Mater.* **2010**, 129, 345-353.

24. Choi, J.S.; Son, Kim, J.; Ahn, W.S. Metal–organic framework MOF-5 prepared by microwave heating: Factors to be considered. *Micropor. Mesopor. Mater.* **2008**, 116, 727-731.
25. Lia, J.; Chengb, S.; Zhaoa, Q.; Longa, P.; Dong, J. Synthesis and hydrogen-storage behavior of metal–organic framework MOF-5. *Int. J. Hydrogen Energy.* **2009**, 34, 1377-1382.
26. Purewal, J.J.; Liu, D.; Yang, J.; Sudik, A.; Siegel, D.J.; Maurer, S.; Muller U. Increased volumetric hydrogen uptake of MOF-5 by powder densification. *Int. J. Hydrogen Energy.* **2012**, 37, 2723-2727.
27. Dietzel, P. D. C.; Besikiotis V.; Blom, R. Application of metal–organic frameworks with coordinatively unsaturated metal sites in storage and separation of methane and carbon dioxide. *J. Mater. Chem.* **2009**, 19, 7362-7370.
28. Lin, X.; Jia, J.; Hubberstey, P.; Schroder, M.; Champness, M. R. Hydrogen storage in metal-organic frameworks. *CrystEngComm.* **2007**, 9, 438-448.
29. Cohen, S. M. Postsynthetic methods for the functionalization of metal-organic frameworks. *Chem. Rev.* **2012**, 112 (2), 970-1000.
30. Stock, N.; Biswas, S. Synthesis of metal-organic frameworks (MOFs): Routes to various MOF topologies, morphologies, and composites. *Chem. Rev.* **2012**, 112(2), 933-969.
31. Fanga, Q. R.; Makala, T. A.; Young, M. D.; Zhou, H. C. Recent advances in the study of mesoporous metal-organic frameworks. *Comm. Inorg. Chem.* **2010**, 31, 165-195.
32. Yang, H.; Orefuwa, S.; Goudy A. Study of mechanochemical synthesis in the formation of the metal-organic framework Cu₃(BTC)₂ for hydrogen storage. *Micropor. Mesopor. Mater.* **2011**, 143, 37-45.
33. Isaeva, V. I.; Kusatov, L. M. Metal-organic frameworks-New materials for hydrogen storage. *Russian J. Gen. Chem.* **2007**, 77, 721-739.
34. Li, J-R.; Sculley J.; Zhou, H. C. Metal-organic frameworks for separations. *Chem. Rev.* **2012**, 112, 869-932.
35. Sumida, K.; Rogow, D.L.; Mason, J. A.; McDonald, T. M.; Bloch, E. D.; Herm, Z. R.; Bae T. H.; Long, J. R. Carbon dioxide capture in metal-organic frameworks. *Chem. Rev.* **2012**, 112, 724–781.

36. Orefuwa, S. A.; Yang H.; Goudy, A. J. Rapid solvothermal synthesis of an isostructural metal-organic framework with permanent porosity for hydrogen storage. *Micropor. Mesopor. Mater.* **2012**, 153, 38-93.
37. Panella, B. Hydrogen storage by physisorption on porous materials. Max-Planck-Institut für Metallforschung, Stuttgart. Ph.D dissertation. **2006**.
38. Rowsell, J. L .C.; Yaghi, O.M. Strategies for hydrogen storage in metal-organic frameworks. *Angew. Chem. Int. Ed.* **2005**, 44, 4670–4679.
39. Rowsell, J. L .C; Yaghi, O.M. Metal–organic frameworks: a new class of porous materials. *Micropor. Mesopor. Mater.* **2004**, 73, 3-14.
40. Li, J. R.; Ma, Y.; McCarthy, M. C.; Sculley, J.; Yub, J.; Jeong, H. K.; Balbuenab, P. B.; Zhou, H.C. Carbon dioxide capture-related gas adsorption and separation in metal-organic frameworks. *Coordination Chem. Rev.* **2011**, 255, 1791-1823.
41. Dinca, M.; Dailly, A.; Liu, Y.; Brown, C. M.; Neumann, D. A.; Long, J. R. Hydrogen storage in a microporous metal-organic framework with exposed Mn²⁺ coordination sites. *J. Am. Chem. Soc.* **2006**, 128, 16876-16883.
42. Sun, D.; Ma, S.; Ke, Y.; Collins, D. J.; Zhou, H. C. An interweaving MOF with high hydrogen uptake. *J. Am. Chem. Soc.* **2006**, 128, 3896-3897.
43. Tanabe, K. K.; Wang, Z.; Cohen, S. M. Systematic functionalization of a metal-organic framework via a postsynthetic modification approach *J. Am. Chem. Soc.* **2008**, 130, 8508-8517.
44. Sun, L. B.; Lin, J. R.; Park J.; Zhou, H. C. Cooperative template-directed assembly of mesoporous metal-organic frameworks. *J. Am. Chem. Soc.* **2012**, 134, 126-129.
45. Cao, W.; Li, Y.; Wang, L.; Liao, S. Effects of metal ions and ligand functionalization on hydrogen storage in metal-organic frameworks by spillover. *J. Phys. Chem. C.* **2011**, 115, 13829-13836.
46. Deng, H.; Doonan, C. J.; Furukawa, H.; Ferreira, R. B.; Towne, J.; Knobler, C. B.; Wang, B.; Yaghi, O. M. Multiple functional groups of varying ratios in metal-organic frameworks. *Science.* **2010**, 327, 846-850.
47. Eddaoudi, M.; Kim, J.; Rosi, N.; Vodak, D.; Wachter, J.; O'Keeffe, M.; Yaghi, O. M. *Science*, **2002**, 295, 469-472.
48. Roswell, J. L. C.; Yaghi, O. M. Effects of functionalization, catenation, and variation of the metal oxide and organic linking units on the low-pressure hydrogen

- adsorption properties of metal-organic frameworks. *J. Am. Chem. Soc.* **2006**, 128, 1304-1315.
49. Lin, X.; Jia, J.; Champness, N.R.; Hubberstey, P.; Schroder, M. Solid-state hydrogen storage, materials and chemistry. *Woodland publishing in materials.* **2008**, 228-312.
 50. Walton, K. S.; Snurr, R. Q. Applicability of the BET method for determining surface areas of microporous metal-organic frameworks. *J. Am. Chem. Soc.* **2007**, 129, 8552-8556.
 51. Webb, P. A.; Orr, C. Analytical methods in fine particles technology. *Micromeritics instrument corporation, Norcross, GA.* **1997**, 45-65.
 52. Sing, K. The use of nitrogen adsorption for the characterization of porous materials. *Colloids and Surfaces.* **2001**, 187, 3-9.
 53. Zhong, D. C.; Lin, J. B.; Lu, W. G.; Jiang, L.; Lu, T. B. Strong hydrogen binding within a 3D microporous metal-organic framework. *Inorg. Chem.* 48, 2009, 8656-8658.
 54. Min, D.; Yoon, S. S.; Lee, C.; Lee, C. Y. Suh, .; M.; Hwang, Y.J.; Han, W. S.; Lee, S. W. A zinc (II)-carboxylate coordination polymer constructed from zinc nitrate and 2, 6-naphthalenedicarboxylate. *Bull. Korean Chem. Soc.* **2001**, 22, 531-533.
 55. Nicholson, D. M. Interaction of the explosive molecules RDX and TATP with IRMOF-8. *J. Phys. Chem. C.* **2010**, 114, 7535-7540.
 56. Li, Y.; Yang, R. T. Hydrogen storage in metal-organic frameworks by bridged hydrogen spillover. *J. Am. Chem. Soc.* **2006**, 128, 8136-8137.
 57. (a) Roswell, J. L. C.; Millward, A. R.; Park, K. S.; Yaghi, O. M. *J. Am. Chem. Soc.* **2004**, 126, 5666-5667.
(b) Roswell, J. L. C.; Millward, A. R.; Park, K. S.; Yaghi, O. M. *J. Am. Chem. Soc.* **2004**, 126, 1-4.
 58. (a) Li, Y.; Yang, R.T. Significantly enhanced hydrogen storage in metal-organic frameworks via spillover. *J. Am. Chem. Soc.* **2006**, 128, 726-727.
(b) Li, Y.; Yang, R.T. Significantly enhanced hydrogen storage in metal-organic frameworks via spillover. *J. Am. Chem. Soc.* **2006**, 128, 1-7.
 59. Dailly, A.; Vajo J.J.; Ahn, C.C. Saturation of hydrogen sorption in Zn benzenedicarboxylate and Zn naphthalenedicarboxylate. *J. Phy. Chem. B.* **2006**, 110 1099-1101.

60. Siberio-Pe´rez, D. Y.; Wong-Foy, A.G.; Yaghi, O. M.; Metzger, A. J. Raman spectroscopic investigation of CH₄ and N₂ adsorption in metal-organic frameworks. *Chem. Mater.* **19**, **2007**, 3681-3685.
61. Keskin, S.; Sholl, D. S. Efficient methods for screening of metal organic framework membranes for gas separations using atomically detailed models. *Langmuir*. **2009**, **25**, 11786-11795.
62. Yao, Q.; Su, J.; Cheung, O.; Liu, Q.; Hedin, N.; Zou, X. Interpenetrated metal-organic frameworks and their uptake of CO₂ at relatively low pressures. *J. Mater. Chem.*, **2012**, **22**, 10345-10351.
63. Wang, L.; Stuckert, N. R.; Chen, H.; Yang, R. T. Effects of Pt. size on hydrogen storage on Pt-doped metal-organic framework IRMOF-8. *Phys. Chem. C*, **2011**, **115**, 4793-4799.
64. Greathouse, J. A.; Ockwig, N. W.; Criscenti, L. J.; Guilinger, T.R.; Pohl, P.; Allendorf, M. D. Computational screening of metal-organic frameworks for large-molecule chemical sensing. *Phys. Chem. Chem. Phys.* **2010**, **12**, 12621-12629.
65. Yang, Q.; Zhong, C.; Chen, J. F. Computational study of CO₂ in metal-organic frameworks. *J. Phys. Chem. C*. **2008**, **112**, 1562-1569.
66. Yang, Q.; Ma, L.; Zhong, C.; An, X.; Liu, D. Enhancement of CO₂/N₂ mixture separation using the thermodynamic stepped behavior of adsorption in metal-organic frameworks. *J. Phy. Chem. C*. **2011**, **115**, 2790-2797.
67. Frost, H.; Duren, T.; Snurr, R. Q. Effects of surface area, free volume, and heat of adsorption on hydrogen uptake in metal-organic frameworks. *J. Phy. Chem. C*. **2006**, **110**, 9565-9570.
68. Hicks, J. M.; Desgranges, C.; Delhommelle, J. Characterization and comparison of the performance of IRMOF-1, IRMOF-8, and IRMOF-10 for CO₂ adsorption in the subcritical and supercritical regimes. *J. Phy. Chem. C*. **2012**, **116**, 22938-22946.
69. (a) Tsao, C.-S.; Yu, M.-S.; Wang, C.-Y.; Liao, P.-Y.; Chen, H.-L.; Jeng, U.-S.; Tzeng, Y.-R.; Chung, T.-Y.; Wu, H. Nanostructure and hydrogen spillover of bridged metal-organic frameworks. *J. Am. Chem. Soc.* **2009**, **131**, 1404-1406.
(b) Tsao, C.-S.; Yu, M.-S.; Wang, C.-Y.; Liao, P.-Y.; Chen, H.-L.; Jeng, U.-S.; Tzeng, Y.-R.; Chung, T.-Y.; Wu, H. Nanostructure and hydrogen spillover of bridged metal-organic frameworks. *J. Am. Chem. Soc.* **2009**, **131**, S1-S5.

70. Kaye, S.S.; Dailly, A.; Yaghi, O. M.; Long, J.R. Impact of preparation and handling on the hydrogen storage properties of ZnO(1,4-benzenedicarboxylate) (MOF-5). *J. Am. Chem. Soc.* **2007**, 129 (46), 14176-14177.
71. Bae, Y.-S.; Dubbeldam, D.; Nelson, A.; Walton, K. S.; Hupp, J. T.; Snurr, R. Q. Strategies for characterization of large-pore metal-organic frameworks by combined experimental and computational methods. *Chem. Mater.* **2009**, 21, 4768-4777.
72. Khan, N. A.; Jung, S. H. Facile synthesis of metal-organic framework $\text{Cu}_3(\text{BTC})_2(\text{H}_2\text{O})_3$ under ultrasound. *Bull. Korean Chem. Soc.* **2009**, 30, 2921-2926.
73. Son, W.-J.; Kim, J.; Kim, J.; Ahn, W.-S. Sonochemical synthesis of MOF-5. *Chem. Commun.* **2008**, 6336-6338.
(b) Son, W.-J.; Kim, J.; Kim, J.; Ahn, W.-S. Sonochemical synthesis of MOF-5. *Chem. Commun.* **2008**, S1-S7.
74. Jung, D.-W.; Yang, D.-A.; Kim, J.; Kim, J.; Ahn, W.-S. Facile synthesis of MOF-177 by sonochemical method using 1-methyl-2-pyrrolidinone as a solvent. *Dalton Trans.* **2009**, 39, 2883-2887.
75. Carson, C. G.; Hardcastle, K.; Schwartz, J.; Liu, X.; Hoffmann, C.; Gerhardt, R.A.; Tannenbaum, R. Synthesis and structure characterization of copper terephthalate metal-organic frameworks. *Eur. J. Inorg. Chem.* **2009**, 2338-2343.
76. Ni, Z.; Masel, R.I. Rapid production of metal-organic frameworks via microwave assisted solvothermal synthesis. *J. Am. Chem. Soc.* **2006**, 128, 12394-12395.
77. DeFusco A.T.; Arnold. A.T. *Patent* 4531013, 1985, downloaded July 2012. <http://www.surechem.org/index.php?Action=document&docId=642474&db=USPTO>
78. Mamatha, M.; Bogdanovic, B.; Felderhoff, M.; Pommerin, A.; Schmidt, W.; Schuth, F.; Weidenthaler, C. Mechanochemical preparation and investigation of properties of magnesium, calcium and lithium-magnesium alanates. *J. Alloys. Comp.* **2006**, 407, 78-86.
79. ChemDraw[®]Ultra8.0, **2003**, Chemical Structure Drawing Standard. CambridgeSoft.
80. Yaghi, O.M.; Arbor, A.; Eddaoudi, M.; Li, H.; Kim, J.; Rosi, N. Isoreticular metal-organic frameworks, process for forming the same and systematic design of pore size and functionality therein, with application for gas storage. *U.S Patent Application* 2003/0004364 A1, **2003**, 1-57.

81. Matzger, A.J. Solvothermal synthesis of metal-organic frameworks. Final scientific and technical report. **2008**.
82. Calleja, G.; Botas, J.A.; Orcajo, M.G.; Sánchez-Sánchez, M. Differences between the isostructural IRMOF-1 and MOCP-L porous adsorbents. *J. Porous Mater.* **2010**, *17*, 91-97.
83. Li, Y.; Yang, R.T. Gas adsorption and storage in metal-organic framework MOF-177. *Langmuir.* **2007**, *23*, 12937-12944.
84. Choi, J.Y.; Kim, J.; Jung, S.H.; Kim, H.K.; Chang, J.-S.; Chae, H. K. Microwave synthesis of a porous metal-organic framework, zinc terephthalate MOF-5. *Bull. Korean Chem. Soc.* **2006**, *27*, 1523-1524.
85. Tranchemontagne, D.J.; Hunt, J.R.; Yaghi, O.M. Room temperature synthesis of metal-organic frameworks: MOF-5, MOF-74, MOF-177, MOF-199, and IRMOF-0 *Tetrahedron.* **2008**, *64*, 8553-8557.
86. Torrisi, A.; Bell, R.G.; Draznieks, C.M. Functionalized MOFs for enhanced CO₂ capture. *Cryst. Growth Des.* **2010**, *10*, 2839-2841.
87. Arstad, B.; Fjellvag, H.; Kongshuang, K.O.; Swang, O.; Blom, R. Amine functionalized metal-organic frameworks (MOFs) as adsorbent for carbon dioxide. *Adsorption.* **2008**, *14*, 755-762.
88. Duren, T.; Bae, Y.-S.; Snurr, R.Q. Using molecular simulation to characterize metal-organic frameworks for adsorption applications. *Chem. Soc. Rev.* **2009**, *38*, 1237-1247.
89. Shao, X.; Wang, W. Adsorption of hydrogen and methane on mesocarbon microbeads by experiment and molecular simulation. *J. Phys. Chem. C.* **2004**, *108*, 2970-2978.
90. Duren, T.; Sarkisov, L.; Yaghi, O. M.; Snurr, R.Q. Design of new materials for methane storage. *Langmuir.* **2004**, *20*, 2683-2689.
91. Walton, K.S.; Millward, A.R.; Dubbeldam, D.; Frost, H.; Low, J. J.; Yaghi O.M.; Snurr, R.Q. *J. Am. Chem. Soc.*, **2008**, *130*, 406-407.
92. Millward, A.R.; Yaghi, O.M. Metal-organic frameworks with exceptional high capacity for storage of carbon dioxide at room temperature. *J. Am. Chem. Soc.* **2005**, *127* (51), 17998-17999.

93. Thallapally, P.K.; Tian, J.; Kishan, M.R.; Fernandez, C.A.; Dalgarno, S.J.; McGrail, P.B.; Warren, J.E.; Atwood, J.L. Flexible (breathing) interpenetrated metal-organic frameworks for CO₂ separation applications. *J. Am. Chem. Soc.* **2008**, 130, 16842-16843.
94. Coudert, F.X.; Boutine, A.; Jeffroy, M.; Mellot-Drazniewski, C.; Fuchs, A.H. Thermodynamic methods and models to study flexible metal-organic frameworks. *ChemPhysChem.* **2011**, 12, 247-258.
95. Wood, C.D.; Tan, B.; Trewin, A.; Su, F.; Rosseinsky, M.J.; Bradshaw, D.; Sun, Y.; Zhou, L.; Cooper, A.I. Microporous organic polymer for methane storage. *Adv. Mater.* **2008**, 20, 1916-1921.
96. Britt, D.; Tranchemontagne, D.; Yaghi, O.M. Metal-organic frameworks with high capacity and selectivity for harmful gases. *PNAS.* **2008**, 105(33), 11623-11627.
97. Huang, L.; Wang, H.; Chen, J.; Wang, Z.; Sun, J.; Zhao, D.; Yan, Y. Synthesis, morphology control, and properties of porous metal-organic coordination polymers. *Micropor. Mesopor Mater.* **2003**, 58, 105-114.
98. Saha, D.; Deng, S.; Yang, Z. Hydrogen adsorption on metal-organic framework (MOF-5) synthesized by DMF approach. *J. Porous Mater.* **2009**, 16, 141-149.
99. Custelcean, R.; Gorbunova, M.G. A metal-organic framework functionalized with free carboxylic acid sites and its selective binding of a Cl(H₂O)⁴⁺ cluster. *J. Am. Chem. Soc.* **2005**, 127, 16362-16363.
100. Ma, S.; Fillinger, J.A.; Ambrogio, M.W.; Zuo, J.-L.; Zhou, H.C. Synthesis and characterization of magnesium metal-organic framework with distorted (10,3)-a-net topology. *Inorg. Chem. Comm.* **2007**, 10, 220-222.
101. Tsao, C.-S.; Yu, M.-S.; Chung, T.-Y.; Wu, H.-C.; Wang, C.-Y.; Chang, K.-S.; Chen, H.-L. Characterization of pore structure in metal-organic framework by small-angle x-ray scattering. *J. Am. Chem. Soc.* **2007**, 129, 15997-16004.
102. Hafizovic, J.; Bjørgen, M.; Olsbye, U.; Dietzel, P. D. C.; Bordiga, S.; Prestipino, C.; Lamberti, C.; Lillerud, K.P.; The inconsistency in adsorption properties and powder XRD data of MOF-5 is rationalized by framework interpenetration and the presence of organic and inorganic species in the nanocavities. *J. Am. Chem. Soc.* **2007**, 129, 3612-3620.
103. Ma, S.; Eckert, J.; Forster, P.M.; Yoon, J. W.; Hwang, Y. K.; Chang, J.-S.; Collier, C. D.; Parise, J.B.; Zhou, H.-C. Further investigation of the effect of framework

- catenation on hydrogen uptake in metal-organic frameworks. *J. Am. Chem. Soc.* **2008**, 130, 15896-15902.
104. Botas, J.A.; Calleja, G.; Sánchez-Sánchez, M.; Orcajo, M.G. Cobalt doping of the MOF-5 framework and its effect on gas-adsorption properties. *Langmuir*. **2010**, 26(8), 5300-5303.
105. Chen, L.; Grajciar, L.; Nachtigall, P.; Duren, T. Accurate prediction of methane adsorption in a metal-organic framework with unsaturated metal sites by direct implementation of an ab initio derived potential energy surface in GCMC simulation. *J. Phys. Chem. C*. **2011**, 115, 23074-23080.
106. Watanabe, T.; Manz, T.A.; Sholl, D.S. Accurate treatment of electrostatics during molecular adsorption in nanoporous crystals without assigning point charges to framework atoms. *J. Phys. Chem. C*. **2011**, 115, 4824-4836.
107. Zhou, W.; Wu, H.; Hartman, M.R.; Yildirim, T. Hydrogen and methane adsorption in metal-organic frameworks: A high-pressure volumetric study. *J. Phys. Chem. C*. 111, **2009**, 16131-16137.
108. Alcañiz-Monge, J.; Lozano-Castelló, D.; Cazorla-Amorós, D.; Linares-Solano, A. Fundamentals of methane adsorption in microporous carbons. *Micropor. Mesopor. Mater.* **2009**, 124, 110-116.
109. Olah, G.A.; Surya Prakash, G.K.; Goepfert, A. Anthropogenic chemical carbon cycle for a sustainable future. *J. Am. Chem. Soc.* 133, **2011**, 12881-12898.
110. Wu, C.; Cheng, H.-M. Effects of carbon on hydrogen storage performances of hydrides. *J. Mater. Chem.* **2010**, 20, 5390-5400.
111. Fichtner, M. Nanoconfinement effects in energy storage materials. *Phys. Chem. Chem. Phys.* **2011**, 13, 21186-21195.
112. Bhakta, R.K.; Herberg, J.L.; Jacobs, B.; Highley, A.; Behrens, R.Jr.; Ockwig, N.W.; Greathouse, J.A.; Allendorf, M.D. Metal-organic frameworks as templates for nanoscale NaAlH₄. *J. Am. Chem. Soc.* **2009**, 131(37), 13198-13199.
113. Sun, W.; Li, S.; Mao, J.; Guo, Z.; Liu, H.; Dou, S.; Yu, X. Nanoconfinement of lithium borohydride in Cu-MOFs towards low temperature dehydrogenation. *Dalton Trans.* **2011**, 40, 5673-5676.
114. Majzoub, E.H. First-principles calculated phase diagram for nanoclusters in the Na-Al-H System: A single-step decomposition pathway for NaAlH₄. *J. Phys. Chem. C*. **2011**, 115, 2636-2643.

115. Gross, A.F.; Vajo, J.J.; Van Atta, S. L.; Olson, G.L. Enhanced hydrogen storage kinetics of LiBH₄ in nanoporous carbon scaffolds. *J. Phys. Chem. C*. **2008**, 112, 5651-5657.
116. Gosalawit-Utke, R.; Nielsen, T. K.; Saldan, I.; Laipple, D.; Cerenius, Y.; Jensen, T.R.; Klassen, T.; Dornheim, M. Nanoconfined 2LiBH₄-MgH₂ Prepared by direct melt infiltration into nanoporous materials. *J. Phys. Chem. C*. **2011**, 115, 10903-10910.
117. Li, Y.; Zhou, G.; Fang, F.; Zhang, Q.; Ouyang, L.; Zhu, M.; Sun, D. De-/ rehydrogenation features of NaAlH₄ confined exclusively in nanopores. *Acta Materialia*. **2011**, 59, 1829-1838.
118. Gao, J.; Adelhelm, P.; Verkuijlen, M.H.W.; Rongeat, C.; M.; Herrich, van Bentum, P.J.M.; Gutfleisch, O.; Kentgens, A. P.M.; de Jong, K.P.; de Jongh, P.E. Confinement of NaAlH₄ in nanoporous carbon: Impact on H₂ release, reversibility, and thermodynamics. *J. Phys. Chem. C*. **2010**, 114, 4675-4682.
119. Gunaydin, H.; Houk, K.N.; Ozolins, V. Vacancy-mediated dehydrogenation of sodium alanate. *PNAS*. **2008**, 105(10), 3673-3677.
120. Fang, Z.Z.; Wang, P.; Rufford, T.E.; Kang, X.D.; Lu, G.Q.; Cheng, H.M. Kinetic- and thermodynamic-based improvements of lithium borohydride incorporated into activated carbon. *Acta Materialia*. **2008**, 56, 6257-6263.
121. Ngene, P.; Verkuijlen, M.H.W.; Zheng, Q.; Kragten, J.; van Bentum, J.M.; Bittera, J.H.; de Jongh, P.E. The role of Ni in increasing the reversibility of the hydrogen release from nanoconfined LiBH₄. *Faraday Discussion*. **2011**, 151, 47-58.
122. Balde, C.P.; Hereijgers, B.P.C.; Bitter, J.H.; de Jong, K.P. Facilitated hydrogen storage in NaAlH₄ supported on carbon nanofibers. *Angew. Chem. Int. Ed.* **2006**, 45, 3501-3503.
123. Balde, C.P.; Hereijgers, B.P.C.; Bitter, J.H.; de Jong, K.P. Sodium alanate nanoparticles-linking size to hydrogen storage properties. *J. Am. Chem. Soc.* **2008**, 130, 6765-6761.
124. Stavila, V.; Bhakta, R.K.; Alam, T.M.; Majzoub, E.H.; Allendorf, M.D. Reversible hydrogen storage by NaAlH₄ confined within a titanium functionalized MOF-74(Mg) nanoreactor. *ACS NANO*. **2012**, 6 (11), 9807-9817.

8

APPENDIX

8.1 PRESENTATIONS OF THIS DISSERTATION (ORAL AND POSTER)

Orefuwa, S.A., Yang, H., Iriowen, E., Alexander, D., Wakefield, B., and Goudy, A. “Enhancing Hydrogen Storage Capacity in Isoreticular Metal-Organic Framework (IRMOF-8): Synthesis and Functionalization” World Hydrogen Energy Conference, Toronto, Canada. **June 3-7, 2012.** (Poster presentation)

Orefuwa, S. A., Yang, H., and Goudy, A. J. “Improving the Desorption Temperature of NaAlH_4 for Hydrogen Storage Application” Graduate Research Symposium, Dover, DE. **April 20, 2012.** (Oral presentation)

Yang, H., **Orefuwa, S.**, and Goudy, A. “Solvent Assisted Mechanochemical Synthesis in the Formation of the Metal–Organic Framework $\text{Cu}_3(\text{BTC})_2$ for Hydrogen Storage” MRS Fall meeting, San Francisco, CA. **April 9-April 13, 2012.** (Poster presentation)

Wakefield, B., Goudy, A, **Orefuwa, S.**, Lott, L. Q., Alexander, D., and Kerr, A. “Synthesis of New Naphthalene Linkers for the Incorporation in Hydrogen Storing Metal-Organic Frameworks” ACS Meeting, Washington, DC **August, 2011.** (Poster presentation)

Orefuwa, S.A., Yang, H., Alexander, D., Wakefield, B., and Goudy, A.J. Characterization and Hydrogen Enthalpy of a Novel IRMOF-8-NO₂ prepared by a Rapid Solvothermal method” Gordon Research Conference, Easton, MA. **July, 2011.** (Poster presentation)

Yang, H., **Orefuwa, S.A.**, and Goudy, A. “Study of mechanochemical synthesis in the formation of the metal–organic framework $\text{Cu}_3(\text{BTC})_2$ for hydrogen storage: An efficient and environmentally benign approach” 15th Annual Green Chemistry and Engineering Conference + 5th International Conference on Green and Sustainable Chemistry. Washington, DC. **June, 2011.** (Poster presentation)

National Organization for the Professional advancement of Black Chemists and Chemical Engineers (NOBCChe). Maryland, USA. **September 2009.** (Attendee)

8.2 LIST OF PUBLICATIONS OF THIS DISSERTATION

Orefuwa, S.A., Iriowen E., Yang, H., Wakefield, B.H., Goudy, A.J. Effects of nitro-functionalization of the gas adsorption properties of isoreticular metal-organic framework-eight (IRMOF-8). Under review, microporous and mesoporous materials 2013.

Orefuwa, S.A., Yang, H., Goudy, A.J. Rapid solvothermal synthesis of an isoreticular metal-organic framework with permanent porosity for hydrogen storage. *Micropor. Mesopor. Mater.* **2012**, 153, 88–93.

Yang, H., **Orefuwa S. A.**, Goudy, A. Study of mechanochemical synthesis in the formation of the metal-organic framework $\text{Cu}_3(\text{BTC})_2$ for hydrogen storage. *Micropor. Mesopor. Mater.* **2011**, 143, 37–45.

OREFUWA SAMUEL ABIDEMI

sammybid@yahoo.com

Permanent Address:
393 Northhampton Way
Middletown, DE 19709
(302) 765-7176

School Address:
Department of Chemistry
Center for Hydrogen Storage
1200 N. DuPont Highway
Dover, DE 19901

EDUCATION

- Delaware State University, Dover, USA** Jan.09-May 13
PhD, (Applied Chemistry)
Dissertation: A Study of an Isoreticular Metal-Organic Framework (IRMOF-8) For Gas Storage: Synthesis, Functionalization and Nanoconfinement
- Delaware State University, Dover, USA** Jan.07-Dec. 08
Master of Science (M.Sc. Applied chemistry),
- University of Agriculture Abeokuta, Nigeria** Mar.98-Feb.02
Bachelor of Science (BSc Biochemistry),
- Federal Polytechnic Ilaro, Ogun State** Jan.95-Dec. 96
National Diploma in Science Laboratory Technology (SLT),

ACCOMPLISHMENTS**Honors/Awards:**

- Best in Session at the Graduate Research symposium, Dover, DE Apr.12
- Graduated on Dean's list, University of Agriculture Feb. 02

Grants:

- Thurgood Marshall College fund for Graduate Students Sept.09-Sept.10

Affiliation:

American Chemical Society

RESEARCH EXPERIENCE

- Delaware State University, Center for Hydrogen Storage and Research** Jan.07-
Present
- Research Assistant; Assist professor with research in metal hydride and metal-organic frameworks (functionalization, synthesis and characterization) in the laboratory

- Developed a new rapid and inexpensive method for synthesizing metal-organic frameworks
Development of a new functionalized material with high enthalpy for gas storage
- Developed a method for interfacing the results between two instruments; pressure in residual gas analyzer (RGA) to temperature profile of pressure composition isotherm (PCI) instrument
- Trained other first year graduate students on instrumentation
- Preparation of standard operational procedure for instruments used

TECHNIQUAL SKILLS

Proficient in the use of;

- Microscope
- UV-Spectroscopy, FTIR (Fourier transform infrared spectroscopy)
- Thermogravimetric analyzer (TGA)
- Pressure composition isotherm (PCI)
- X-ray Diffractometer
- Residual gas analyzer (RGA) and GC-MS
- Laser diffraction particle size analyzer
- High pressure volumetric analyzer (HPVA)
- Surface area and porosity analyzer
- Nuclear Magnetic Resonance (NMR)
- Effective communication and interpersonal skills
- Proficient in data analysis using Microsoft office

TEACHING EXPERIENCE

Delaware State University, Center for Hydrogen Storage and Research

Jan.07-Present

- Teaching Assistance (Gen Chem. 102 lab, a class of 20 students)

Chi-Ben Comprehensive College, Lagos

Sept.03-Nov.06

- Subject Tutor in Chemistry and Biology
- Preparing and coordinating students for national examinations
- Head of Department (Sciences): Oversaw the work of five staff members in my department

Sokoto Teachers' College, Sokoto

Sept.02-Aug.03

- Subject Tutor in Chemistry

RELATED PROFESSIONAL EXPERIENCE

Eucharistic Heart of Jesus Clinic, Lagos

Jan.05-Apr.05

- Laboratory scientist: investigated biological specimens; Blood, Sputum, Urine, Seminal fluid

El-Rapha Medical Diagnostic Center, Lagos

Dec.96-Aug.97

- Laboratory technician (Practical training): investigated Biological specimens for medical diagnosis

PUBLICATIONS

Orefuwa, S.A., Iriowen, E.M., Yang, H, Wakefield, B.H., Goudy, A.J. Effects of nitro-functionalization on the gas adsorption properties of isoreticular metal-organic framework-eight (IRMOF-8) (under review) microporous and mesoporous materials.

Overton, A.T., **Orefuwa, S.A.**, Mohamed, A.A. Fluorous gold organometallic Electrode. (under review) Organometallics

Orefuwa, S. A., Yang, H., Goudy, A. J. Rapid solvothermal synthesis of an isoreticular metal-organic framework with permanent porosity for hydrogen storage. *Micropor. Mesopor. Mater.* **2012**, 153, 88–93

Yang, H., **Orefuwa S. A.**, Goudy, A. Study of mechanochemical synthesis in the formation of the metal-organic framework $\text{Cu}_3(\text{BTC})_2$ for hydrogen storage. *Micropor. Mesopor. Mater.* **2011**, 143, 37–45

Oyedapo, O.O., Akinpelu, B.A., **Orefuwa, S.A.** Anti-inflammatory effect of *Theobroma cacao* root extract. *J. Trop. Med. Plants.* **2004**, 5, 161-166

CONFERENCES

Orefuwa, S.A., Yang, H., Iriowen, E., Alexander, D., Wakefield, B., and Goudy, A. “Enhancing Hydrogen Storage Capacity in Isoreticular Metal-Organic Framework (IRMOF-8): Synthesis and Functionalization” World Hydrogen Energy Conference, Toronto, Canada. **June 3-7, 2012.** (Poster presentation)

Orefuwa, S. A., Yang, H., and Goudy, A. J. “Improving the Desorption Temperature of NaAlH_4 for Hydrogen Storage Application” Graduate Research Symposium, Dover, DE. **April 20, 2012.** (Oral presentation)

Yang, H., **Orefuwa, S.**, and Goudy, A. “Solvent Assisted Mechanochemical Synthesis in the Formation of the Metal-Organic Framework $\text{Cu}_3(\text{BTC})_2$ for Hydrogen Storage” MRS Fall meeting, San Francisco, CA. **April 9-April 13, 2012.** (Poster presentation)

Wakefield, B., Goudy, A, **Orefuwa, S.**, Lott, L. Q., Alexander, D., and Kerr, A. "Synthesis of New Naphthalene Linkers for the Incorporation in Hydrogen Storing Metal-Organic Frameworks" ACS Meeting, Washington, DC **August, 2011.** (Poster presentation)

Orefuwa, S.A. Yang, H., Alexander, D., Wakefield, B., and Goudy, A.J. Characterization and Hydrogen Enthalpy of a Novel IRMOF-8-NO₂ prepared by a Rapid Solvothermal method" Gordon Research Conference, Easton, MA. **July, 2011.** (Poster presentation)

Yang, H., **Orefuwa, S.A.**, and Goudy, A. "Study of mechanochemical synthesis in the formation of the metal-organic framework Cu₃(BTC)₂ for hydrogen storage: An efficient and environmentally benign approach" 15th Annual Green Chemistry and Engineering Conference + 5th International Conference on Green and Sustainable Chemistry. Washington, DC. **June, 2011.** (Poster presentation)

National Organization for the Professional advancement of Black Chemists and Chemical Engineers (NOBCChe). Maryland, USA. **September 2009.** (Attendee)

REFERENCES

Andrew J. Goudy, Ph.D.
Dir, Hydrogen Storage Research Center
Department of Chemistry
SCS 326
302-857-6534
agoudy@desu.edu

Bizenuh Workie, Ph.D.
Department of Chemistry
SCS 322
302-857-6545
bworkie@desu.edu

Ahmed Mohamed, Ph.D
Department of Chemistry
Assistant Professor
SCS 324
302-857-6531
amohamed@desu.edu